Summer 2011

Characterizing cartilage-specific T1rho MRI for clinical translation and application

Noelle F. Klocke
University of Iowa

Recommended Citation

Klocke, Noelle F.. "Characterizing cartilage-specific T1rho MRI for clinical translation and application." MS (Master of Science) thesis, University of Iowa, 2011.
http://ir.uiowa.edu/etd/1155.

CHARACTERIZING CARTILAGE-SPECIFIC T1RHO MRI FOR CLINICAL TRANSLATION AND APPLICATION

by

Noelle F. Klocke

A thesis submitted in partial fulfillment
of the requirements for the Master of
Science degree in Biomedical Engineering
in the Graduate College of
The University of Iowa

July 2011

Thesis Supervisors: Professor Thomas D. Brown
Research Associate Professor Douglas R. Pedersen

Graduate College
The University of Iowa
Iowa City, Iowa

CERTIFICATE OF APPROVAL

MASTER'S THESIS

This is to certify that the Master's thesis of

Noelle F. Klocke

has been approved by the Examining Committee
for the thesis requirement for the Master of Science
degree in Biomedical Engineering at the July 2011 graduation.

Thesis Committee: ___________________________________
Thomas D. Brown, Thesis Supervisor

____
Douglas R. Pedersen, Thesis Supervisor

____
Joseph M. Reinhardt

____
Daniel R. Thedens

ACKNOWLEDGMENTS

I would first and foremost like to thank and acknowledge my thesis supervisors, Drs. Doug Pedersen and Thomas Brown, for their invaluable guidance over the past couple of years. Secondly, I would like to acknowledge and thank the other members of my thesis committee, Drs. Dan Thedens and Joseph Reinhardt, for their guidance and perspectives. I would also like to thank the other members of the research team. For the construction and assembly of the phantom used in this work, I would like to thank and acknowledge Tom Baer and Dr. James Martin. Patient recruitment and clinical perspectives were given by Dr. Annunziato (Ned) Amendola, Dr. Glenn Williams, and Catherine Fruehling-Wall. The financial support for this research was provided by NIH NIAMS Program Grant P50 AR055533. Outside of the research team, I would like to thank the other faculty and graduate students in the Orthopaedic Biomechanics Research Laboratory for the countless discussions that spurred this work forward. It was truly a unique research opportunity that will surely guide my future professional decisions. Lastly, I would like to thank my friends and family for their love and support during this academic journey.

TABLE OF CONTENTS

LIST OF TABLES

Table

LIST OF FIGURES

Figure

CHAPTER 1: AN INTRODUCTION TO THE BURDEN OF OSTEOARTRHRITIS

As estimated in 2005, approximately one-third of adults (≥18 years) in the United States suffer from arthritis or chronic joint symptoms, costing the nation approximately $114.5 billion per year [1]. This translates to an economic burden of approximately 1% of the official GDP [2]. Obviously, understanding the pathogenesis and early detection of the disease is important for the overall health and fiscal well-being of the nation.

Osteoarthritis is a degenerative disease of articular cartilage, whose early stages include loss of proteoglycan and other macromolecules in the extracellular matrix, which eventually leads to cartilage thinning, patient pain and possible loss of mobility [3]. While primary osteoarthritis (OA) is variable in its onset and progression, post-traumatic osteoarthritis (PTOA) is easier to study because it develops after a distinct traumatic event, such as a meniscal tear or an intra-articular fracture. PTOA accounts for approximately 9.8% of knee OA patients; the lower-extremity joint most commonly afflicted by OA [1]. Anterior cruciate ligament (ACL) rupture is one traumatic event that has been shown to be a precursor to PTOA (which develops in 60-90% of patients at 10-15 years post-ACL injury), with rupture commonly occurring in young athletes, such as female soccer players [4, 5]. Young (≤ 35 years) ACL-rupture patients were chosen as the model to investigate PTOA progression in the knee within this work.

Magnetic resonance imaging (MRI) is a non-ionizing imaging modality that has been used for soft-tissue investigations in the medical field since the 1970s [6]. This modality is ideal for studying musculoskeletal anatomy and many different disorders, since it provides the opportunity for different contrasts and clinical diagnostic capabilities to be achieved between tissues [7]. Structural abnormalities and changes may be viewed in morphologic imaging sequences, such as fast low-angle shot (FLASH) and 3D spoiled-gradient-recalled echo (SPGR), whereas other sequences provide insight into the biochemistry of a tissue, such as quantitative sequences like T2-mapping and T1rho. These quantitative sequences are obtained by acquiring the same slice image multiple times, and by varying the key parameter associated with image contrast (i.e. spin-lock time in T1rho), an exponential decay curve may be determined. The relaxation time found from these exponential-decay curves may be thought of as a tissue's characteristic material property within the realm of MR. This relaxation time constant may be considered analogous to a characteristic material property within the physical world (i.e. a metal's Young's modulus determined by a uniaxial tensile test). These relaxation times give a quantitative measure of the molecular interactions occurring within the imaged tissues.

T1rho MRI, the spin-lattice relaxation in the rotating frame, has been shown to be sensitive to proteoglycan loss in cartilage *in vitro* [8]. It has also been demonstrated to have a higher dynamic range of relaxation times in various OA grade specimens than that found using T2 mapping, another sequence under investigation for monitoring OA development [3]. This wider range may make T1rho more helpful in distinguishing various stages of OA in a clinical setting, since a larger range will allow for more categorizations of PTOA development stages. Knowing which stage a patient is in allows for a more specific treatment plan. Thus, it has been proposed within the research community that T1rho may serve as a biomarker for early cartilage changes associated with PTOA.

However, while research is a necessary tool for investigation of new processes and technologies, if the end product is undeliverable to the general public, its impact will be much less significant than if it is implementable nationwide. This is the primary motivation for this work: Can T1rho MRI be used in an at-risk population and translated to a clinical setting? To determine the feasibility of a clinical T1rho, first the method of how to acquire and interpret the T1rho data will be addressed in a 3.0T MR scanner, the field strength most commonly used and validated in previous T1rho research. Tools (MRI_Relaxation_Map_Tool, Line Profile Analysis) used for measuring T1rho relaxation times will be used and validated in a clinically-relevant patient model, and will address:

1) Is there a quantifiable difference between healthy and injured cartilage in patients?

2) Is there some measure which can be tracked over time and used as a meaningful pre-screening procedure for PTOA development at 3.0T?

Since only 5% of MR scanners have a field strength of 3.0T or more, it is necessary to demonstrate T1rho's data quality on the more clinically-available field strength of 1.5T [6]. In short, a series of preliminary experiments at both 1.5T and 3.0T will address:

3) Is it possible to obtain the same or similar quality data from 1.5T T1rho as found from 3.0T T1rho images?

Within this work, if it is determined that the proposed data analysis tools will provide a means to obtain quantifiable differences at 3.0T, and if image data quality is similar at 1.5T, then such tools could be used in a clinical 1.5T setting to characterize and provide direct patient benefit and insight after a traumatic event. Otherwise, until imaging techniques can be improved, T1rho may be limited to a research environment.

CHAPTER 2: BACKGROUND AND LITERATURE REVIEW

2.1 Pertinent Anatomy and Biomechanics of the Knee

In this work, T1rho imaging's clinical utility is studied within the knee. Basic anatomy and tissue function will provide background to understand the biomechanical failure seen during ACL-rupture. Since this joint is often used for studying post-traumatic osteoarthritis progression, a basic description of the current paradigms for how PTOA occurs will provide the motivation for why this is an ideal patient population and how T1rho imaging can be interpreted in a biomechanically meaningful way as a diagnostic tool.

2.1.1 Anatomy

The knee is comprised of four bones; the femur, patella, tibia, and fibula. Ligaments are primarily responsible for the stabilization of this joint, unlike other joints, such as the hip, which rely primarily on boney congruency. Because of this, the knee is one of the most unstable and most injury-prone articulating joints in the body [9].

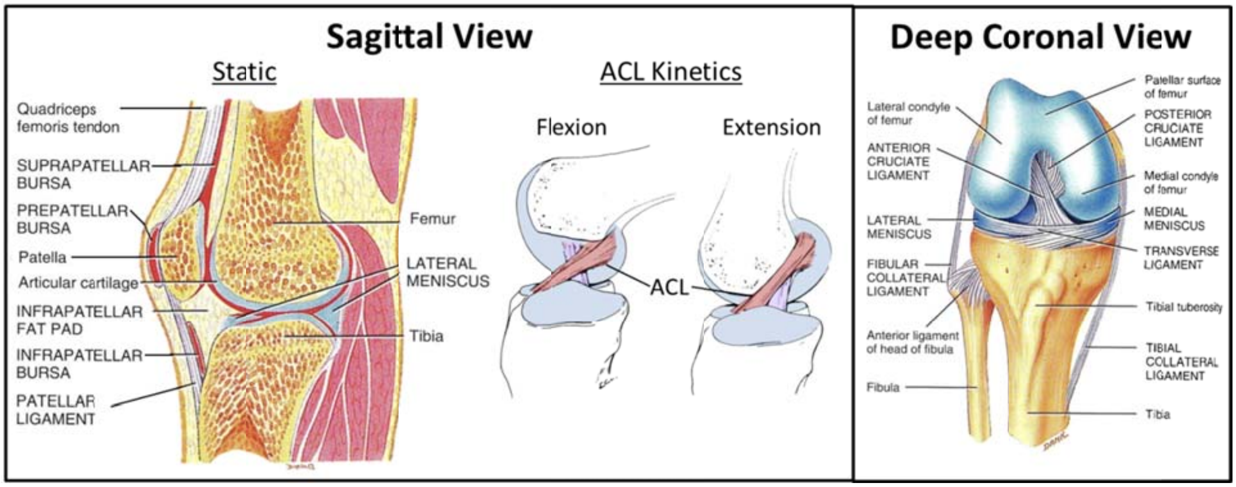

Figure 1. Basic anatomy of the knee. Images reproduced and reformatted from Blackburn and Craig (ACL Kinetics, [10]) and from Tortora (static sagittal view, deep coronal view, [11]).

The cruciate ligaments are found within the intercondylar notch of the femur. The posterior cruciate ligament (PCL) provides resistance to posterior motion of the tibia relative to the femur, whereas the anterior cruciate ligament resists anterior subluxation [9]. The other two main ligaments, the medial collateral ligament and the lateral collateral ligament, provide for varus/valgus and rotational stabilization of the knee. The meniscus also performs some stabilization of the knee, as it wraps around on the tibial plateau to cradle the femoral condyles into place. This is especially important in the lateral compartment, since the lateral femoral condyle and the lateral tibial plateau are both slightly convex in geometry [10]. Friction between the bones is significantly reduced at their interfaces by the smooth articular cartilage (more detail in section 2.2 Cartilage) and the synovial fluid.

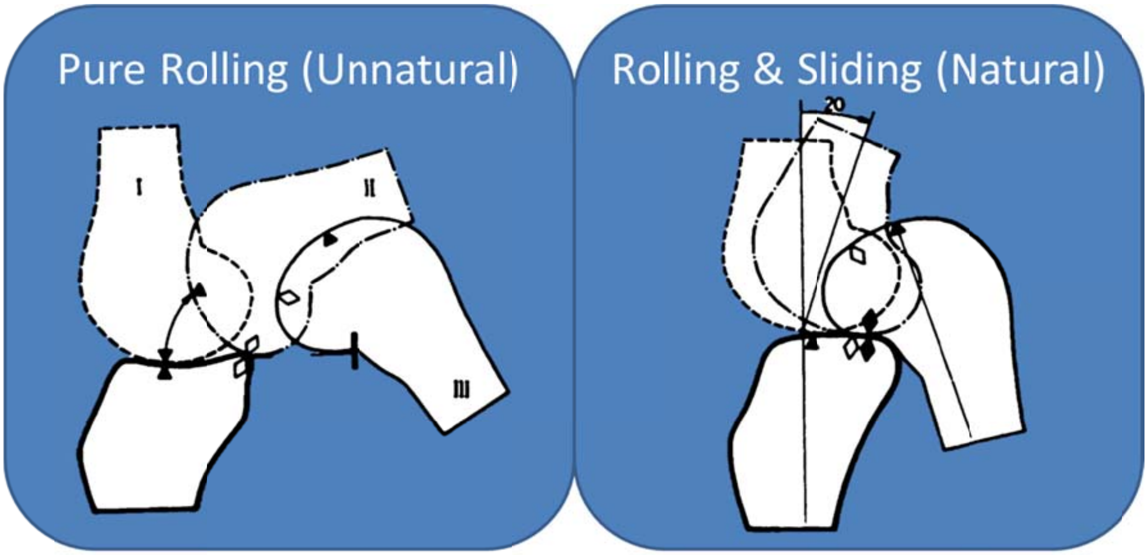

Figure 2. If only rolling were allowed during knee flexion, the femur would unnaturally roll off of the posterior tibial plateau (left). With the cruciate ligaments, simultaneous rolling and sliding is allowed such that the femur remains in contact with the tibial plateau; typically described as the four-bar cruciate linkage system (right). Images adapted from Fu et al. [12].

As flexion occurs, the femoral condyles roll and slide posteriorly along the tibial plateau; this flexion-extension mechanism is typically characterized as the four-bar cruciate-linkage system between the cruciate ligaments and the two bones [12]. The joint relies on the cruciate ligaments for such anterior-posterior restraint, but other forces from the gastrocnemius-soleus complex and quadriceps groups are also responsible for reducing the entire loads and impulses experienced by the knee joint [5, 12]. The medial compartment has been found to be subjected to higher forces than the lateral during stance [13]. Therefore, the complexity of each role a particular tissue plays in joint kinematics is further muddled during acute ACL rupture.

2.1.2 ACL Injury and the Consequences

The anterior cruciate ligament (ACL) is primarily composed of type-I collagen which is grouped into bundles with a crimped pattern, and on average is approximately 31-38mm long and 11mm wide [12]. While it is generally accepted that the posterior cruciate ligament tensile strength is greater than the ACL's, one cadaveric study found that a pure quadriceps force of 4500 N was necessary to produce tearing of the ACL [12, 14]. This excessive force is not usually seen in the quadriceps, so it is only logical that some other mechanism must be involved during the 80,000-200,000 ACL ruptures seen in the United States each year [15, 16].

Noncontact ACL injuries (i.e. pivoting or jump-landing) encompass approximately 70% of all ACL injuries, compared to only 30% from direct contact with another player or object [15]. Several studies have identified risk factors for noncontact ACL-rupture to be environmental (knee braces, high friction between shoes-surface), anatomical (typical male joint geometry compared to female, shallow medial tibial plateaus), and biomechanical (muscle fatigue, full body kinematics) [5, 15]. More specifically, studies have tried to answer why females have a two-to-eight fold higher risk and prevalence of ACL rupture compared to their male counterparts involved in similar activities (i.e. soccer) [16]. Some propose that a smaller intercondylar notch, steeper tibial slope (causing higher anterior shear components), predisposition to anterior/posterior laxity, lower muscle stiffness, more valgus alignment, greater hip varus, foot pronation, and even hormonal fluctuations during the menstrual cycle to be responsible for the higher prevalence of ACL rupture in women [5, 15, 17].

Many kinematic mechanisms for noncontact injury have been proposed. However, after an extensive review of the literature, Quatman et al. found that the vast majority of studies tend to agree that multi-planar forces, rather than single plane forces, are responsible for ACL rupture [16]. It is also known that partial flexion of the knee is a common position at time of injury, and that perhaps whole body dynamics are responsible for injury [5]. Other proposed mechanisms include a near-flat foot contact with the ground during deceleration and hip extension combined with knee flexion [5, 17]. However, it has been shown that with carefully designed exercises, athletes may be able to reduce ACL injury rate by learning ACL-protective maneuvers [15].

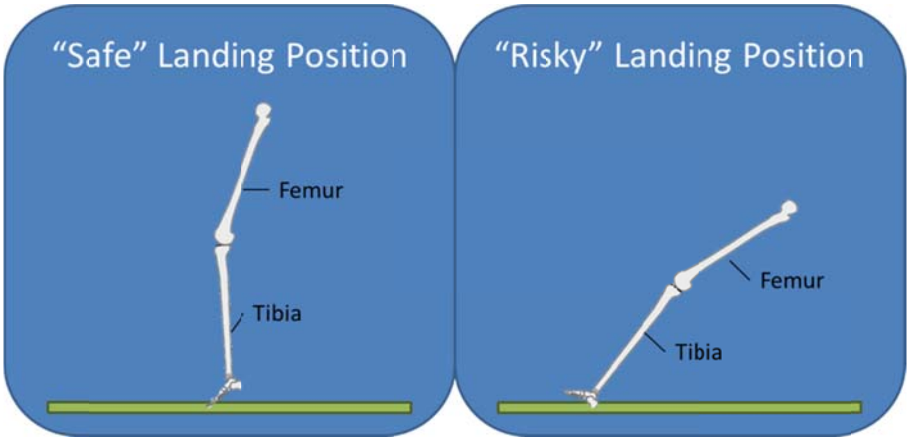

Figure 3. An ACL-protective landing is shown on the left, whereas one proposition for an injurious landing position (note the slight knee flexion and foot parallel to the ground) is shown on the right. Adapted from Boden et al. [5].

Another motivating factor for studying ACL-rupture, and how best to treat and prevent it, is the effect such a traumatic injury has on the rest of the tibiofemoral joint. More specifically, it has been found that 60-90% of ACL-rupture patients exhibit radiologic changes consistent with osteoarthritic development 10-15 years after injury, regardless of whether the ACL is reconstructed [4, 17, 18]. In order to understand this progression, normal cartilage structure and function, and then the changes associated with this disease will be discussed in the next section.

2.2 Cartilage

2.2.1 Structure and Biochemical Composition

Articular cartilage is an avascular connective tissue found in synovial joints. The main function of cartilage is to act as a "shock absorber" and cushion by distributing joint loading over a large area, but it also reduces friction during normal kinematics. Cartilage is inherently designed to handle compressive loads, and is therefore not known to withstand shear stresses as well, which may be seen during ACL-rupture kinematics [18]. The structure of the extracellular matrix (ECM), which is maintained by chondrocyte cells, provides the basis for this tissue's mechanical properties (Figure 4).

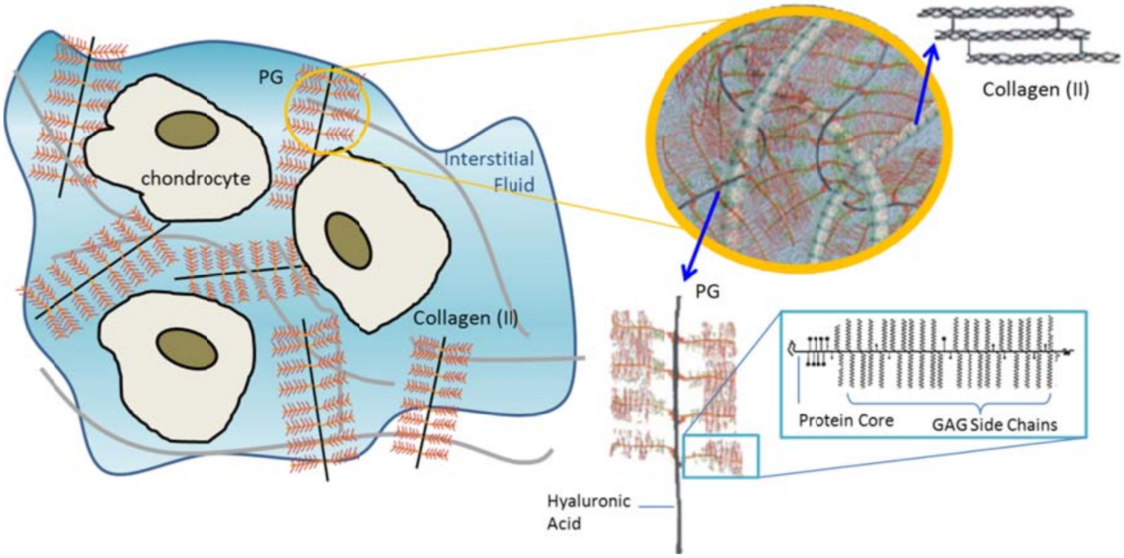

Figure 4. A representation of the extracellular matrix (ECM) and its constituents surrounding chondrocytes within cartilage. Images adapted and reproduced from Borthakur et al. [19].

The macromolecular ECM network restricts interstitial fluid flow (about 75% weight of cartilage) during normal joint loading, such that the pressurized fluid distributes and supports the mechanical load [20]. The two largest macromolecular constituents within the network are collagen (70-80% of the dry weight) and aggrecan, which contains negatively-charged glycosaminoglycan (GAG) molecules; these macromolecules are responsible for the tensile and shear strength and the compressive strength of the cartilage, respectively [20, 21]. All GAG macromolecules have carboxylate and sulfate groups in their side chains, and this negative charge is the reason for GAG macromolecules' attraction to Na^+ ions [22, 23]. Electroneutrality in normal cartilage is maintained by a balance between the negative fixed charge of the cartilage's macromolecules and charge of the ions within the interstitial fluid; this is important since mobile ion concentration is significantly different between normal and degenerated (GAG-depleted) cartilage [21]. GAG is composed of three main subunits, chondroitin 4-sulfate, chondroitin 6-sulfate, and keratin sulfate, with the chondroitin sulfates accounting for 55-90% of the total GAG side chains [24].

Collagen structure, chondrocyte population, and proteoglycan content of the extra-cellular matrix vary depending upon the zone (Figure 5). In the superficial zone collagen fibers run approximately parallel to the surface, in the radial and deep zones they are directed approximately perpendicular to the surface, and are randomly oriented in the transitional zone. Within the histology images in Figure 5, PG is identifiable using Safranin-O stain, with more stain meaning increased PG content. It has been found that PG content is highest in the middle zone (radial) compared to the other zonal layers [25]. The way these zones would be imaged with the T1rho MRI sequence used in this work is shown in the bottom panel (Figure 5). Since zonal layers' ECM constituents vary, this sampling in MR should provide some information about the individual layers' properties. However, since this zonal continuum is discretized when imaged, there are partial volume effects present in the bone-cartilage interface (bone and cartilage signals, black box) and the superficial (cartilage and fluid, blue box) zones. Therefore, these zones are ignored during image post-processing (average 2mm thick for femoral articular cartilage, [26]).

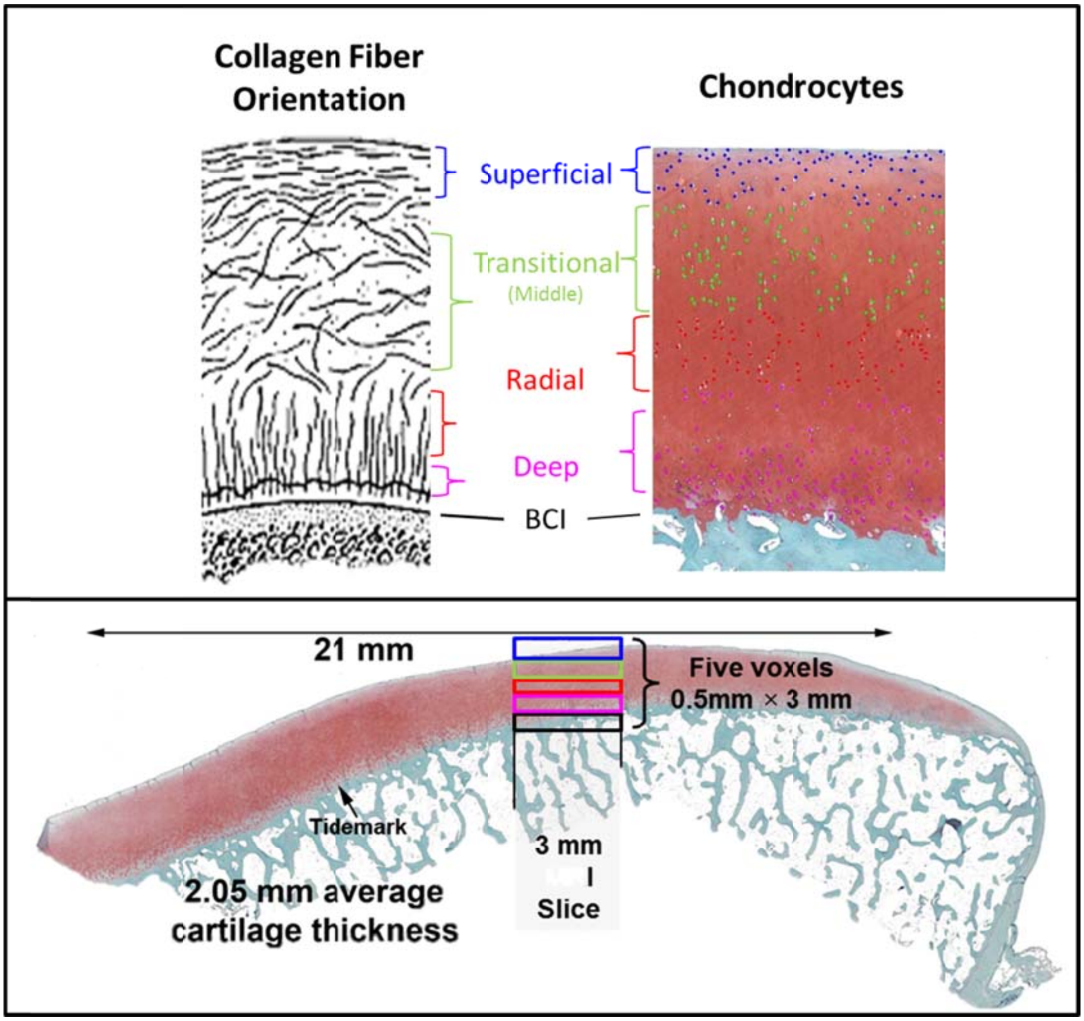

Figure 5. Collagen fiber orientation throughout the zonal layers as adapted from Borthakur et al. [19] alongside chondrocyte population throughout the zones. The histology image below shows how these physical zones are related to the sampled MRI voxels used in the rest of this work. While cartilage is a continuum, MRI sampling discretizes the tissue, and this is why partial volume effects would affect the bone-cartilage interface and superficial zones' MR samplings.

While these zonal PG and collagen variations exist, changes to these biological structures are possible. Architectural remodeling is presumed to occur due to altered mechanical loading of cartilage, with the tissue being best "designed" to withstand daily forces [20]. Even with short-term changes of physical activities, it has been documented that cartilage thickness can significantly be altered [27]. Some negative mechanical changes can also be incurred. Pro-inflammatory cytokines and proteases produced by chondrocytes may cause cleavage and denaturation of collagen, fragmentation and loss of PG, and general tissue weakening [13]. Some of these changes are naturally seen as people age.

Aging affects cartilage state. The content of GAG decreases with increasing age, thereby affecting other structural and functional changes [28]. In a study of healthy subjects, cartilage volume and thickness was lost at a rate of 4% per decade after the age of fifty [27]. Cartilage tensile properties decrease as aging occurs, and may reflect chondrocyte death, mechanical surface wear, and degradation of the extracellular matrix components [13]. In a study by Temple et al., a decrease in the Middle age group's (40-59years) superficial layer's tensile strength, and increased surface wear, were noted versus asymptomatic OA cartilage specimens of the Young group (20-39years). Further degradation occurred between the Middle and Old (≥60years) groups studied, with decreased cellularity and GAG content of the deep layer, especially in the weight-bearing regions and medial compartments [13]. In general, OA tends to progress at a faster rate for older individuals, does not tend to regress on its own, and has a "snow-ball effect", in which the disease progresses more rapidly in more advanced stages [29].These asymptomatic age-related changes may be detectable in MRI images, such as the increase in T2 relaxation times in the transitional zone of cartilage [22]. Such changes occurring during aging or after a traumatic event constitute the onset of osteoarthritis.

2.2.2. Osteoarthritis

Complete understanding of osteoarthritis (OA) development and progression remains elusive. While certain patterns have been identified, the *exact* series of events leading to cartilage degeneration is not well understood. OA is typically characterized as a degenerative disease of the articular cartilage leading to loss of form and function. There are two types of OA.

Risk factors for primary OA include genetic predisposition, hormonal influences, inflammation, leg-length inequality, and changes in biomechanics [20, 30]. One form of secondary OA is characterized as osteoarthritic progress after a known stimulus, such as ACL-rupture, which has been shown to make an affected individual 7.4 times more likely to develop OA as compared to a non-injured individual [31]. Depending upon the severity of the injury, post-traumatic osteoarthritis (PTOA) may develop in as little as two years [32]. Besides a relatively fast onset, OA progression seems to accelerate with ACL rupture insult, since there is an increased risk of advancing OA by more than one point on the Kellgren-Lawrence (K-L) scale over 10 years post-injury [18]. This K-L score is a common way to characterize knee pain and OA, and ranges from 0 (none or normal) to 4 (severe), with a score of 2 or higher being characteristic of OA [33, 34].

Changes within the extracellular matrix (ECM) are precursors to disease development. Reduction of tissue GAG content (especially in the superficial layer) is proposed to be one of the earliest changes, followed by irreversible changes of collagen network fragmentation and re-orientation, which reduces the normal water-restraining function of the cartilage and allows the tissue to swell [3, 28]. This theory is supported by animal models, where hypertrophy preceded cartilage breakdown [31]. Next, an overall increase in water content and loss of the cartilage pressure ultimately leads to chondrocyte death and tissue loss [20]. So while radiography and morphometric MRI sequences may be able to detect end-stage degenerative changes, early biochemical changes in OA are not apparent [35].

One study found ACL-rupture patients had an increased risk for OA pathological features [18, 30]. Focal cartilage abnormalities of the far posterior articular cartilage were seen 2.5 times more frequently in the lateral femoral condyle compared to the medial femoral condyle [36]. One of these pathological features has been studied thoroughly due to its prevalence. Bone marrow lesions (a.k.a. bone bruises, occult osteochondral lesions) are discovered in 80% of ACL rupture patients [37]. The theorized contributors to these abnormal MR signals are blood, edema, hyperemia and subchondral bone microfracture [37]. A common location for a bone marrow lesion is deep to the lateral femoral condyle's sulcus, which is a shallow bone dimple at approximately the sagittal midline of the condyle and is the junction between the tibiofemoral and patellofemoral articular surfaces [37]. Significantly larger volumes for bone marrow lesions are related to cortical depression fractions, and have been demonstrated to be a sign of a strong compressive force near the articular surface [31]. These bone marrow lesions have led to a theory that during ACL rupture, the anterolateral femur impacts the posterolateral tibia [38]. Some evidence for this theory include a study of nine patients which found bone marrow lesions were most common in the lateral tibia and the lateral femoral condyle [38], These lesions have been observed to gradually decrease or disappear over a time course of nominally a year [31, 38].

Some sequelae to ACL-injury include osteosclerosis and osteochondral defects [37]. Other OA-related maladies include synovitis, which was exhibited in 89.2% of OA-affected knees within one study, and had a strong correlation to knee pain severity as assessed by the Western Ontario and McMaster Osteoarthritis Index (WOMAC) pain scale [30].

Treatment options for OA are being developed and studied within clinical trials, such as cartilage resurfacing procedures and pharmaceuticals, but each have had varied success [39]. As of yet, there are no disease-modifying OA drugs which are approved by the Food and Drug Administration [30]. However, some drugs (i.e. celecoxib) are currently under investigation for their use in abating cartilage loss [30]. Others have found that involvement in rigorous physical activity at baseline resulted in a reduced annual rate of patellar cartilage loss [30].

2.3 Magnetic Resonance Imaging as a Diagnostic Tool

Osteoarthritis diagnosis has historically used radiographic changes (i.e. joint space narrowing) as the “gold standard” for identification [27]. An advantage of this imaging modality is that it is less expensive than other imaging modalities (approximately one-fifth the cost of a basic MRI knee scan, [40]). However this technique is highly unreliable (false-positive rates as high as 20-40%), is non-specific to global cartilage loss, is insensitive to biochemical changes, and does not generally correlate with pathologic joint destruction severity [32, 41, 42]. Thus, there has been a large interest in magnetic resonance imaging to accurately assess injuries.

Magnetic resonance imaging (MRI) has been shown to be a noninvasive imaging technique that is ideal for soft-tissue characterization. Reports show that more abnormalities are detectable within soft tissues, like cartilage, in MR images than compared to the late-stage OA findings in radiographs, thereby showcasing MRI's potent diagnostic capabilities and potential use in OA-abating drug trials [18, 43]. While there has been a little work within computed tomography (CT) or ultrasound for cartilage analysis, MRI has been the predominant imaging modality under investigation [41]. As such, several different sequences have been used to study PTOA in multi-center cohorts, such as the osteoarthritis initiative (OAI, [44]). The OAI encompasses approximately 5,000 patients and five 3.0T scanners [44]. To facilitate multiple research centers pursuing the same knowledge, Eckstein et al. proposed nomenclature for discussing anatomic abnormalities, in hopes of expediting discussion across research groups [45]. These labels, such as cAB for the bone-cartilage interface, are commonly utilized in this and others' bodies of work.

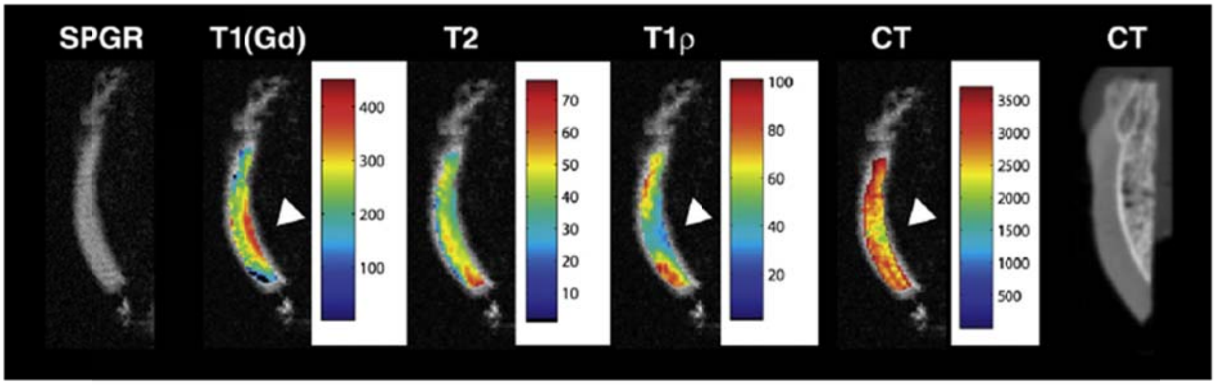

Figure 6. To introduce what some cartilage-specific modalities look like, sample images from Taylor et al. show typical morphometric MRI (SPGR), quantitative MRI (T1(Gd) (dGEMRIC), T2, T1rho), and contrast-enhanced CT of osteochondral datasets [41].

Two main subsets of sequences are under investigation. Biochemical/quantitative imaging is good for early PTOA assessment and perhaps guiding prevention, whereas morphologic imaging is better for knowing end-stage OA geometries and how best to surgically intervene [46]. After introduction to MR imaging principles, sequences of each type will be discussed.

2.3.1. The Basic Physics of MR Imaging

Magnetic resonance imaging relies upon the principle of nuclear magnetic resonance. Each nucleus within an atom has a positive charge, but nuclei with odd atomic number or odd mass number (H^1, Na^{13}) have angular momentum, which causes the protons to "spin" and produce individual miniscule magnetic fields. The rate a magnetic dipole spins depends upon the proton being imaged and the strength of the magnetic field, and is known as the gyromagnetic ratio (γ, γ^{H1}=42.58*2π rads/Tesla, [7]). Each proton (since H^1 is most common, this shall be the reference for this discussion) spins independently of its neighbors at any given instant; therefore the net sum of all magnetization vectors (which are produced by this spinning) is zero. However, when under a strong magnetic field (i.e. 1.5T or 3.0T), these spins align such that there is a net magnetization vector in line with the direction of the B_0 field (the static field). This is the equilibrium state from which MRI images can be produced.

A change in signal is produced when there is a change in the magnetic field. Such desirable changes come from smaller radio-frequency (RF) pulses produced by imaging coils within the hardware of the MRI scanner system or specialized anatomic-site-specific coils (e.g., a quadrature knee coil). Currents are applied through the imaging coil that oscillate at the Larmor frequency ($\omega_0=\gamma B_0$), which causes an induction of a B1 magnetic field to cause the proton spins to precess from the equilibrium state and down toward the transverse plane. Antennas are also located within these imaging coils, which measure induced RF currents of these spins as they return to their original state, and thus are able to make measurements and MRI images. Slice selection and other spatial encoding (phase and frequency) are found by using gradient coils (G_x, G_y, G_z within main scanner), which alter the magnetic field in a controlled manner such that only signals from a desired slice are measured [47].

It is usually easier to comprehend the overall magnetization vector in the rotating frame of reference. If the observer considers themselves rotating with the proton at the same frequency (Larmor), then the magnetization vectors viewed are more straightforward (Figure 7). The laboratory frame of reference, which remains motionless, is also used but may be more difficult to interpret since precession is actually shown. The rotating-frame of reference will be used in the remainder of this work.

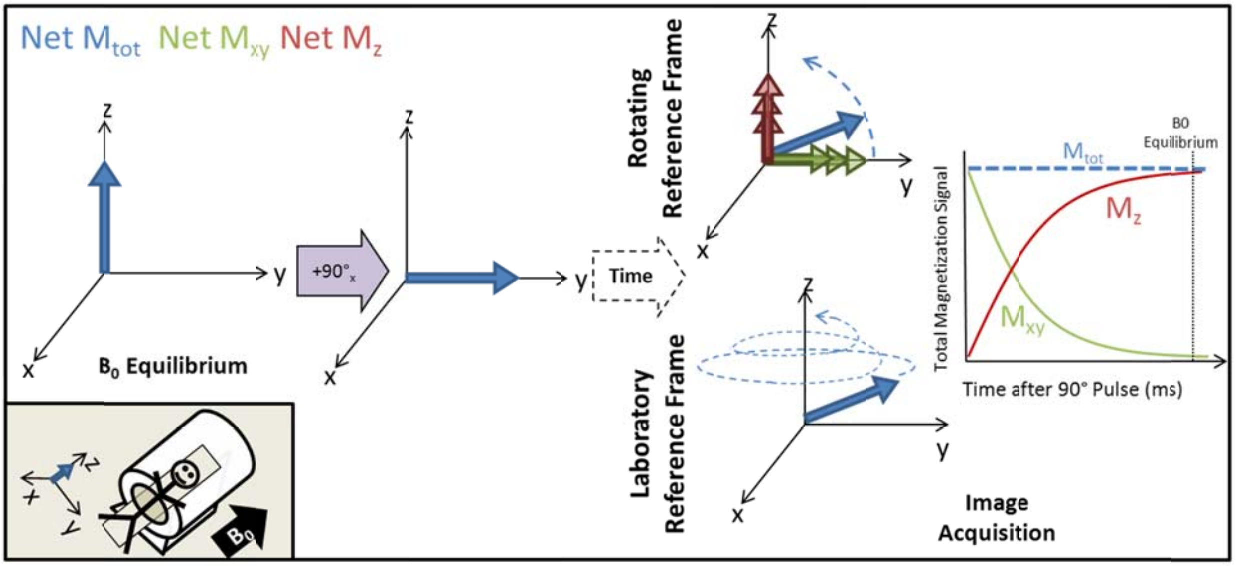

Figure 7. Basics of T1 and T2 relaxation. Consider patient orientation within the MRI scanner (inset) with regard to the conventional coordinate system used. At equilibrium, the net magnetization vector (blue) points along the z-axis, and when excited by a 90° B_1 pulse (lavender), is nutated into the transverse (x-y) plane. The B_1 pulse is turned off, and as time progresses, signal in the transverse plane decays (green) as signal in the longitudinal plane (red) returns back to equilibrium. The rotating frame is typically used, even though both are showing the same thing in this diagram (synthesized based off of Prince [7]).

There are two basic forms of relaxation that occur after an application of a B_1 field (RF pulse) to systems. One is transverse (spin-spin) relaxation, which is typically called T2 relaxation (Net M_{xy} in Figure 7). The other is longitudinal (spin-lattice) relaxation, which is typically called T1 (red Net M_z in Figure 7). In reality, what is measured is T2* decay, a combination of T2 and noise, but through the use of echos, true T2 can be measured. Behavior of these relaxation mechanisms can be characterized by the Bloch Equations below [7].

$$\frac{\partial}{\partial t}\begin{pmatrix} M_x(t) \\ M_y(t) \\ M_z(t) \end{pmatrix} = \gamma\begin{pmatrix} M_y(t)B_z(t) - M_z(t)B_y(t) \\ -M_x(t)B_z(t) + M_z(t)B_x(t) \\ M_x(t)B_y(t) - M_y(t)B_x(t) \end{pmatrix} - \begin{pmatrix} \frac{1}{T2}M_x(t) \\ \frac{1}{T2}M_y(t) \\ \frac{1}{T1}(M_z(t) - M_{0z}) \end{pmatrix}$$

In these equations, *B* is the sum of both the static and RF field components, *t* is time, and the net magnetization vector is characterized by *M* components. The directions are shown in Figure 7. To simplify these equations, consider the situation in Figure 7, with transverse plane magnetization magnitude (M_{xy}) instead of a combination of two vectors (M_x, M_y). One $\pi/2$ pulse is applied by the B_1 field, which causes the net magnetization vector to nutate into the transverse plane. After the B_1 pulse is turned off, relaxation (in the rotating reference frame) can be characterized by these simplified Bloch equations:

$$\begin{array}{c} \mathit{Transverse\ Relaxation} \\ \mathit{Longitudinal\ Relaxation} \end{array} : \begin{array}{c} M_{xy}(t) \\ M_z(t) \end{array} = \begin{array}{c} M_{xy}(0)e^{-t/T2} \\ M_0\left(1 - e^{-t/T1}\right) \end{array}$$

These characteristic relaxation behaviors are common contrast mechanisms in MRI known as T1-weighted and T2-weighted. The reason these behaviors are useful is that for a given tissue at a given field strength, the T1 and T2 time constants are consistent, and thus provide a measure of a tissue's characteristic MR properties [23]. Since different tissues have different time constants, this results in different signal intensities in the reconstructed image, and thus contrast between tissues may be achieved. An example of a different contrast mechanism commonly employed in knee imaging is fat suppression (most common lipid suppression), which affects the overall dynamic image range because the contrast is increased between lipid- and non-lipid-containing tissues [23]. Careful manipulation of imaging parameters (i.e. performing a T1-weighted image instead of a T2-weighted image) results in different tissue contrasts, which is the reason MRI performs well for distinguishing soft tissues, and is often helpful for gathering complementary information for diagnostic purposes.

Like other imaging modalities, there is both signal and noise within the reconstructed image, and it is important to be able to differentiate between the two. Signal-to-noise ratio (SNR) is theoretically proportional to the main B_0 magnet strength, and when there are more protons with a higher gyromagnetic ratio (i.e. $\gamma^{H} > \gamma^{Na}$), a greater signal intensity will be found compared to the inherent noise [48]. In other words, the greater the SNR, the easier it is to distinguish the tissue of interest from the noise (background) once images are reconstructed. This would mean that a two-fold increase in SNR would be expected when comparing images taken at 3.0T to 1.5T. However, it has been found that SNR can be increased three-fold between these two B_0 magnet strengths when an optimized coil design is used [49]. This demonstrates that coils can play a major role in SNR and overall image quality. Another example was a study by Lutterbey et al., which found that even a 1.5T image (with a knee coil) had greater SNR than a whole body scan (no coil) at 3.0T [50].

Imaging artifacts are another form of “noise” in all images. Some artifacts within MRI images include motion artifact (i.e., patient moves during scan), and inhomogeneities within either the B_0 or B_1 fields. Susceptibility artifact is an inhomogeneity in the main magnetic field which is induced by metal [48]. One solution for artifact correction is using a higher readout bandwidth [48]. A very MRI-specific artifact is what is known as the “magic-angle effect”. This artifact is associated with tissues oriented at 54.44° to the B0 magnetic fields, and higher intensities may be artificially encountered when using short echo time techniques, like proton-density, T1-weighted, and T2 mapping sequences [23, 28, 36]. This is due to collagen alignment’s effect on the efficiency of the T2 dipole interactions, which manifests in vertical striations within the cartilage image [43]. It has also been shown to be present in tendons and other highly-organized collagenous tissues in T2-mapping [51]. Some theorize that T1rho may be affected by magic angle effect [28], but others have reported that T1rho eliminates residual dipolar interaction (magic angle effect) as long as the spin-lock amplitude is greater than that of the residual dipolar interactions [3]. Whether or not T1rho is affected by magic-angle effects remains to be determined.

2.3.2. Cartilage-Specific Sequences: Morphologic Imaging

Within this section, some basic morphologic sequences will be discussed along with some studies' results. Since the focus of this work is T1rho, quantitative imaging will be discussed in more detail. Nevertheless, since these sequences are commonly used for later-stage OA diagnosis, their omission would detract from overall understanding of MRI clinical diagnostic capabilities.

Some of the most commonly used fast-spin echo (FSE) morphologic sequences are 2d proton density (PD) and T2-weighted FSE. Common gradient echo sequences include fast low-angle shot (FLASH) and 3D spoiled gradient (SPGR) sequences [22]. 3D FSE has flip angle modulation to reduce blurring and parallel imaging to reduce imaging time, so that isotropic imaging might be more clinically feasible [23]. The 2D FSE is already an important tool in the clinic, but like many other 2D sequences, it suffers from anisotropic voxels, gaps between slices, and partial volume effects [23].

3D spoiled-gradient-recalled echo (SPGR) sequences are currently the standard for morphologic imaging [23]. However, drawbacks of SPGR sequences include unreliable contrast between cartilage and fluid, being prone to metallic artifact, long imaging times, and poorer meniscal or ligament tear diagnostic capabilities compared to spin-echo sequences [23, 48]. Steady-state free precession (SSFP) has been shown to have better SNR and speed compared to SPGR imaging, but unfortunately is sensitive to B_0 off-resonance artifacts [52].

Precision of 3D-gradient-echo sequence with a selective water excitation (FLASH) was proven to be unaffected by artifacts arising from scanner drift, or scanning (i.e., humidity) and patient (i.e., activity levels) conditions in a long-term longitudinal study [27]. This, along with 3D SPGR, has been shown to be good for cartilage volume and surface measurements, but pathology (i.e., fissures) visualization may be limited by bright cartilage signal; therefore intermediate-weighted FSE sequences might be easier for visualization of internal cartilage pathology [22].

Double-echo steady-state (DESS) is another morphometric sequence which is widely used. This is one of the primary Osteoarthritis Initiative morphologic sequences [44]. This sequence, a mixture of T1 and T2*-weighted, performs similarly to 3D FLASH in its lesion detection abilities, and has similar cartilage signal as SSFP sequences [22]. This sequence is also better for diagnosis of cartilage softening compared to purely T2-weighted sequences, but is poorer at distinguishing surface abnormalities [22]. Other morphologic sequences that have been investigated include vastly interpolated projection reconstruction (VIPR), driven equilibrium Fourier transform (DEFT), and balanced SSFP [23].

There are conflicting opinions on cartilage morphometric changes and the time appropriate to view them post ACL-rupture. One report found that high-risk populations show a difference in cartilage thickness in as little as one year [23], whereas another reported that significant changes are not present even seven years after ACL reconstruction [38]. Other differences in cartilage morphometry have been reported besides changes due to disease state. Measurements of cartilage volume may have more variation due to joint size than that found in cartilage thickness measurements, so some studies have normalized 3D volumetric patient data based on the maximal epicondylar distance [39]. Patient exercise may also play a role in cartilage morphology. In the study by Stahl et al., sedentary controls tended to have larger cartilage volume in the medial tibial plateau, but none of the other compartments' volumes were significantly different when compared to healthy active subjects or mild OA subjects [39]. No matter the cause of variation in cartilage morphometry, one recent study proposed that three measures (total area of subchondral bone (tAB), percent of subchondral bone area that is denuded (dABp), and mean cartilage thickness over tAB (ThCtAB.ME)) may explain nearly all of the variation seen in morphologic measures as observed in longitudinal studies of the knee [30, 45]. Perhaps such measurements will help monitor patient progression and multi-center research collaborations.

2.3.3. Cartilage-Specific Sequences: Quantitative Imaging

Relaxometry is one common MRI technique for quantitative diagnosis, with some others including magnetization transfer and spectroscopy [53]. Most methods discussed in this section use relaxometry in order to create the images (relaxation maps) which contain the biochemical quantitative information. Changes in mobile ion concentration, which MRI is capable of capturing through relaxometry, would reflect proportional PG changes [35]. Measurement of relaxation rates (relaxometry) is performed by capturing at least two images, changing an imaging parameter (echo time or spin-lock time, T2 and T1rho respectively), and using an RF pulse to excite nuclei and then measure the relaxation back to equilibrium state [53]. Sodium and delayed gadolinium-enhanced MRI will be briefly discussed, followed by T2-mapping and T1rho. Since the latter two are at the forefront of current clinical application, comparisons between these sequences will also be discussed.

While other methods presented in this section rely upon hydrogen spins, sodium mapping does not. As the name implies, Na^{23} is another nucleus that can be useful for cartilage imaging, having a concentration of approximately 320mM and T2 relaxation times of 2-10ms [23]. Since sodium ions are attracted to negatively charged GAG molecules, it follows that sodium imaging would allow direct quantification of GAG content. Sodium mapping, while having a high specificity to the GAG concentrations, lower resonant frequencies, concentrations, and shorter T2 relaxation (compared to H^1 imaging), is not used in the clinic because it requires specialized hardware and higher magnetic field strengths because of low SNR and low spatial resolution [20, 23, 35].

Delayed gadolinium-enhanced MRI of cartilage (dGEMRIC) measures the fixed charge density of cartilage, which is mainly attributed to GAG concentration [21]. This type of quantitative imaging sequence usually utilizes SPGR T1-weighted maps [23]. Images are acquired ninety minutes after injection of the GAG-affinitive $Gd\text{-}DTPA^{2-}$ contrast agent, which should distribute evenly within this time from both the bone-cartilage and synovial-cartilage interfaces [20]. One assumption that might introduce very small quantitative errors to this sequence is relaxivity of Gd would be the same as in saline [54]. Nevertheless, a potential setback to dGEMRIC imaging has been the discovery of nephrogenic systemic fibrosis in a small fraction of renal failure patients who were subjected to gadolinium-based imaging studies. While most complications documented were associated with gadadiamide, there were some reactionary cases involving gadopentetate dimeglumine (Magnevist) injections, which led to the Food and Drug Administration mandating a warning on all five of the approved gadolinium-based agents [55]. dGEMRIC, while GAG-specific, may not be as clinically viable due to a long waiting period between injection and imaging, and the technique's documented side-effects.

T2 mapping of cartilage has been under investigation since 1989, and reflects water-water as well as water-macromolecule interaction effects in moving and exchanging of energy, with an inverse relationship between the amount of such interactions and the resulting T2 parameter (high interaction = low T2) [20, 39]. In short, T2 is sensitive to tissue hydration [41]. To measure T2 relaxation with high accuracy, care needs to be taken when using a multi-echo spin-echo technique, and whether a mono-exponential or multi-exponential decay model is needed based on the imaging parameters [23].

T2 relaxation is also sensitive to the tissue's architecture; regional and zonal differences in the type-II collagen fibers may be visualized on some of these images [20]. One polarized light microscopy study demonstrated that approximately 40% of the depth-wise variation in T2 relaxation time was attributable to collagen fibril alignment to the B_0 field [28]. T2 has also been shown to be inversely correlated with cartilage volume and thickness [41]. These insights were correlated to cartilage mechanical properties in a study which showed that patellar T2 relaxation time is correlated to its Young's modulus [32]. It has been shown that there is an increase in T2 relaxation time in osteoarthritic knees compared to normal, but differentiation of mild versus severe OA cases was not possible [43, 56]. This lack of differentiation may be attributable to T2 relaxation times correlating poorly with respect to PG content, which is known to change during OA progression (PG cleavage did not affect the values significantly) [56]. This poor correlation was further demonstrated in that T2 was not significantly correlated with GAG content, except when full thickness region-of-interest measurements were made [28].

Spin-lattice relaxation in the rotating frame, or T1rho, was first described by Redfield in 1955 with experiments on aluminum and copper [57]. Decades passed prior to T1rho research in biological tissues (1974), which has since evolved into the quantitative cartilage-specific sequence used today [58]. T1rho has also been of interest outside of the cartilage imaging community, and has been investigated for changes in brain chemistry for Alzheimer's disease, and tumors [35, 59].

T1rho relaxation is dependent on both the static magnetic field strength (B_0), and the RF pulse (B_1, which is set to a frequency ω_1). T1-dispersion occurs when a sequence's relaxation time is dependent on the static field strength [8, 54]. Theoretically, different field strengths will produce different T1rho relaxation times, which is a motivating factor for some of the B_0 comparisons in the present work. Inhomogeneities in the static field may also result in localized T1-dispersion artifacts. However, it was found that small off-resonance artifacts (<=25Hz) only affected T1rho relaxation times by +-2 to 7ms, at least within a carrageenan-agarose phantom [60]. It has been shown that these static magnetic field inhomogeneities may be reduced with the use of turbo spin-echo with inter-echo spacing [48].

Dependence on ω_1 (a.k.a. T1rho dispersion) has been found for T1rho. As ω_1 tends toward zero, then 1/T1rho is identical to 1/T2 [24]. In other words, as the spin-locking pulse goes toward zero, the behavior of T1rho tends to be more like T2 relaxation. In one study by Duvvuri et al., T1rho relaxation times spanned from ~60-130ms in bovine patellar specimens as the SL pulse's frequency was varied from 0.1-10kHz [61]. Each tissue may have different T1rho dispersion behavior [62]. Because of T1rho's B_1 sensitivity, hardware with good B_1 homogeneity is essential for image quality [63].

B_1 inhomogeneities and their resulting artifacts can be compensated for by using a self-compensating spin-lock pulse [64]. This pulse sequence, which is used in the present work (Figure 8), begins with 90° hard pulse, which nutates the magnetization vector from its equilibrium position. The spin-locking pulse is applied in the transverse plane for a specific duration (SL time), causing the component aligned with the spin-locking vector to decay at a time constant of T1rho. Next, another pulse (-90°) is applied along with a crusher gradient, resulting in removal of transverse magnetization. The remainder of the longitudinal magnetization is sampled and an image is created using a fast-spin echo sequence [64]. T1rho decay is similar to T2* decay (bottom panel Figure 8), except for the additional “spin-lock” RF pulse [20]. Hence, previous studies’ T2 decay and curve-fitting findings are used as a basis for some of the work presented here regarding curve-fitting algorithms during relaxation mapping, since these are new investigations with regards to T1rho (to the author’s knowledge).

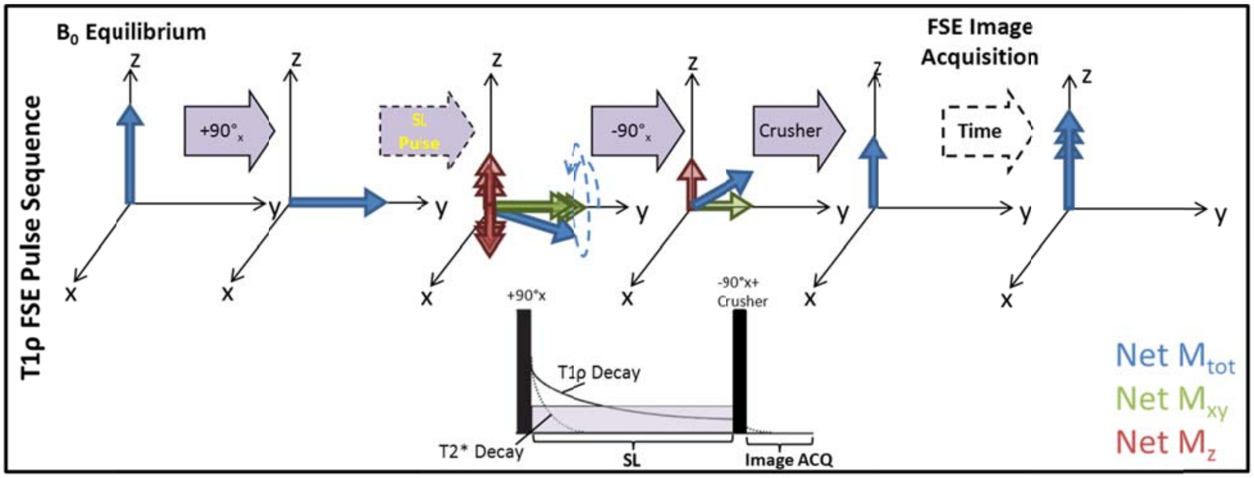

Figure 8. Vector diagram showing the net magnetization forces seen at each of the various stages of the T1rho pulse sequence used in the present work. The diagram on the bottom shows how decay is slowed (T1rho) by the spin-lock (SL) pulse, compared to regular T2* decay (bottom diagram adapted from Borthakur et al. [19]).

A concern with T1rho is the potential for high energy deposition during the application of the spin-lock pulse, and so extra attention must be paid to the specific absorption rate (SAR). SAR limits for each gram of tissue are enforced by the Food and Drug Administration in MRI, because the absorbed RF power causes an increase in local tissue temperature [35]. Whole body

SAR is averaged over the entire body of the patient over a span of fifteen minutes, but maximum allowable power deposition is 12 W/kg per five minutes of scan time for the extremities [65]. SAR depends on static field strength, conductivity of the tissue being sampled, the tissue geometry, and in T1rho, the spin-lock duration [35]. In Regatte et al.'s experiment, it was found that as long as ω_1 was less than 750Hz, the SAR levels would not be exceeded in human studies [24]. Such precautions have been taken to adhere to these limits within this work and others' research in T1rho [54].

T1rho measurements are thought to probe the slow molecular interactions that occur within the 0-100 kHz range (due to B_1 dependence), whereas T2 measurements are more dependent upon the B_0 field, and thus probe interactions in the MHz range [20, 42]. Proposed molecular interactions that T1rho captures are hydroxyl proton exchange, molecular motions, amide proton exchange, and inhomogeneous field diffusion [8]. More interestingly, though, T1rho relaxation measurements were found to be increased in osteoarthritic subjects and with increasing grades of OA [39], which corroborated with radiographic grading [3, 56]. Many studies have found that there is at least some depth-wise variability in T1rho relaxation times [24, 25, 28, 38, 54, 61, 62, 66], with some studies further specifying that this variability corresponded to a variable zonal PG/GAG content [25, 28, 54, 61]. It is hypothesized that there are several factors which contribute to variation in T1rho, including physical activity levels, collagen fiber orientation and concentration, proteoglycans, and some other unidentified macromolecules [20, 39]. While it is unknown what T1rho is measuring *exactly*, a case study highlighted its unique diagnostic abilities, when a T1rho "lesion" was confirmed to be a structural cartilage lesion during arthroscopy; this lesion was not evident on the other collected MR sequences [67].

Duvvuri et al. were one of the first groups to investigate T1rho's OA-diagnostic capabilities at 1.5T *in vivo*. Since T1rho was still relatively new to the cartilage realm, Duvvuri and colleagues made comparisons of it to T2 in six subjects. They found that T1rho relaxation times are usually longer than T2 relaxation times, and that the former have a 20%-25% (normal and tissue lesions) higher SNR. However, signal-difference-to-noise ratio (SDNR) between cartilage and fluid in T1rho was approximately 13% smaller than that found in T2 [62]. In Duvvuri et al.'s next set of experiments, PG was incrementally digested in bovine cartilage, and then T2 and T1rho relaxation measurements were made [8]. That study found that increases in T1rho relaxation times correlated with PG loss (R^2=0.81), with a 15% PG loss resulting in an 8% increase in T1rho relaxation. T2 was less correlated to PG loss (R^2=0.65) [8]. Wheaton et al.'s work also found a similar relationship in fixed charge density (directly related to GAG content), with the percentage change in T1rho relaxation rate correlating (R^2>0.85) in both bovine and human cartilage samples [63]. T1rho relaxation rates were also strongly correlated with biomechanical properties [25]. Other comparisons between T1rho and T2 demonstrate that T1rho has greater SNR, improved fluid and fat saturation signal suppression, reduced diffusion-induced signal losses, reduced susceptibility artifacts (metal-induced B_0 inhomogeneities), less orientation dependence (relating to magic angle), and higher chondral defect sensitivity than T2 [3, 20, 54].

T1rho thus may prove to be a more GAG-sensitive measure than T2 [39, 56]. A recent study by Keenan et al. found that cadaveric patellar tissue samples with decreased GAG content had increased T1rho relaxation time, despite these same tissues still being within the "normal" T2 relaxation range [28]. This corresponds to the findings of Regatte et al., who found that T2 relaxation times nearby to a full-thickness cartilage defect were essentially normal, whereas the T1rho relaxation times in the same region were 95% higher than baseline values [3]. And within an *in vivo* ACL-rupture patient experiment by Li et al., T1rho values varied over the course of a year, and were significantly different than in normal subjects, yet T2 values were not significantly different between the two groups [66].

2.3.4. MRI in the Clinic: Considerations and Correlations Across Centers

Some standard cartilage-dedicated sequences include the morphometric proton density-weighted fast spin echo, T1-weighted spoiled gradient echo, and fat-saturated T2 weighted sequences [56]. While these sequences are useful for later-stage OA detection and for pre-operative planning, early biochemical OA changes are detected in the quantitative sequences. Currently, T1rho is not prevalent within clinical scanners, but since it requires no special hardware (sequence slightly deviates from a standard spin-echo sequence) and no contrast agents, it can be easily implemented [35, 63].

OA is a whole joint organ disease, so OA imaging techniques need to be able to visualize and analyze whole joints [30]. Gold et al. recommended that current clinical two-dimensional slice techniques should be acquired with 0.3-0.6mm in-plane resolution, 2-5mm thickness (many have 3mm), and multiple planes to minimize partial volume effects [22, 23]. The T1rho sequence used in this work is within these recommended resolutions, but is not captured in multiple planes. However, other sequences collected during the examination are in different planes, so these may address questions regarding partial volumes and whole-joint geometry. For early morphologic degenerative changes, that same study recommended that an in-plane resolution of 0.2-0.4mm is needed [23]. T2-weighted fat saturated images that have 0.438mm resolution may serve as a clinical morphologic dataset, since the resolution is not far from that recommendation, and since this is a typical sequence already collected during clinical examination.

A balance between resolution, short acquisition time, and signal-to-noise ratio (SNR) must be achieved in MRI. As a general rule of thumb, two out of these three desirables are achievable. This is based on the fact that SNR is roughly proportional to voxel size multiplied by the square root of the acquisition time [68]. So, if one desired high SNR and small voxel size, as in a research setting, the acquisition time would need to be long. In contrast, within a clinical setting, imaging time needs to be kept at a minimum (so as to have high patient throughput), with "good-enough" diagnostic results. Therefore, high-resolution clinical images are still limited *in vivo* by the total SNR available (in order to minimize acquisition time) [23]. Even with available higher resolution sequences, motion artifact and long imaging sessions reduce the quality and clinical utility of such images [22]. Some of the methods that have been investigated to speed up acquisition time and reduce specific absorption rates (SAR) are parallel imaging, hybrid gradient-echo/spin-echo, partial k-space (keyhole) sampling, using eight-channel phased array coils, and others [20]. One parallel imaging study found that at 3.0T, parameters were approximately the same as those found with a conventional coil and T1rho and T2 pulse sequence [69].

One way to improve SNR without affecting voxel size or data acquisition time is to use a larger B_0 field. In fact, low field strengths (<1.0T) are not recommended for assessing cartilage morphometry, due to errors in detecting less-than-full-thickness lesions; therefore, 1.5T has been the clinical standard [22]. On the other hand, larger B_0 magnets (>3.0T) may provide information about cartilage ultrastructure with greater resolution and shorter scan times than most clinically available systems, but these larger magnets are more expensive, and also have radiofrequency penetration and high power deposition problems, which would inhibit clinical T1rho imaging [23]. So far, improvement in OA diagnosis has not been found when comparing 7.0T to 3.0T systems [22]. This suggests that these higher field strengths really have little clinical advantage over 3.0T systems. Therefore, this means that magnetic field strengths between 1.5T and 3.0T are likely to remain the main clinical workhorses.

Several studies have investigated MRI sequences in both 1.5T and 3.0T systems. However, there have been no previous studies which have compared T1rho at both 1.5T and 3.0T at the same time. Therefore, these comparative morphological sequence studies provide guidance and a basis for what might be expected when comparing T1rho at both field strengths.

When Kornaat et al. compared SPGR and SSFP on both 1.5T and 3.0T systems, they discovered that SNR and contrast-to-noise ratio (CNR) both increased for the higher system, yet the morphologic measurements were not significantly different between the two [52]. Link et al.

also compared SPGR to PD images on both 1.5T and 3.0T, but assessed cartilage lesion detection for both sequences. After radiologists examined the 27 porcine knees, it was determined that SPGR was superior to both the high resolution (0.20x0.26x2mm)and low resolution (0.31x0.47x3mm, worst scoring) PD images on both systems, using receiver operator characteristics (ROC) analysis [46]. Kijowski et al. compared several different morphometric sequences (axial T2-weighted, coronal T1-weighted, coronal intermediate weighted, sagittal intermediate-weighted, and sagittal T2-weighted with fat suppression) in terms of their sensitivity, specificity, and accuracy for detecting lesions in 200 patients at 1.5T and 3.0T. They found that all measures (sensitivity, specificity, accuracy) were improved at 3.0T (70.5%,85.9%,80.1%) compared to 1.5T (69.3%,78%,74.5%) images. These results were likely due to the increased SNR seen when a higher B_0 magnetic field strength is used, so it was easier for the radiologists to visualize what was a lesion and what was not [70].

An improvement in accuracy errors was also seen in Bauer et al.'s experiment, when examining cartilage volume at 3.0T (3% errors) compared to 1.5T (16% errors) in SPGR images [49]. Lesions were also investigated in Saupe et al.'s experiment of 10 cadaveric wrists in intermediate-weighted FSE and 3D GRE sequences, at both 1.5T and 3.0T. The inter-observer agreement of lesion location was greater (but not significant) at 3.0T compared to 1.5T [71]. Since cartilage in the wrist is much thinner than that in the knee, it may have been easier to misjudge a lesion at either 1.5T or 3.0T. Metal artifact is common in musculoskeletal imaging after reconstructive surgery. To assess susceptibility to metal artifact and other qualitative imaging characteristics, Farraly found that for GRE sequences at both 1.5T and 3.0T, increased readout bandwidth improved artifact from the titanium plate [48].

Overall, improvements to SNR, CNR, specificity and sensitivity were found when examining the same specimens at 3.0T compared to 1.5T. However, the 1.5T images were still useful in their ability to perform diagnostic measures. 3.0T systems are becoming more common, but since many imaging centers in the United States still have 1.5T systems, knowing whether there is useful information to be garnered at 1.5T is important for early patient care, diagnosis, and preventative measures. Now that current clinical practices and considerations have been introduced, the two tools used in this work for analyzing T1rho will be presented. Their application to the clinically relevant PTOA model (ACL rupture) will be addressed, and the questions regarding T1rho's potential for migration into clinical settings will be investigated.

CHAPTER 3: CONSIDERATIONS IN MRI RELAXATION CARTOGRAPHY

3.1 An Introduction to MRI Relaxation Mapping

Capturing tissues' MRI relaxation properties, which correlate to the underlying physical and biochemical constituents, is done through a process typically referred to as "relaxation mapping", or relaxometry. This procedure is typically done in quantitative imaging, such as T2, dGEMRIC, and T1rho. While there have been many studies which discuss the optimal parameters and fits in T2 mapping [72-77], there have been far fewer which have grappled with the same concepts in T1rho [19, 59]. Previous studies have found that relaxation times are sensitive to the controls used during image collection and post-processing (i.e. curve-fitting and model selection, [53]). To structure this chapter, it is hypothesized that the number, combination, and spacing of the data points to be included, the model, and the type of fitting procedure used will ultimately affect what T1rho relaxation values are found from the curve fit. Since all of the reported T1rho relaxation values in the present work are dependent upon this mapping process, this chapter discusses issues pertaining to optimal T1rho relaxation map creation.

A brief overview of how relaxometry works to create the T1rho relaxation values is necessary to understand the rigor involved in each of the following subsections (Figure 9). To make a T1rho relaxation map, a set of images with varying SL times need to be acquired. Once that is done, the images are registered to one another so that a voxel in one image has the same location in all other images within that dataset. Curve-fitting needs to be performed on a local, voxel-by-voxel basis to acquire the properties of a particular tissue. A single exponential decay curve is fit to the data, and the constant found from this fit is stored in the resulting map image as that voxel's T1rho time. This process is repeated until all voxels within the image have been analyzed, resulting in the T1rho relaxation map. Each step (except image acquisition) was performed using the 7.8.0 (R2009a) version of MATLAB (The MathWorks, Inc ., Natick, MA).

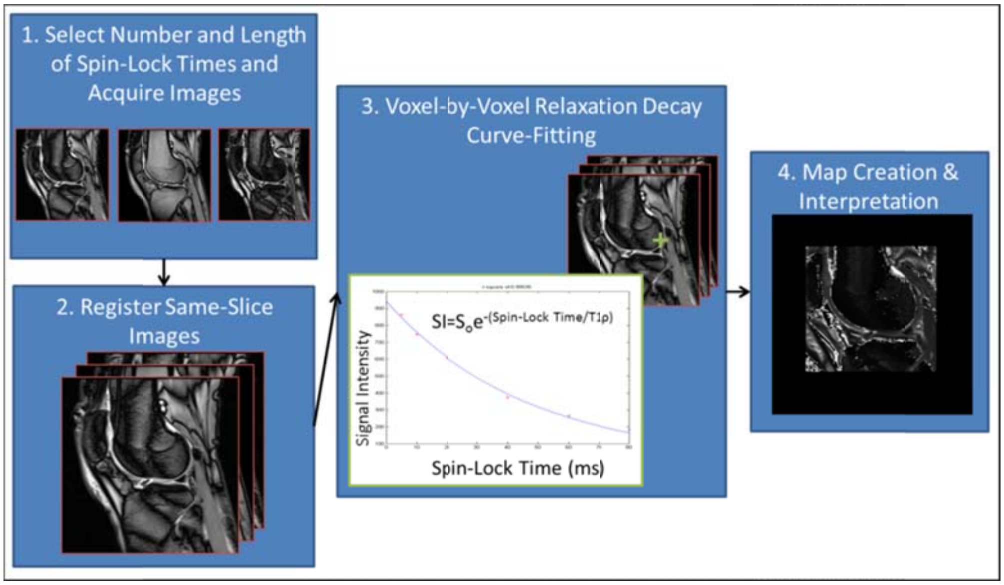

Figure 9. An overview of how a T1rho relaxation map is made.

After the registration of same-slice images (Section 3.2) and exponential model selection (Section 3.3) have been discussed, the driving hypothesis of this chapter will be addressed by the individual hypotheses:

A) Different curve-fitting procedures will produce different T1rho relaxation times (Section 3.4).

B) Different spin-lock combinations produce different T1rho relaxation times (Section 3.5).

C) Better similarity to "full data-capture" is accomplished with more spin-lock image captures (Section 3.5).

D) The same spin-lock combinations on 1.5T and 3.0T will describe T1rho relaxation accurately (Section 3.5).

E) Non-linear (exponential) spin-lock time spacing is a better sampling scheme than linear spin-lock time spacing (Section 3.6).

These are several motivations for these hypotheses, the first being that different research centers currently use slightly different methods for their cartilage imaging experiments. For standardization, such that T1rho relaxation times from multiple research centers can be compared, it is imperative to determine whether or not the resulting relaxation times are affected by these slight differences (curve-fitting procedure, number and combination of spin-lock images captured, spin-lock time spacing). If it is found that some of these differences do affect the resulting T1rho values, then it should be determined what parameters should be used on both research (3.0T) and clinical (1.5T) field strengths, so that T1rho can be used and compared in both settings.

Statistical analyses were employed to verify and determine some of the results found in this chapter. One such analysis was applied during the various curve-fitting explorations to measure the proportion of the variability among the dependent variables that is explicable by the least-squares linear regression (R^2) of the dependent variable (i.e. signal intensity) on the independent variable (i.e., spin-lock time) [78]. In essence, this R^2 measure is used frequently to describe how well a particular analysis (i.e. an exponential curve-fit) interprets the observed data. R^2 is calculated by using the mean of the dependent variables (y_{mean}), the dependent variables observed (y), and the determined dependent values of the fitted model (f). These values are used for every ith data point (where there are n observations) in the model, such that an R^2 value is determined from the following sets of equations:

$$SS_{tot} = \sum_{i}^{n} (y_i - y_{mean})^2$$

$$SS_{err} = \sum_{i}^{n} (y_i - f_i)^2$$

$$R^2 = 1 - \frac{SS_{err}}{SS_{tot}} = 1 - \frac{SS_{err}/n}{SS_{tot}/n}$$

Other statistical tests incorporated in this chapter and used in some other portions in this work are the student’s t-test with equal variance and the one-way analysis of variance (ANOVA) test. The student’s t-test is appropriate when testing the null hypothesis (H_o) that the mean from one group (μ_1) is equivalent to the mean of another (μ_2). If equal variance is assumed, then this means that the populations are assumed to have a normal distribution, and thus the variances are equal as well. If *p*, the probability of observing a discrepancy between the two groups as large as x_{mean1}-x_{mean2}, is less than the desired α (usually 0.01 or 0.05), then the null hypothesis is rejected, and it can be said that the two groups are significantly different from one another ($\mu_1 \neq \mu_2$). The population sizes in the student t-test do not need to be the same size to make a single comparison [78].

A one-way ANOVA test is similar to the student's t-test, but it is used in instances where the null hypothesis is H_o:$\mu_1=\mu_2=\ldots=\mu_k$ for more than just two groups. However, if H_o is rejected, then one can only conclude that the population means are unequal. In order to determine which of the groups were significantly different, a Tukey's honestly significant difference criterion was used in this work. It is optimal for cases with equal sample sizes, is based on the studentized range distribution, and provides a correction such that a type I error is found only at the α value, instead of an α value which is inflated due to multiple comparisons [78],[79]. Therefore, the one-way ANOVA test with Tukey's honestly significant difference criterion was used in the cases where sample size between groups was the same, whereas a simple student t-test was used to determine similarity between groups of unequal sample size.

One way to try to maintain similar data comparisons across magnetic field strengths is to use a control, such as the phantom that was used in the present work. An agarose-carrageenan gel phantom was built for in-house MR scanner calibrations and imaging experiments, similar to a previous concentric-ringed design [60]. Like other cartilage-surrogate phantoms [80], the proportion of gadolinium trichloride ($GdCl_3$) and agarose were varied between the concentric rings to provide various contrasts and T1rho signals typically seen within *in vivo* cartilage (Figure 10). 1% carrageenan concentration was present throughout the various rings' gels. The central core consisted of lipid (lard), so as to provide a simulation of the fat seen in bone marrow. The 15 cm diameter frame containing the various gels was composed of (MRI-compatible) Plexiglas.

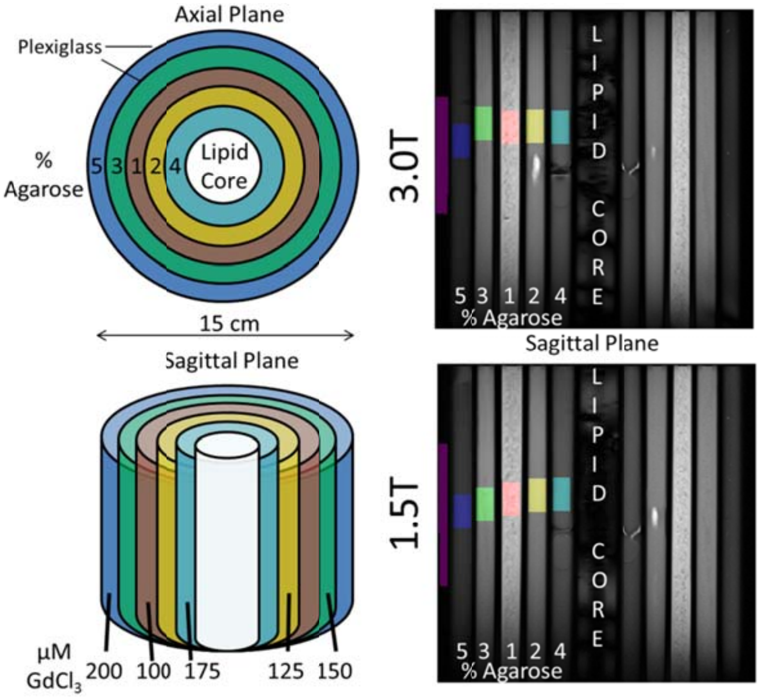

Figure 10. Schematic (left) showing concentric-ringed, carrageenan-agarose phantom used in this work. The midline 20 ms T1rho images for the 1.5T and 3.0T scans are shown at right.

The phantom was used for several parts of the present work, for various reasons. First, it affords consistency for measuring T1rho relaxation times. There is no day-to-day variability, as would be seen in living subjects. Second, no motion is possible, thereby guaranteeing that exactly the same in-plane samples will be sampled during relaxation curve-fitting within a given scan session (i.e., no out of plane movement is possible). Third, since it also has large homogeneous gels for sampling T1rho relaxation, consistent direct comparisons can be made between scanning sessions and scanners. Also, due to its size, it loads the entire knee coil, which is similar to the nearly full coil loading that would be seen during an *in vivo* scan. Another attraction for its use is that in some longer imaging experiments, specific absorption rates (SAR) for a living subject could be exceeded. By using the phantom, preliminary experiments could provide guidance to future *in vivo* imaging sessions, with regards to such things as the proper spin-lock combination, or how to deal with B_0 field inhomogeneities. Of course, this assumes that the phantom's T1rho relaxation behavior is broadly similar to that of cartilage. While not all signal components may be accounted for (i.e., interactions between proteoglycans and interstitial fluid, since PG not present in phantom's biochemical make-up), the phantom's general relaxation behavior (signal curve shape) is fairly similar to that of cartilage, with regard to the resulting T1rho relaxation time derived during curve-fitting to a mono-exponential model (more detailed explanation in Figure B-1).

3.2 Spin-Lock Images' Registration and Validation

Registration of each of the acquired SL images to a single slice location is crucial to the subsequent curve-fitting and derivation of T1rho. Misalignment can mix signals from neighboring voxels. Since articular cartilage is not an extremely thick tissue (average femoral thickness is 1.65-2.65 mm [26]), slight movements would result in inaccurate image capture of the tissue. Even though the patient's limb is restricted by the coil and technician-placed padding, slight patient movement is still possible within the acquisition time of approximately one minute per slice, per spin-lock (SL) image.

Earlier implementation of inter-image motion correction required user-intervention, and thus human error was always possible. The need for an objective automated image registration program was satisfied by adapting a multi-purpose, image registration toolkit from Matlab Central (image_registration.m, written by Dirk-Jan Kroon, Copyright 2009). Another advantage of this algorithm was that it used an optimization of a similarity metric to determine the best possible rigid transform to apply.

A rigid affine transformation was selected for registration of the SL images. This particular method only allows for in-plane rotation and translation [81]. Since all images in this work were isolated two-dimensional slices, this was the best way to correct in-plane movement. A b-spline or other three-dimensional interpolating function was not used because out-of-plane changes were assumed to be small in comparison to the entire thickness of the image slice (assumed similar scale of movement as in-plane, < 1 mm during a scan). Without T1rho information captured in three dimensions, it would be challenging to appropriately characterize such out-of-plane movements. Therefore, the general affine transform parameters (decomposed from their general form, a_x) as seen below were used to transform the “moving” image’s coordinates (x,y), to the “fixed” image’s coordinates (x’,y’) [81]. No shearing or scaling components were involved, since the patient’s knee size was assumed to not change during the course of the scan.

$$\begin{bmatrix} x' \\ y' \\ 1 \end{bmatrix} = \begin{bmatrix} a_{11} & a_{12} & a_{13} \\ a_{21} & a_{22} & a_{23} \\ 0 & 0 & 1 \end{bmatrix} \begin{bmatrix} x \\ y \\ 1 \end{bmatrix} = \begin{bmatrix} 1 & 0 & t_x \\ 0 & 1 & t_y \\ 0 & 0 & 1 \end{bmatrix} \begin{bmatrix} x \\ y \\ 1 \end{bmatrix} + \begin{bmatrix} \cos\theta & -\sin\theta & 0 \\ \sin\theta & \cos\theta & 0 \\ 0 & 0 & 1 \end{bmatrix} \begin{bmatrix} x \\ y \\ 1 \end{bmatrix}$$

The registration algorithm optimizes the found affine transformation using a similarity metric. To test which similarity metric option performed the best with the T1rho images, two image datasets (AKA 14, Normal 1’s first scan) from the midline of the lateral femoral condyle were registered to the first SL image captured (20ms image). These available similarity metrics included sum of squared pixel distance (SPD), normalized local mutual information (MI), normalized mutual information with image splitting (MIP), gradient differences (GD), normalized cross correlation (CC), pattern intensity (PI), and log absolute difference (LD). The various transformations which were applied to each of the images within a set were recorded through means of the affine registration parameters (a_x values in Table B-1).

The two image datasets were chosen for specific reasons. First, the amputee specimen was considered the control case for movement, so any affine parameters found by the various similarity metrics would be erroneous. Normal 1’s scan was a test for the sensitivity of the algorithm to movement, since movement across the set of SL images was visually detectable.

The overall average affine parameters, which indicate the detected movement and applied registration, for each of the registered SL images in the AKA specimen and Normal 1 are reported in Table B-1. Overall, the mutual information (MI) metric was found to be the best. The mutual information metric can be described by finding the rigid transform which maximizes S in the equation below, where p(x) and p(y) are the probability distributions in each of the images, and the joint probability distribution of both images is p(x,y) [82]. Ultimately, the mutual information metric produced the smallest errors in translation in the AKA dataset, and was still able to capture the motion seen in the Normal 1 dataset, based upon both the reported a_{13} and a_{23} parameters (being greater than 0) and visual affirmation of the corresponding images being aligned to the static image.

$$Mutual\ Information\ Metric\colon S = \sum_{x,y} p(x,y)\log\left(\frac{p(x,y)}{p(x)p(y)}\right)$$

Only the SL=5ms image in the AKA dataset had detected "movement" when using the mutual information metric (0.003% of the pixel size). Therefore, a movement threshold was determined and implemented for future registration of the SL images. If the detected movement in either the x- or y-translation affine variables was greater than this threshold, then the determined affine transformation was applied. If not, then the affine transformation would not be applied. It was determined from these initial datasets (AKA14, Normal 1), that the movement threshold of five percent of average cartilage thickness would be used to give some physical reference (movement threshold equates to 0.29 voxels in T1rho images). With this threshold in place, the "moved" image in the AKA specimen would be below the threshold and therefore no affine transformation would be applied. Yet, the SL=40,10,80,5ms images in the Normal 1 dataset would be transformed and registered to the 20ms image, thus correcting for patient movement.

Overall, a new registration technique was tested and validated for use in SL image registration, prior to the rest of the relaxation mapping process. This automated technique detects small movements which were previously difficult for a human user to visually discern, and uses a mutual information similarity metric to optimize the rigid, affine transformation applied. Therefore, this registration algorithm was applied to all living subjects in the rest of the relaxation map-making process of this work.

3.3 A Single or Double Exponential Model?

Model selection is important for curve fitting, since a different model (i.e., a bi-exponential model) will result in different values for relaxation time constants. In the context of T1rho mapping and curve fitting, there has not been much work within the literature regarding what exponential shape best describes T1rho relaxation. A mono-exponential curve fit has been used as the basis for several groups' work [3, 66, 83]. However, in T2 relaxation mapping (the reference for many aspects of this chapter regarding curve fitting due to its similar overall shape characteristics), there have been studies which indicate that it may be better to use a bi-exponential or even a multi-exponential curve fit as described by the equation below [84, 85]. SI refers to final signal intensity, SI_{short} and SI_{long} refer to the initial signal intensities for the constituents responsible for the $T2_{short}$ and $T2_{long}$ relaxation, and TE is echo time (the parameter varied in T2 mapping) [76].

$$SI = SI_{short}e^{-TE/T2_{short}} + SI_{long}e^{-TE/T2_{long}}$$

It would be ideal if a bi-exponential fit could capture the separate collagen and proteoglycan relaxation times and interactions, to truly elucidate the underlying biochemical properties of the cartilage. However, T1rho (spin-lattice) relaxation usually occurs much more slowly than the multi-exponential intercompartmental exchange between material transfers seen in T2 (spin-spin) relaxation, so the averaging process that occurs leads to T1rho being best described by a mono-exponential curve [77]. For such reasons, while the T1rho curve may be similar to a mono-exponential T2 decay curve, using a bi-exponential model may not be appropriate with regards to the physics behind T1rho. Therefore, investigations with the particular curve-fit parameters were undertaken for the mono-exponential decay model (below), and a mono-exponential curve was used for all curve fitting in this work. Like the previous equation, SI and SI_o refer to the final and initial signal intensities, respectively, SL is spin-lock time, and T1rho is the relaxation time constant, to be determined.

$$SI = SI_o e^{-SL/\mathrm{T1\rho}}$$

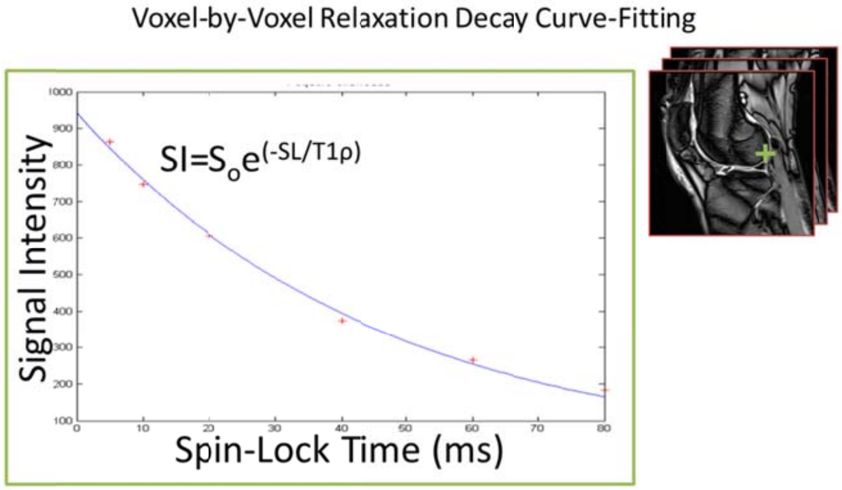

Figure 11. An exponential curve is fit to the set of signal intensities recorded at all spin-lock times for an individual voxel to determine the T1rho relaxation time. This is repeated for every voxel in the MRI sequence images.

3.4 Mono-exponential Curve-Fitting Validation

The appropriate model for relaxation measurements of T1rho has been defined as a mono-exponential decay curve. However, there are several different ways in which to fit a curve to measured data, with different criteria for each procedure possibly producing different estimations of the desired absolute relaxation time constant. Since interpretation of a patient's cartilage health is dependent upon the T1rho relaxation calculations, it follows that determination of these values should be as robust and accurate as possible.

Non-linear least squares fits have previously been used for T1rho relaxometry [62, 83]. Comparisons of fitting procedure effects have not been thoroughly investigated in T1rho, unlike for cartilage-specific T2 sequences. One study, performed by Koff et al., investigated different fitting procedures for T2 mapping using patellar cartilage from ten healthy subjects. T2 maps were made with linear, weighted-linear, and non-linear fits to a mono-exponential decay model, and the resulting fits were evaluated for goodness-of-fit with an R^2 parameter. Between the three fitting procedures used, all resulting T2 values were considered to be significantly different

($p<0.0001$). The best fit (overall highest R^2) to the relaxation data collected was found with the non-linear fit [75]. Since T2 relaxation is assumed to have approximately similar decay properties as T1rho relaxation, it was hypothesized that the type of fitting procedure used would significantly affect the resulting T1rho relaxation time (Hypothesis A of this chapter).

Normal subject T1rho image sets were utilized to test this hypothesis. The 2D midline slices (SL=5, 10, 20, 40, 60, 80 ms) of the lateral femoral condyle from the first-day scans of Normals 1 through 7 were used (APPENDIX A: Image Sequence and Patient Information).

Relaxation maps were made for each of the normal subjects using a mono-exponential model. Since Koff et al. found that non-linear fits had the highest-scoring R^2 values, only non-linear, least square (NLLS) fits were considered. Several variations of this fit were implemented. First, two different robustness measures were incorporated to the NLLS fit. Least Absolute Residuals (LAR NLLS) is a particular robustness measure which minimizes the absolute difference of the residuals, whereas the other robustness measure, Bisquare Weights (BiSq NLLS), minimizes a weighted sum of the squares [79]. These three fit types (NLLS, LAR NLLS, BiSq NLLS) all had uniform weighting, but non-uniform weighting was also tested. For each of the following equations, W_i is the weight factor that is applied to the i^{th} datapoint (SL_i image's signal intensity at a particular voxel), and n = number of datapoints (SL images) acquired. Chi-weights (ChiWi) and squared signal intensity weights (SqSI) were both described by Koff et. al., and their weighting was determined as [75]:

$$ChiWi\colon W_i = \frac{1}{var(\log SI) * \log(SI_i)}$$

$$SqSI\colon W_i = {SI_i}^2$$

$$SI\ Weights\colon W_i = \frac{SI_i}{\sum_{i=1}^{n} SI_i}$$

Using these different fitting parameters, the maps were made for each of the normal subjects. The R^2 statistic was also reported for each voxel's curve-fit. Once the maps and corresponding R^2 had been calculated, full thickness cartilage regions of interest (ROI's) were selected from 0-90° from the posterior ridge based upon line profile analysis results (Figure B-2). Voxel intensity distribution statistics were measured for each map (or R^2) image within each ROI. A one-way analysis-of-variance (ANOVA) test and Tukey's honestly significantly different criterion was used to make comparisons between the different fit methodologies (n=2220 voxels, Figure 12).

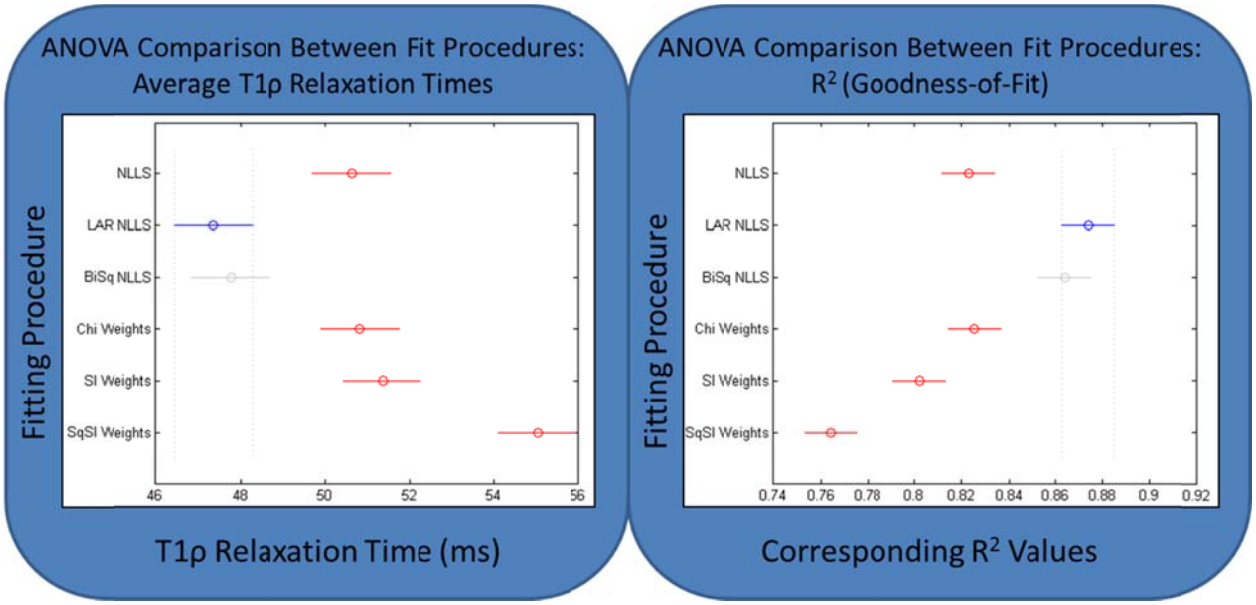

Figure 12. The results of the ANOVA and Tukey's honestly significant different test for the various fitting algorithms' effects on the T1rho relaxation parameter, and how well the particular algorithms fit the data (shown by the R^2 statistic). In these graphs, when the bars from two groups' labels do not overlap along the abscissa, it means that a significant difference was found between them. While the LAR NLLS and BiSq NLLS are not significantly different from each other, they are significantly different from the other procedures' T1rho relaxation times and R^2 values. The circle represents the mean value in each group.

Overall, the results from this ANOVA test prove that T1rho relaxation parameter's value depends upon the algorithm used to perform the mono-exponential curve fitting. The curve-fitting algorithms also varied in their ability to fit the data, as demonstrated by their average R^2 values. The relaxation times for the LAR NLLS and BiSq NLLS were the smallest, and were significantly different from the other fits. These two fit methodologies also had significantly higher R^2 values; therefore, the LAR NLLS and BiSq NLLS fits characterized the true T1rho relaxation the best. Statistical similarity was found between the LAR NLLS and the BiSq NLLS, but the BiSq NLLS was approximately four times faster to compute than the LAR NLLS procedure, and thus became the preferred method of curve-fitting. The significantly worst fit to characterize T1rho relaxometry was the SqSI Weights, as indicated by its low value of average R^2. Interestingly, this yielded the highest average T1rho relaxation times.

This particular validation of curve-fitting algorithms demonstrated that the choice in the algorithm affects how well a given model describes the data, and how these descriptions could significantly mis-inform the analyst. Therefore, all future T1rho relaxation maps utilize the non-linear least squares fit with bisquare weights robustness measure (BiSq NLLS) curve-fitting algorithm. This validation also affirmed the first hypothesis in this chapter (Hypothesis A): The type of curve-fitting algorithm did affect the resulting T1rho relaxation times, as shown by the significantly different mean relaxation times (Figure 12).

3.5 Exploration of Spin-Lock Selection: A Permutations Study

Many studies have looked at the T1rho relaxation values for both normal and damaged cartilage *in vivo*, yet *specifically* what T1rho is measuring remains unknown. One source of confusion in multi-center determinations of relaxation properties is the variability in imaging parameters from study to study. Spin-lock (SL) time is an important T1rho imaging variable that directly affects the signal intensity of each image to be used in quantitative T1rho mapping.

Therefore, the goal of this exploration was to identify the effects of choosing various spin-lock times on the resulting T1rho relaxation properties, in both a 1.5T and a 3.0T scanner. More specifically, work was undertaken to determine whether different spin-lock combinations produce different relaxation times (Hypothesis B), whether increasing the number of spin-lock images captured causes the relaxation curve to be sampled more like a full data-capture (assuming full-capture is attainable with 12 spin-lock images, Hypothesis C), and whether the same spin-lock combinations can be used across magnetic fields to describe T1rho relaxation accurately (Hypothesis D). The answers to these questions will ultimately help determine what subset of spin-lock images are necessary and sufficient within a scanning session to properly ascertain absolute cartilage T1rho relaxation times.

These questions were addressed by a study of spin-lock permutations in both a normal subject and the cartilage-surrogate phantom. Ultimately, studies such as these will determin which SL parameters are most appropriate for consistently accurate analysis.

With Institutional Review Board approval and subject consent, one healthy 23 year-old female and the agarose-carrageenan gel phantom provided source data for this study. Same-day scans were performed to eliminate day-to-day variability. T1rho fast-spin echo acquisitions were performed on a 3.0T Siemens TIM Trio scanner and an Avanto 1.5T scanner. A quadrature knee coil was used. Twelve spin-lock (SL) times were chosen (SL=0.5,5,10,15,20, 25,30,40,50,60,70,80 ms) in a 2D oblique sagittal slice through the normal subject's LFC midline (see APPENDIX A: Image Sequence and Patient Information). The midline sagittal slice of the phantom was used for analysis, which provided five separate homogeneous signal regions.

T1rho relaxation maps of both the phantom and normal subject were created on a voxel-by-voxel basis. All combinations of SL times which would be used to create the maps were determined. Since a non-linear curve needs at least three points to start to accurately describe its behavior, all combinations which used three to twelve SL images were computed for the normal subject, and all combinations which used four to twelve SL images were made for the phantom images. To expedite calculation, a smaller region (approximately 25 x 50 voxels) centered on the interface between the superficial surfaces of the femoral and tibial cartilage was selected for analysis in the normal subject images (Figure 13). Smaller regions for the various phantom gels were also selected on the left side of the midline image (Figure 13). Results were reported in both a relaxation map and an image containing the R^2 measure for each voxel's fit. A manually segmented region of interest (ROI) was analyzed for each relaxation map. The full-data map (12

SLN) was used as the baseline image for permutation comparisons, since it *should* follow that more samples in a dataset can more accurately capture material behavior.

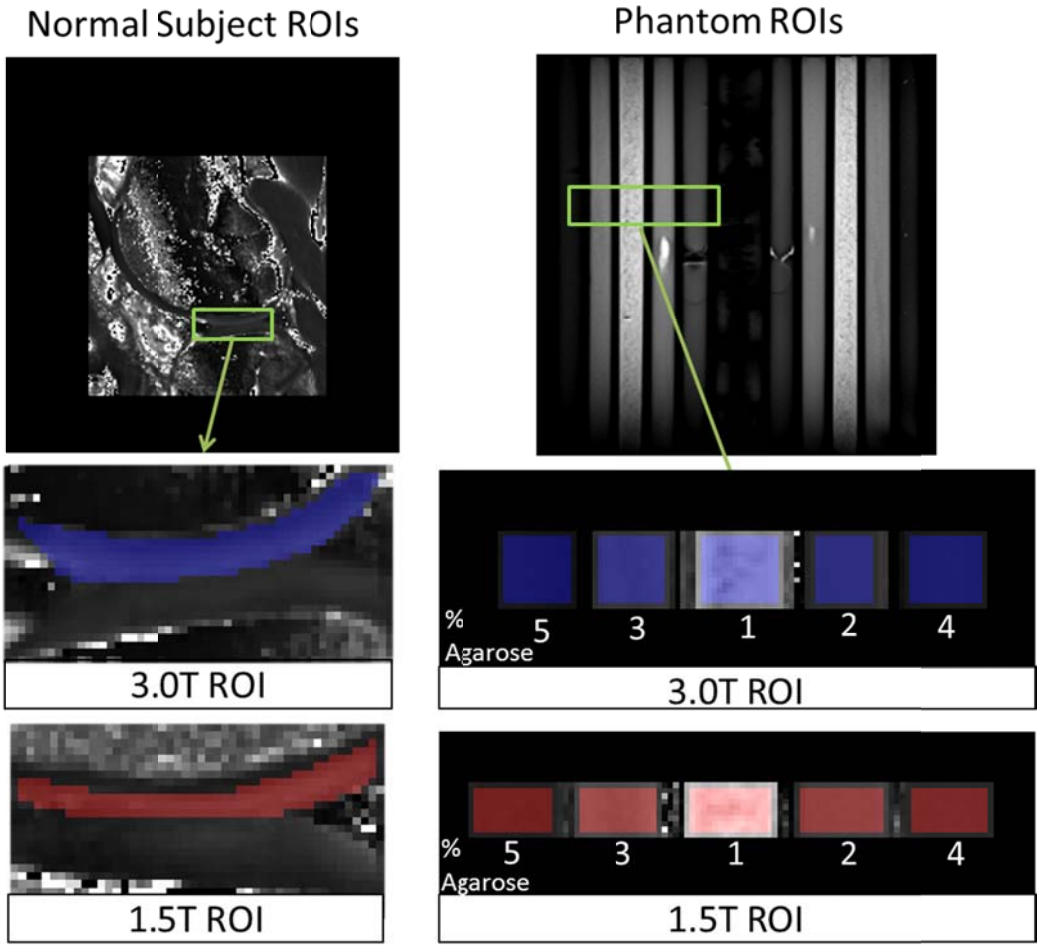

Figure 13. The full 12SL image maps (top) show the approximate location (green rectangle) of the entire smaller ROI regions in the normal subject (left, 4017 permutations) and the phantom (right, 3797 permutations). The two zoomed-in images at left show the femoral cartilage ROI analyzed for the 1.5T permutations (red highlighted) and the 3.0T permutations (blue highlighted). At right, the portions of the phantom gels which were analyzed are also highlighted.

A student's t-test was used to determine which spin-lock combinations were the closest to the full-data capture (12 SLN) ROI (95% confidence interval, p=0.05). Since the pval from the student t-test is the probability that the two compared datasets come from the same population with the same mean (with pval=1.0 being very similar datasets), if a combination has a pval close to 1.0, this demonstrates that the combination's mean relaxation time was very close to that of the full data-capture (12 SLN) image. A high probability value (p or pval) would indicate high similarity between mean T1rho relaxation times found in one map compared to the 12 SL map image, and a low pval would indicate low similarity. The highest pval-scoring SL combination for each number of SL images was also reported for the 1.5T and 3.0T image datasets.

Hypothesis B proved to be supported: different combinations of spin-lock times produced different mean relaxation times. The mean relaxation times from all *in vivo* combinations which had 6 spin-lock images are shown Figure 14 (900+ combinations). As can be seen, a range of values were obtained on both 1.5T and 3.0T, and there is quite a bit of variation with regards to the full-data capture map's mean relaxation time (12 SLN). This sort of variation in mean relaxation times, even when using the same number of spin-locks, was seen in the other permutations as well (3 to 11 spin-lock images used).

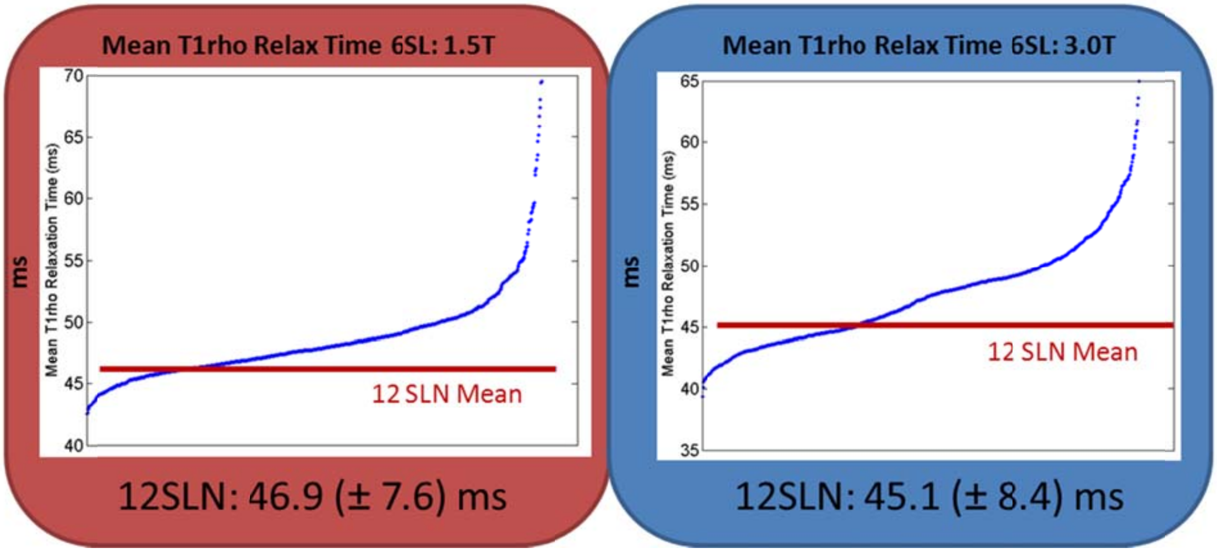

Figure 14. Mean relaxation times found for all permutations with 6 spin-lock images. As can be seen, the relaxation time varied considerably on both 1.5T and 3.0T systems from the 12 SLN map, thereby showing that spin-lock combination affects T1rho relaxation time.

The highest-scoring (closest pval to 1.0) pval spin-lock combinations for each number of spin-locks had normalized means close to 1.0 (with only 3 SLN pval<0.95 at 3.0T). As can be seen in Figure 14, however, a lot of the total combinations were not close to 1.0, and hence that is why the highest-scoring pval spin-lock combinations were examined closer to determine how many spin-lock images were needed. With respect to Hypothesis C, it was thought that as the number of spin-lock images captured increased, the value of the highest-scoring pval spin-lock combination (for a given number of images) would also increase. There were no apparent trends for the pval score based on the SLN in the normal subject data, but for the phantom data it appeared that pval range progressively converged with increased number of spin-locks (Figure B-3, Figure B-4). However, proximity to the full data capture image's mean relaxation could be achieved *independent* of the number of spin-lock images (meaning a pval very close to 1.0 was achieved at 3 SL, 4 SL, 5 SL, etc.). So while a pval was attainable (that was close to 1.0) in any number of spin-locks, only the overall probability that a higher pval score would be obtained increased with increasing the number of spin-lock images. This therefore refuted Hypothesis C.

There were no spin-lock combinations that were seen in both of the highest-scoring pval 1.5T and 3.0T results. This refuted Hypothesis D, in that the high-scoring pval spin-lock combinations were not the same on both systems. However, since it was shown that the combination of spin-lock times does affect the resulting T1rho relaxation values (Hypothesis B), the scores of the perturbations were re-examined for a combination that would yield the same spin-lock combination on both magnetic field strengths.

Optimal Trans-Magnetic (OTM) spin-lock times were determined for each number of spin-lock images captured, such that the same spin-locks could be used from one scanner to another to capture T1rho images (Table B-2). This was determined using the *in vivo* data to ensure that these spin-lock combinations would indeed be ideal for cartilage. Only permutations whose normalized means (combination's mean relaxation time divided by the full-data capture's mean relaxation time) were between 0.975-1.025 were considered, to eliminate some combinations that were completely different from the full-capture map. Next, the pval for each combination (within this range) was sorted and ranked. The permutations' pval rankings were compared such that the highest ranking combination on both B_0 systems would be the "best" OTM combination for that number of spin-locks captured.

Ultimately these permutations yielded several different options for capturing T1rho relaxation that would be similar to a full-data capture. This similarity to full data-capture was desired because twelve spin-lock images would be infeasible in a clinical setting, simply due to the limitations in time. Therefore, an acceptable approximation with fewer spin-lock times was desired. However, further analysis of the OTM combinations needed to be performed so that it could be known which one was the absolute best combination (as was the ultimate intent of Section 3.5). This analysis would therefore address how many spin-lock times were needed and which would still provide good capture of the relaxation curve within a clinical time-frame. A clinical-time frame of ten to fifteen minutes of additional scan time may be devoted to T1rho imaging within a typical knee scan, thereby dictating the number of spin-lock images (and thus times) that may be acquired. If one were to examine how many spin-lock times were acquirable within this time frame, it would equate to approximately 4 spin-lock times for three-dimensional (full joint) coverage, compared to 6-9 spin-lock times for one to two slices of 2D images.

The sum of squared error (SSE) was found between the highest-scoring combinations and the 12 SLN image for all voxels within the ROI. This would characterize how similar the "topography" of the ROI was to the 12 SLN image (or how close the actual error was). The smallest SSE were denoted (*) for each B_0 field by the number of spin-locks used in Table B-2 and Table B-3. The OTM combinations (with 9 or fewer SL) with the smallest SSE over the entire cartilage ROI were the 8 spin-lock OTM on 1.5T (followed by the 7 SL OTM), and the 9 spin-lock OTM on 3.0T (followed by the 8 spin-lock OTM, Table B-2). To give a better idea in an anatomically meaningful way, the normal subject's maps with OTM combinations and the full-data capture map were analyzed with Line Profile Analysis (Chapter 4), which would sample the T1rho relaxation time information from 0-50° in the posterior portion of the condyle at different cartilage zones. This is similar to the SSE analysis on the whole region of interest, except that only one meaningful line was examined in an area that would be used in future analysis. To simplify analysis, only the radial zone's line profile (1.0mm superficial to the bone-cartilage interface) was examined. For reasons unknown at this time, the SSE did not smoothly decrease as the number of spin-locks increased. As can be seen, the 8 spin-lock (1.5T data) and 7 spin-lock (3.0T) OTM had the smallest SSE (compared to the 12 spin-lock's profile in black, Figure 15). These combinations were the most similar to the full data-capture. In general, the 2D imaging combinations (6-9 SL) were more congruous to the full data capture map than the 3 or 4 SL (probably due to greater characterization with more spin-lock samples). It is curious that the 1.5T 8 SL OTM data was a better match than the 9 and 10 SL OTM; perhaps due to the inclusion of the 10ms SL information. Overall, the 8 spin-lock OTM (0.5, 5,10, 20, 30, 60, 70, 80 ms) combination is suggested as the spin-lock combination to use on both 1.5T and 3.0T magnetic field strengths, due to its similarity to full data capture (small SSE).

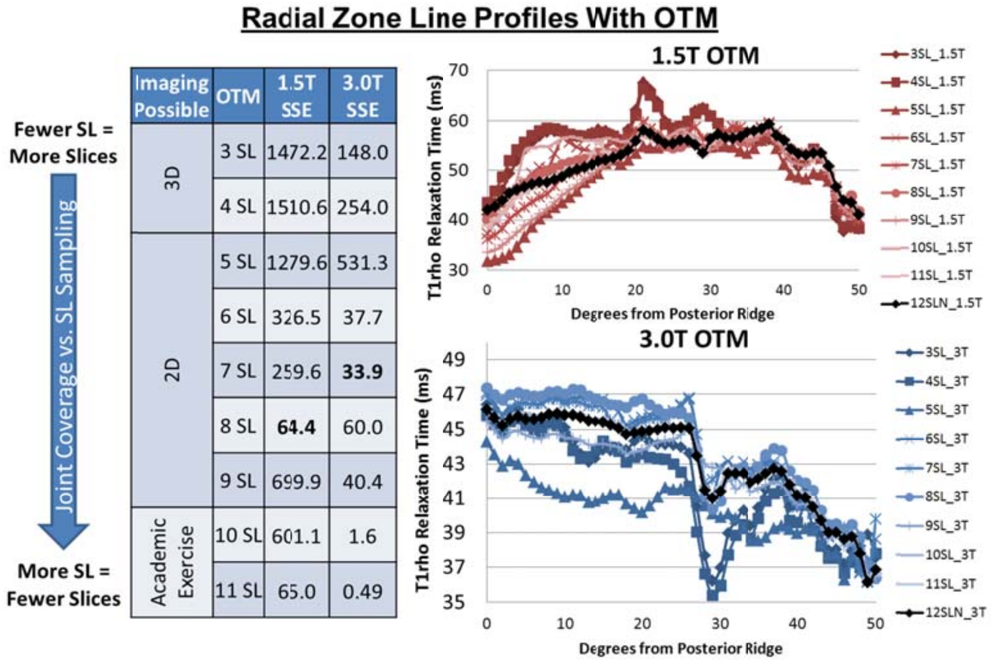

Imaging Possible	OTM	1.5T SSE	3.0T SSE
3D	3 SL	1472.2	148.0
	4 SL	1510.6	254.0
2D	5 SL	1279.6	531.3
	6 SL	326.5	37.7
	7 SL	259.6	**33.9**
	8 SL	**64.4**	60.0
	9 SL	699.9	40.4
Academic Exercise	10 SL	601.1	1.6
	11 SL	65.0	0.49

Figure 15. Radial zone line profiles (a line measurement made of the relaxation times through the posterior portion of the lateral femoral condyle, produced using Chapter 4's Line Profile Analysis) of the normal subject's cartilage using OTM combinations.

To the author’s knowledge, this is the first study of such a large number of spin-lock permutations for T1rho. This study has some limitations, such as the *in vivo* data coming from a small ROI within a single healthy subject. Only the results which used nine spin-lock times or less are clinically relevant (since a single two-dimensional slice acquisition may only be limited to six to nine SL images), and the other spin-lock combinations may prove to be simply an academic exercise. In spite of these limitations, it is necessary to understand where these relaxation values are derived to appropriately characterize cartilage in future studies. Currently, SL selections vary greatly in the literature [8, 28, 56, 59, 66]. Overall, this study highlights the importance of parameter choice to capture T1rho relaxation, which can be validated across centers through use of a phantom (like the one shown here).

3.6. Spin-Lock Images’ Spacing in Time: A Phantom Study

In this section, the effect of spacing in time between spin-lock images will be examined using the same 3.0T agarose-carrageenan phantom data that were collected in the previous section, to determine whether non-linear (exponential) spin-lock time spacing is a better sampling scheme than linear (equal intervals) spin-lock time spacing (Hypothesis E of this chapter). The results of this section will elucidate whether this should be a concern as well, when selecting spin-lock times for collecting T1rho patient data across centers.

Like other sections in this work, T2-mapping literature was used as a point of departure, since a similar T1rho experiment has not been reported to the author’s knowledge. Others have previously examined the sample spacing and the mathematics involved in T2-mapping for single and multi-exponential decay models [73, 74, 77]. One study, by Shrager et al., provided the basis for selection of the non-linearly spaced spin-lock times. Their study proposed a mathematical model for optimal T2 spin-echo spacing selection (i.e., the most essential spin-echo times to get the most characteristic signal information) which would work for single or double exponential models, given that an analyst had an initial estimation for the expected relaxation times boundaries, of the shortest and longest spin-echo times possible (based on signal-to-noise ratio being greater than 7), and the number of spin-echo images desired. Shrager et al. found a 30-80% improvement when using the non-linearly spaced spin-echoes, relative to the precision obtained using a standard, uniformly (linearly) spaced spin-echo experiment [77]. Therefore, it was hypothesized that perhaps a similar improvement would be seen when applying their mathematical model to create the exponential spacing for a T1rho experiment.

Since the sampling (either linear or non-linear spacing) would need to be sensitive to the full spectrum of expected cartilage relaxation values (which are derived from the shape of the mono-exponential decay curve), boundary values for this spectrum were defined (as per required by Shrager's model). The assumed expected boundaries for cartilage T1rho relaxation signal were between 5ms and 150ms. These conservative boundary values were chosen because anything below 5ms was expected to be bone, and anything above 150ms was expected to be fluid [66]. With regard to appropriate signal-to-noise ratio (SNR), the shortest spin-lock time which is achievable is 0.5ms, and the longest is 80ms, so these parameters were also used in the model. Lastly, the exponential spacing for four, six, and nine spin-lock times were found, since these number of images are perhaps achievable within a clinical scan timeframe. The resulting "optimal" exponential spin-lock spacings according to Shrager et al.'s model were 0.5, 3.03, 15.8, 80 ms for a four spin-lock (SL) capture, 0.5, 8.1, 18.6, 33, 52, 80 ms for a six SL capture, and 0.5, 6.6, 13.5, 21.3, 30.3, 40.4, 52, 65, 80 ms for a nine SL capture.

During the scanning of the cartilage-surrogate phantom (diagram in Figure 10), the spin-lock times of 0.5, 2.5, 5, 10, 15, 20, 25, 30, 35, 40, 45, 50, 55, 60, 65, 70, 75, 80 ms were captured (eighteen SL total). While not the primary purpose of these image captures, these SL times provided the opportunity for this study to use the same data to examine both linear and exponential spacing. However, these SL times were not always what the exponential model predicted, so approximations of the "optimal" SL times were made. The linearly spaced spin-lock times consisted of 0.5, 25, 50, 75 ms for the 4 SL map, 0.5, 15, 30, 45, 60, 75 ms for the 6 SL map, and 0.5, 10, 20, 30, 40, 50, 60, 70, 80 ms for the 9 SL map. Once approximated, the exponentially spaced spin-lock times consisted of 0.5, 2.5, 15, 80 ms for the 4 SL map, 0.5, 10, 20, 35, 50, 80 ms for the 6 SL map, and 0.5, 5, 15, 20, 30, 40, 50, 65, 80 ms for the 9 SL map. T1rho relaxation maps of these spin-lock times were made using the MRI_Relaxation_Map_Tool GUI. The corresponding R^2 values from the individual voxel fits were also recorded in a separate image.

Regions of interest (ROI) of the same size were selected in each of the five gel compartments within the resulting relaxation map and R^2 images of the phantom. The mean and standard deviation of the relaxation times are reported in Table B-4.

A student t-test was used to determine whether there was a significant difference ($p<0.01$) between the linearly- and exponentially-spaced relaxation times (individual gels) and R^2 values (whole data sets). The R^2 values would indicate how "well" the model (and its sampling scheme) fit the data, thereby giving the metric to determine which sampling scheme was superior.

Overall, both of these spacing methods produced relatively good fits, as indicated by the high mean R^2 values (n=5670 total voxels sampled, linear sampling $R^2=0.9931$, exponential sampling $R^2=0.9910$). Although none of the sampled data were considered a "poor" fit, the linear spacing was a better choice (as indicated by higher mean R^2 value, $p<<0.01$) than the exponentially spaced results, thereby refuting the fifth hypothesis of this chapter (Hypothesis E). The difference in spacing resulted in some significant differences in the T1rho relaxation maps times, with this occurring most often in the four spin-lock images.

In conclusion, it was proven that the spacing of the spin-lock image captures did affect the resulting T1rho relaxation times (since $p<0.05$ for some gels' relaxation times), and how well these relaxation times were derived (R^2 value from curve-fitting). At least for this study, non-linear (exponential) spacing did not provide an improvement in fitting accuracy over linear spacing. One limitation of this study was that the "true" optimal exponential spacings (as predicted by Shrager et al.'s model) were not attainable due to imaging time constraints. However, it was thought that the approximated spin-lock times would at least provide an initial examination of the effect of these spacing choices. Another point to consider is that this study was performed in the "ideal" phantom model, and different results may be seen *in vivo*. Future *in vivo* studies should be performed to further verify these results.

3.7 A T1rho Relaxometry Measurement Tool

Within each of the previous sections of this chapter, validation of each aspect necessary to make a relaxation map was demonstrated. The last component needed to incorporate each of these steps was a program which would be user-friendly and usable on different computer platforms. A custom Matlab-based graphical user interface (GUI) was created to perform such a task (Figure 16).

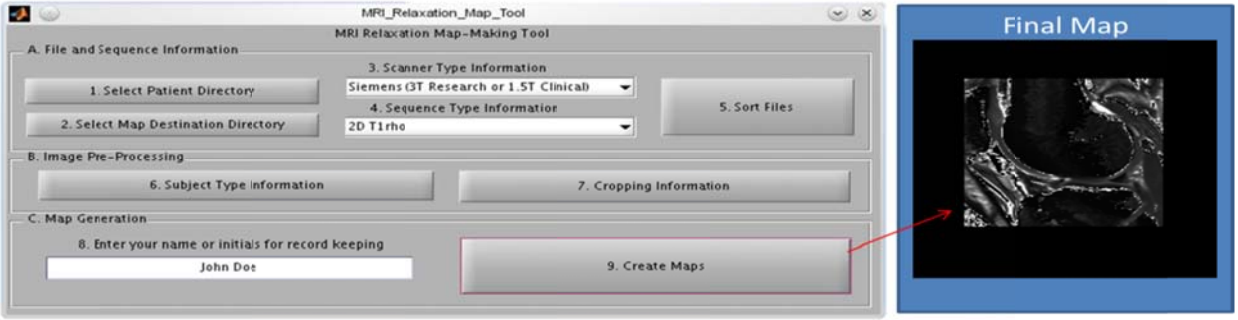

3. Scanner Type Information: Siemens (3T Research or 1.5T Clinical)
4. Sequence Type Information: 2D T1rho
8. Enter your name or initials for record keeping: John Doe

Figure 16. The MRI_Relaxation_Map_Tool GUI and an example relaxation map (right).

The MRI_Relaxation_Map_Tool GUI was created such that a MR technician or researcher could create T1rho maps for a patient. The GUI operates by interpreting the image information that is found within the header files of DICOM images, a typical image format for MRI and other medical imaging systems. This GUI was also easily modifiable, in that if a different quantitative imaging sequence was desired, a programmer could direct the program to the appropriate proprietary header file location of some key variables (e.g., the image's slice location). The GUI could then perform that new sequence's relaxometry procedure, since the basic concepts (Figure 9) of creating a relaxation map are similar for different quantitative sequences. Also, during GUI execution, the user has the option of using all or only some of the captured SL images during map creation. This flexibility facilitates future T1rho relaxometry experiments. The user also controls whether the mutual information registration technique is used (i.e. ACL-rupture patient) or not (i.e. phantom) by selecting the subject type. A cropping option is available to expedite the time it takes to create a relaxation map for a subregion of interest. Lastly, maps are automatically generated and placed in the directory of the user's choosing. With clearly labeled steps and instructions, the MRI_Relaxation_Map_Tool GUI is an easy-to-use tool for relaxation map construction.

3.8 Final Results and Conclusions About T1rho Relaxometry

In conclusion, this chapter discussed several validations of the methodologies incorporated into the MRI_Relaxation_Map_Tool GUI, the tool which is used in the rest of this work to create T1rho relaxation maps. The need for accuracy and understanding of T1rho relaxometry is pertinent in order to have confidence in the resulting T1rho relaxation parameters, which are later used to determine patient status (healthy or damaged cartilage) and perhaps outcome. Within this chapter, an automated registration technique was validated, such that appropriate corrections for patient movement could be made. If left uncorrected, movement would result in misleading T1rho relaxation values.

It was hypothesized that the number, combination, and spacing of the data points to be included, the model, and the type of fitting procedure used would ultimately affect what T1rho relaxation values are found from the curve fit. It was found that indeed the combination, spacing, model, and curve-fitting procedure did affect the overall relaxation measurement, but the number of spin-locks was not as critical as a factor, since a mean relaxation time that was similar to the 12 spin-lock map could be achieved with any number of spin-locks (as long as the combination was appropriate). This was demonstrated by the *in vivo* and phantom studies performed, with the 8 spin-lock Optimal Trans-Magnetic (OTM) combination being suggested as the spin-locks to use across clinics. Patient data collections for other chapters in this work were performed prior to these spin-lock combination observations, yet it is thought that as long as the same number and length of spin-lock times were used in each imaging session, that direct comparisons would still be possible due to the same signal information being acquired (i.e., comparing "apples-to-apples"). Overall, with an easy-to-use package, the MRI_Relaxation_Map_Tool GUI allows for appropriate T1rho relaxometry to be performed across platforms, thus aiding in T1rho's transition into a clinical setting.

CHAPTER 4: LINE PROFILE ANALYSIS- A TOOL TO ANALYZE T1RHO

4.1 Introduction

A clinically meaningful method to extract T1rho relaxation times from relaxometry maps is a crucial component to understand the biochemical and structural changes seen during osteoarthritic progression. Without such a methodology, correct interpretation of the T1rho relaxation times would be lacking. Ideally, the analysis methodology would be universally applicable across both healthy and arthritic subjects, and would provide a means to observe the same cartilage over time to allow tracking of disease progression. These ideal characteristics are not new to the quantitative imaging community.

Several groups have investigated different ways to provide meaning to quantify T1rho and T2 mapping in the tibio-femoral joint. Carballido-Gamio et al. investigated a methodology in five healthy subjects which incorporated a high-spatial resolution data set (morphometry, 0.312 x 0.312 x 1 mm voxel size) as an atlas for their 3D T1rho relaxation maps (0.546 x 0.546 x 3 mm) [83]. Since cartilage thinning is seen during the progression of osteoarthritis, they used the boney structures as a registration reference for their mono-exponential T1rho relaxation maps. The cartilage from the morphometric images was segmented at both the bone-cartilage interface (BCI) and the superficial interface using Bezier-splines, a segmentation technique used in other studies as well [27, 86, 87]. The morphometric data were then registered to the T1rho maps such that T1rho relaxation values were sampled at each voxel point within the BCI line profile. Normal vectors were then created from the BCI, and T1rho relaxation times were interpolated using a bicubic interpolating kernel at 21 equally-spaced depth-wise locations within the cartilage thickness. Further shape interpolation of the 3mm thick T1rho maps was performed to get isotropic voxel sizes, and texture analysis was performed with a gray-level co-occurrence matrix (GLCM) technique after the images were flattened [83]. While high-level image-processing techniques were applied to the T1rho data, the overall mean relaxation values were still reported with regards to the entire cartilage surface, or the values were merely presented graphically. This sort of reporting, while useful for general trends, may potentially be too generalized for localized cartilage damage within ACL-rupture patients. Attempting to characterize the cartilage further, other studies have divided the cartilage into subregions corresponding to deep and superficial cartilage zones [86] or into layer subdivisions of deep, middle, and superficial [87]. This may better describe the various cartilage signal properties, since different cartilage zones have different macromolecular structural configurations and functions. Yet, these studies still grouped cartilage into regions of interest (ROI). Again, while ROI analysis may be useful in some contexts (e.g., comparing image noise ratios in 1.5T to 3.0T), part of the spatial information is lost when combining T1rho relaxation times across broad areas of cartilage. Others have reported that straightforward three-dimensional Euclidean transformations to register image datasets may be all that is necessary to achieve voxel-based reproducibility within quantitative MRI, instead of investing in complex interpolation and re-slicing algorithms [88]. Knowing this, a direct technique may be achievable.

Line Profile Analysis, a simple-to-use objective methodology, is presented. After anatomical landmark identification, the femoral bone-cartilage interface (BCI) is detected using a Canny filter within the 20ms SL T1rho image. Patient-specific normalization creates a coordinate system which allows for sampling in 0.5mm increments (approximately voxel-sized) perpendicular to the BCI, thereby allowing for nominal zonal sampling of the T1rho relaxation map. Like Hohe et al., sampling at these three zonal layers (deep, radial, transitional) will allow for more specific cartilage changes to be documented compared to full-thickness ROI average comparisons [87]. To provide a means to capture localized cartilage damage, T1rho relaxation times are also sampled in 1° increments along the BCI at each zonal layer from the sulcus' posterior ridge (anatomic landmark) posteriorly until a 90° angle has been reached. With this tool, T1rho relaxation information can be characterized in a clinically meaningful way.

4.2 Line Profile Analysis Methodology and Validation

4.2.1 Initial Image Pre-Processing and Edge Detection

The images used to validate the Line Profile Analysis consisted of T1rho data (SL=5,10,20,40,60,80ms) collected three times within a single week from five healthy subjects without PTOA or known knee injury (see APPENDIX A: Image Sequence and Patient Information). During each session, three oblique-sagittal slices (aligned with the midline of the lateral femoral condyle rather than the body's sagittal plane) were taken of the knee: through the trochlea, the midline of the lateral femoral condyle (LFC), and a slice 6mm lateral to the LFC's midline slice. The latter will be referred to as the lateral slice, and the midline of the LFC will be referred to as the midline slice for the remainder of this section. While most T1rho data analysis was performed for the majority of this work on both healthy and injured subjects' midline slices, some of the Line Profile Analysis' methodology validation was also performed using these lateral slices, thereby demonstrating that future application to these lateral slices would be valid.

Matlab R2009a (The MathWorks, Inc, Natick MA) was the programming environment utilized for developing this method. After the user selected the appropriate folder locations for the current patient's data and the desired output folder location within the file system, the line profile generation program began by using the SL=20ms sagittal slice as the basis for coordinate system definition. This SL image was chosen since it has been the first image captured in all patient protocols, and it was also the "static" image within the automated similarity-metric driven registration algorithm during relaxation map creation (see 3.2 Spin-Lock Images' Registration and Validation). The 20ms image also has high signal-to-noise ratio (SNR), thereby aiding user identification of different tissues in some subsequent analysis steps. If this Line Profile Analysis program is used with other MRI sequences, similar reasoning (i.e. high SNR) should be applied for the selection of this coordinate-determining image.

A Canny filter was applied to the original 20ms SL image to highlight the edges found within the knee (Figure 17). The Canny filter is a commonly used multidirectional image processing filter, where edges are detected by convolving a two-dimensional Gaussian filter and then its derivative with the image. First, the image is smoothed by the Gaussian filter and then the derivatives are applied in both the x and y directions of the image. Local maxima of the image's gradient are then found, by setting both a high and low threshold value to detect strong and weak edges (automatically determined thresholds based on image brightness and contrast). The maxima are found in both the x and y directions and along the diagonal, thereby detecting edges in several different directions. If a weak edge is detected (i.e. low contrast), it will only be included in the output if it is connected to a strong edge, which is known as hysteresis [89].

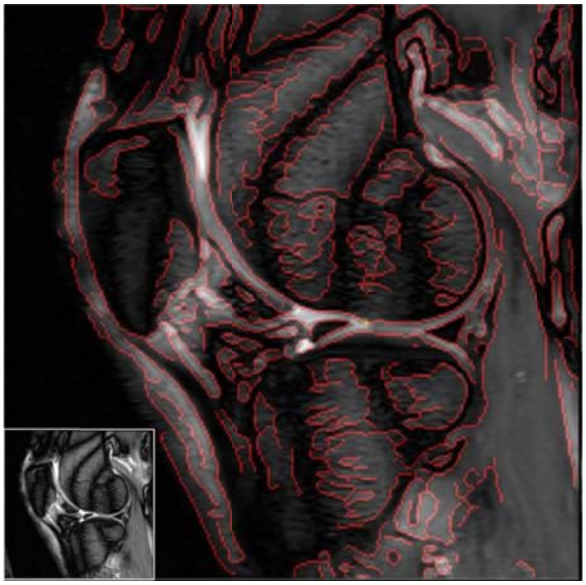

Figure 17. The original 20ms SL image (lower left inset) of the lateral femoral condyle midline, and the results of applying a Canny edge-detection filter (red edges). From this image, a user would select the appropriate edge which is the bone-cartilage interface (BCI) of the femur from the other Canny-detected edges.

Another advantage of the Canny method is its ability to find the same edges, no matter the direction of the local gradient. In other words, the Canny filter can find the same edge locations in images which have different contrasts between tissues, whereas other filters may not be able to detect exactly the same edge locations for both images. An illustration of this property can be seen in Figure 18. A typical 20ms T1rho image of a normal subject was negated ("negative" image) such that it would have exactly the opposite gradient direction of its original image. Then, a Laplacian of a Gaussian (LoG filter), which detects edges by finding the "zero-crossings" of the gradient after a Gaussian blurring filter has been applied [81], and the Canny filter were applied to both images. If a filter found the same edge locations in both images, then it could be considered direction-independent of the gradient, since no other transformations (i.e. translation) were made to these images. However, as can be seen within the highlighted green region of interest, the LoG filter reported different edge locations for the original and "negative" image. Yet, the Canny filter was able to detect exactly the same edge in each image. This property of the Canny filter is advantageous for future Line Profile Analysis studies between MRI imaging sequences of dissimilar contrasts, such as T1rho and T2.

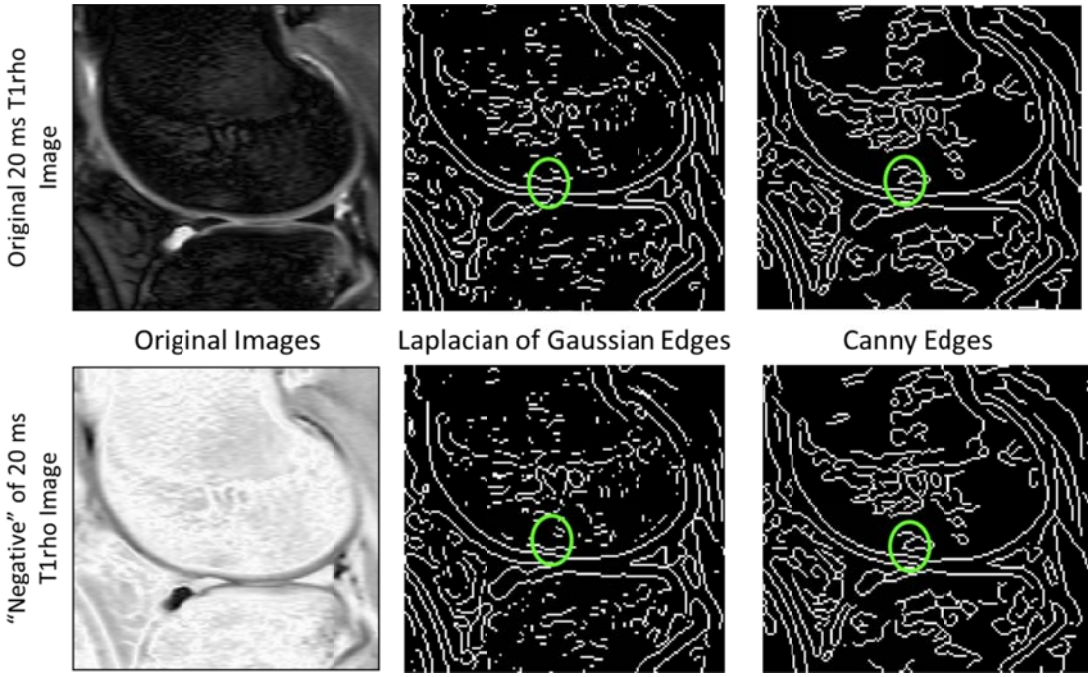

Figure 18. Demonstration that the Canny filter can detect the same edges, independent of local gradient direction. The negative and original 20ms T1rho images had a Laplacian of Gaussian (LoG) and a Canny filter applied to them. The detected edges are shown in white. Within the green circled area, it is easy to see that the location of these edges are different between the two LoG images, but not the two Canny images.

4.2.2 Determination of Anatomic Landmarks

Once all edges had been identified from the Canny filter, the user identified the sulcus area (dimple between the anterior patellofemoral and posterior weight-bearing surfaces of the lateral femoral condyle) by selecting two boundary points demarcating the region; one point anteriorly and one posteriorly. The program then located the closest Canny-detected BCI voxel to each of the user-selected anterior and posterior cutoff points, in order to correct for any slight user misplacement of these points.

A 3x3 sliding-logic matrix (SLM) was used to capture and record the BCI voxels. This logical matrix would only allow those pixels which were previously identified by the Canny filter to be considered for addition to the BCI. To demonstrate how the SLM worked, consider the following example. A portion of the BCI has already been detected, and the center (point E) of the 3x3 neighborhood matrix is the current endpoint of the recorded line (Figure 19). Suppose that this SLM was recording points along the BCI by moving from the anterior to the posterior of the condyle. In the example then, the SLM would not consider any points which would have been previously under consideration (points A, B, C), and would only consider those which may provide new information (points D,F,G,H,I), and then within this subset the SLM would only consider those points which were detected by the Canny (point H). If only one new point was detected, such as point H, then this single point would be added to the recorded BCI line, and would then become the new end of the line. This process was repeated until some pre-determined ending point had been reached (i.e. the posterior cutoff point for the sulcus region). Some provisions were made to allow some user intervention in the case that this logic failed, such as when two pixels were detected (crossing lines) or if the end of the BCI line was detected prematurely to the pre-determined ending point.

After finding the voxels on the Canny line closest to the user-selected anterior and posterior sulcus points, the program used the SLM technique to record the remaining Canny detected bone-cartilage interface voxels. Three landmark points were then found from analyzing the physical geometry of this line: the anterior ridge point, sulcus midpoint, and posterior ridge point. These three landmarks, especially the posterior ridge point, would be used subsequently to define the patient-specific coordinate system.

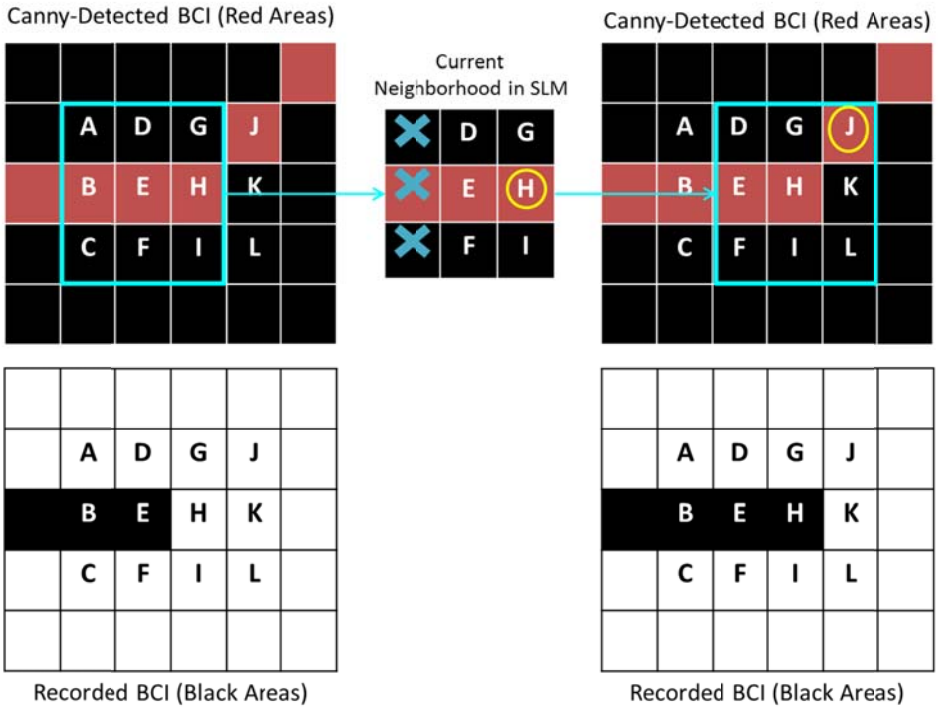

Figure 19. A Sliding Logic Matrix (SLM) was used to automatically detect and record the bone-cartilage interface (BCI) from the Canny-detected edges (shown in red, top). The 3x3 SLM (blue rectangular outline, top) moves anterior to posterior in this example, and therefore does not consider the voxels marked A, B, or C (x's in current neighborhood) since these were previously evaluated. The center voxel E, is the current end of the recorded BCI (last black area, lower left). As the SLM evaluates voxels D,F,G,H,I (middle), the only voxel which was a Canny-detected edge was H (circled). Voxel H is added to the end of the recorded BCI (lower right), and the SLM now uses voxel H as its center (upper right). Following this same logic, voxel J (circled upper right) would be the next point to be added to the recorded BCI.

Landmark determination began by creating a smooth curve from the voxelated BCI line found between the two boundary points. This was to simplify the overall geometry, such that definite peaks (i.e. the sulcus midpoint) would be readily identifiable. First, any geometric redundancies within a continuous area (i.e. anything but the midpoint of a flat region) would be removed from the group of points which would be fit with a piecewise-cubic Hermite interpolating polynomial (pchip) line fit. These were eliminated since it was presumed that these very long flat regions were introduced by the Canny edge (small curvature variations likely found in the infinitely small bone-cartilage interface in physical space, but due to sampling 0.55 mm voxels, some of these slight variations are likely lost in the discretization of the signal in imaging space). Once the pchip line had been fit to these remaining points, the local maxima and minima would be determined in Matlab. Ideally, the global minima would be the posterior ridge, the global maxima would be the sulcus midpoint, and then the next local minima anterior to the sulcus midpoint would be the anterior ridge point. A typical example is shown in Figure 20. However, due to morphological irregularity from knee to knee, knees with less pronounced sulcus regions had more linear pchip curves, and only the posterior ridge point's peak was clearly distinguishable. In the end, the user retained the final selection of the landmark points from the reduced set of "geometrically descriptive" points identified by the pchip fit. Anterior to posterior order was preserved, and subjectivity between users was reduced with objectively determined landmarks across imaging sessions.

To validate this procedure, two tests were implemented to determine the repeatability and reliability of anatomical landmark location. Inter-user variability consisted of three users (engineering graduate students) finding and defining the landmark points for three different knees. These images were from Normal 3's first scan of the lateral slice, Normal 4's last scan for the midline slice, and Normal 5's first scan of the lateral slice. The different images provided different knee geometries, and therefore tested whether the program would also work for various subjects. After being briefly familiarized with the general terms used in the program and the physical geometry of the knee, each user was asked to pick the anterior and posterior points bounding the sulcus region. The resulting anterior ridge point, sulcus midpoint, and posterior ridge point were recorded and compared for each of the four trials for each image (twelve trials total for each image).

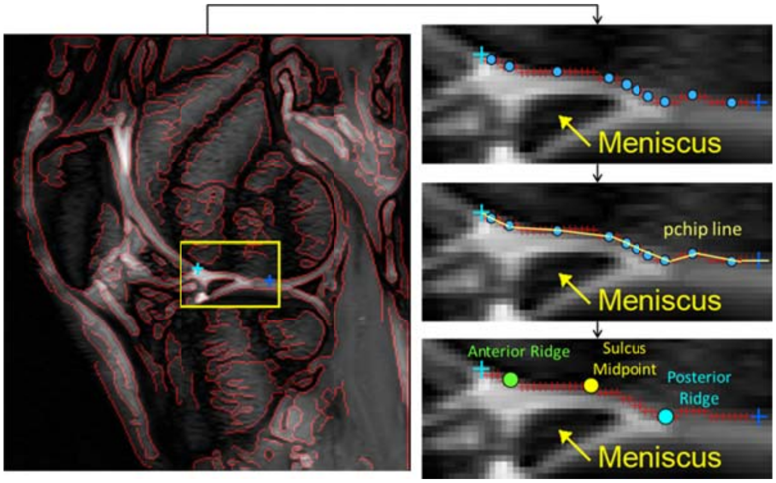

Figure 20. Landmark determination begins when the user selects an anterior (light blue) and posterior (dark blue) boundary to the sulcus area in the Canny-image (left). After the SLM is applied to record the sulcus area's BCI (red cross-hairs in zoomed-in right images), geometric redundancies (flat areas due to Canny voxelation) are eliminated (blue circles, top right). A line is fit to these points (yellow line, middle-right), and the maxima and minima of the line determine the position of the anterior ridge (green), sulcus midpoint (yellow), and posterior ridge (cyan, lower right image).

The number of different voxels for the user-selected anterior cutoff boundary points ranged from seven to ten, and the number of voxels for the user-selected posterior boundary cutoff points ranged from four to six, between the three knees (Table C-1). The program was able to reduce the number of posterior ridge points generated to just one or two locations for each knee. The mean distance between the program-determined posterior ridge points was less than the mean distance between the user-selected posterior cutoff points. The maximum distance out of the three knees between generated posterior ridge points was 2.25 mm, which occured for Normal 3. For a physical perspective on this variance in location, this means that the sampling would roughly vary ±2.5° along the condyle once the polar coordinate system was introduced (as calculated for this subject, small compared to overall 90° being sampled for each layer; this will be discussed in Section 4.2.4). Therefore tracking changes within a patient's cartilage over time could be slightly affected by this, but not as much as if the landmark was not computer-generated. The reduction in the number of unique landmark locations and the distance between those locations is evidence that the program was able to reduce the subjectivity between users' selections, and therefore provide a more consistent, objective anatomic landmark point (the posterior ridge).

To verify that this posterior ridge landmark's location consistency was not dependent upon the user selected posterior boundary cutoff point, a formal validation test was performed to demonstrate objective correction of inaccuracy in point selection. In this test, the user selected the original anterior and posterior boundaries of the sulcus region. In a grid-like manner, the initial selection of the posterior boundary's (x,y) coordinates was changed in single voxel increments (Figure 21). This yielded 49 different locations where a user could have potentially chosen a posterior boundary point within an area of approximately 10.8 mm^2 (the anterior boundary point was kept the same for all cases of this particular test, since its location- as long as it is anterior of the sulcus dimple- would not affect the resulting location of the posterior ridge). For each of the 49 cases, the coordinates of the program generated landmark points were recorded.

The preponderance of the 49 trials (34 trials, 69.4%) resulted in the same posterior ridge point being found. Thirteen trials found a point 1.5mm closer to the sulcus, and two trials located the posterior ridge 1 mm farther down the sulcus wall. The maximum distance between the posterior cutoff points was 4.64mm; however the maximum distance found between the predominant generated posterior ridge (34 trials) point and the relative outlier (2 trials) posterior ridge was 2.45 mm. These results demonstrated the overall number of locations (3) for the posterior ridge was reduced by the program compared to the initial number of posterior cutoff locations (49). The maximum distance between the generated posterior ridge points was also approximately half of the maximum distance between user-selected posterior cutoffs, thereby removing some of the subjectivity between landmarks. Also since most of the trials resulted in a single point, it demonstrated that the program was insensitive to user point selection of the posterior cutoff.

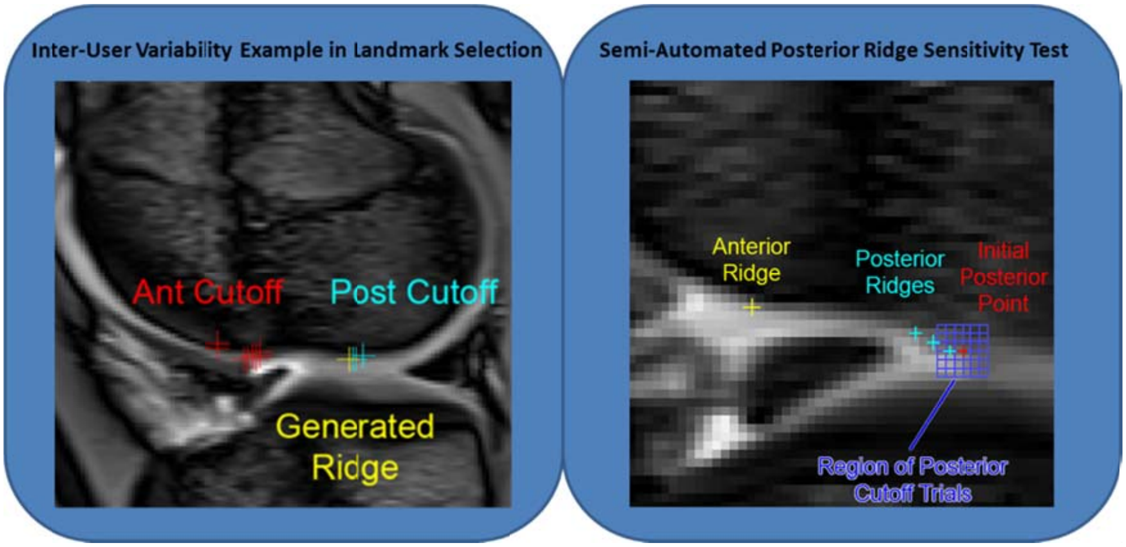
Inter-User Variability Example in Landmark Selection

Semi-Automated Posterior Ridge Sensitivity Test

Figure 21. Validation of the anatomical landmarks' objectivity. An example image (left) of one of the three normal subject's knees which indicate the location of the three users' multiple selections for the anterior cutoff (red) and posterior cutoffs (cyan) demarcating the sulcus region, as compared to the single generated posterior ridge (yellow). In the second test (right), the anterior cutoff point (yellow) remained the same throughout all 49 trials whereas the posterior cutoff was moved in a 7x7 area (blue) around an initial posterior point (red). Three locations for the posterior ridge (cyan) were generated from the 49 trials.

Overall, these validation tests demonstrated that the posterior ridge point was more objective (meaning, less variable in its location) than the user-selected locations within the sulcus region of the femur. This (program-derived) posterior ridge point was therefore used as the Line Profile Analysis' coordinate system origin.

4.2.3 Bone-Cartilage Interface Detection

Once the landmark points were determined, a line-growing protocol utilizing the sliding-logic matrix (SLM) technique was followed in both the anterior and posterior portion of the femoral condyle. While the focus of this work deals primarily with the posterior portion of the femoral condyle, the methodology was similarly followed in the anterior portion of the knee. The Canny detected bone-cartilage interface (BCI) was followed from the posterior ridge point to a pre-set angle of 100° anteriorly and posteriorly. Then, the user was shown the detected pixels with the option to select both endpoints, in case the pre-determined 100° angle was beyond the cartilage extent. All points which were superior to this user-indicated last point were excluded from further analysis. Ellipses were fit (to the centroid x-y coordinates of the Canny-detected edge) using a least-squares criterion to the anterior (from the anterior ridge to the last detected anterior point) and posterior sectors (from the posterior ridge to the last detected posterior point), and the initial locations were reported in 0.5mm increments posteriorly from the posterior ridge (for the posterior cartilage regions). Ellipse fits have been previously used and validated as a simple way to characterize sagittal views of the femoral condyles [90]. This was performed in order to smooth any stair-step voxelation from the Canny filter. The irregular sulcus region's points were omitted from ellipse fits so as to get a more accurate fit of the anterior and posterior condyles. The same interpolation and smoothing routine (Matlab pchip utility) used in landmark point generation was also used to determine the bone-cartilage interface for the sulcus region.

To validate that the same bone-cartilage interface could be detected within the same subject from different scanning sessions, the actual shape of these edges were registered across the three scanning sessions for each normal subject's midline and lateral slices. The line profiles for the latter two sessions were analytically rotated and translated to match up with the BCI line found from the first scanning session's images. This was done by registering the posterior ridge point (as the origin) and the point which was 30mm posterior, and then performing a rigid affine transformation to the remaining points of the curve. Since the 0.5mm spacing remained the same between points on all three curves, the locations of paired points could be directly compared. This validation assumed that the posterior ridge point was indeed at exactly the same location over the course of the three days. The various curves' locations were plotted on the common coordinate system from the first scanning session, and the distances between corresponding points were analyzed (Figure 22).

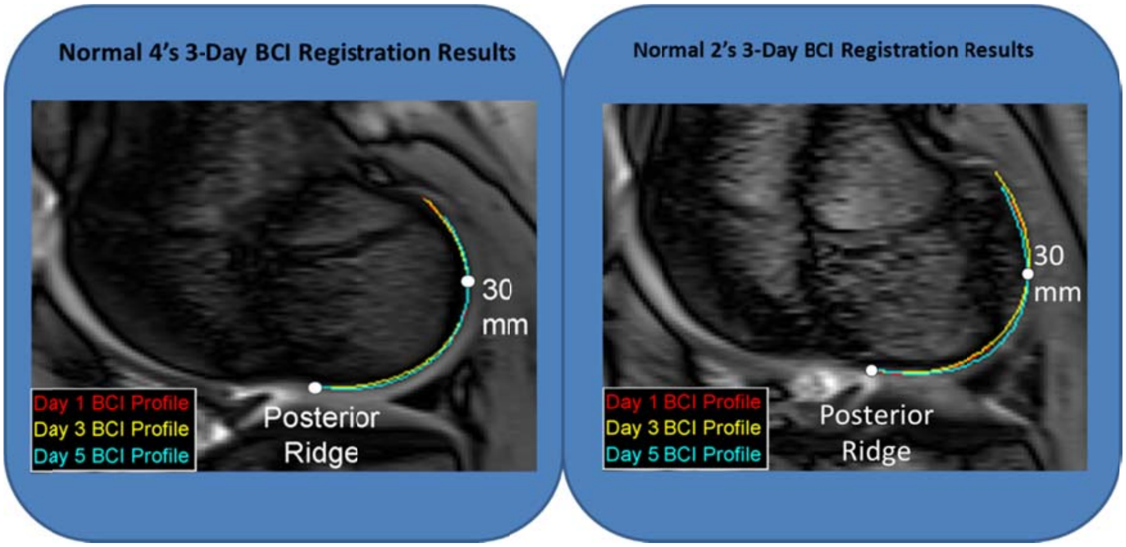

Figure 22. A demonstration of the BCI registration across the three days for Normal 4's scans (left) and Normal 2's scans (right). It is clear that the Day 5 BCI profile is not the same shape as the other two scans for Normal 2, and thus may indicate poor slice alignment, considering the other BCI profiles shown here are fairly similar.

Analytical registration of the three posterior bone-cartilage line profiles for each subject yielded the average distance results (Table C-2). The minimum distance between corresponding points for all images was 0.0mm. The maximum distance was 2.134 mm (Normal 5, midline slice). The majority of the average distances between curves were approximately 1 pixel's width (0.5mm). It is understood that this registration cannot directly test the repeatability of the BCI shape, since there is a confounding factor of imprecision between two-dimensional slice locations from different imaging sessions (which may affect the overall shape of the bone-cartilage interface and resulting location of the posterior ridge). However, this demonstrates the practicality of determining approximately the same BCI from session to session, even with two-dimensional imaging. Ideally, three-dimensional imaging would allow precise location of these slices. However, this was not a possibility with the data gathered in this study. Therefore, it is good to know that the bone-cartilage interface can be determined, measured, and used as a reference from one imaging session to another with relative consistency even with 2D data.

4.2.4 An Anatomic Radius for a Patient-Specific Coordinate System

To make comparisons across different subjects, anthropometric scaling normalizes final coordinate system definition. If all subjects had the same sized knees, then using the previously described 0.5mm increments along the bone-cartilage interface (BCI) would be satisfactory. However, these increments may result in very different portions of the cartilage being sampled if one is comparing a large femoral condyle to a small femoral condyle.

A patient-specific, cylindrical measurement system may be defined, assuming that the posterior femoral condyle is elliptical. By using a central reference point, the femoral cartilage's T1rho relaxation values can be measured in degrees of an arc made from another reference point that lays upon the circumference, such as the posterior ridge.

The patient-specific radius and central reference point still needed definition. The central reference point's anterior-posterior position was placed at the same anterior-posterior position as the objectively located posterior ridge point in each knee. Proximal placement was extracted from other femoral geometric information, and the most posterior point along the BCI was determined. Since this coordinate system is for sampling the cartilage in the posterior portion of the femoral condyle, the BCI provided a curve that would indicate the needed geometric size. If one considers the posterior ridge as the beginning of this continuous line, the furthest point along this curve (in the x-direction) would give the relative size of the condyle (with respect to the posterior ridge). Distances between the perpendicular intersection of the proximal-distal axis (running through the posterior ridge) and anterior-posterior axis (running through the most posterior point) provided the source for the averaged condyle-specific radius (Figure 23).

The anthropometric radius defined the central reference point at approximately the femoral condyle's center of rotation. It was verified that a simple circular fit (without the anthropometric radius) to the BCI was inappropriate for all knees, since some were not as round as others. This could lead to a large circle approximation, and would cause the central reference point to be too proximal to be considered the approximate center of rotation (Figure C-1).

The final coordinate system definition was achieved once the condyle-specific radius, posterior ridge point, and central reference point had been derived. The posterior ridge was used as the origin (0°), as T1rho relaxation times were sampled in single degree increments along the BCI until 90° had been reached (Figure 23). While some groups have previously defined the weight-bearing portion to be limited to 30° posterior of the femur's longitudinal axis [86, 91], it was determined that a full 90° investigation may be more appropriate to characterize cartilage injuries which may occur over a larger range of flexion (i.e. range of motion is approximately 82.5-119° flexion during sit-to-stand movement across age-groups, [92]). Since this coordinate system accounts for knee size prior to normalization, it allows for common cartilage areas to be sampled between imaging sessions. T1rho relaxation changes can be tracked over time, as well as between subjects to make broader, population-based conclusions about T1rho imaging within femoral cartilage using this anthropometric normalization.

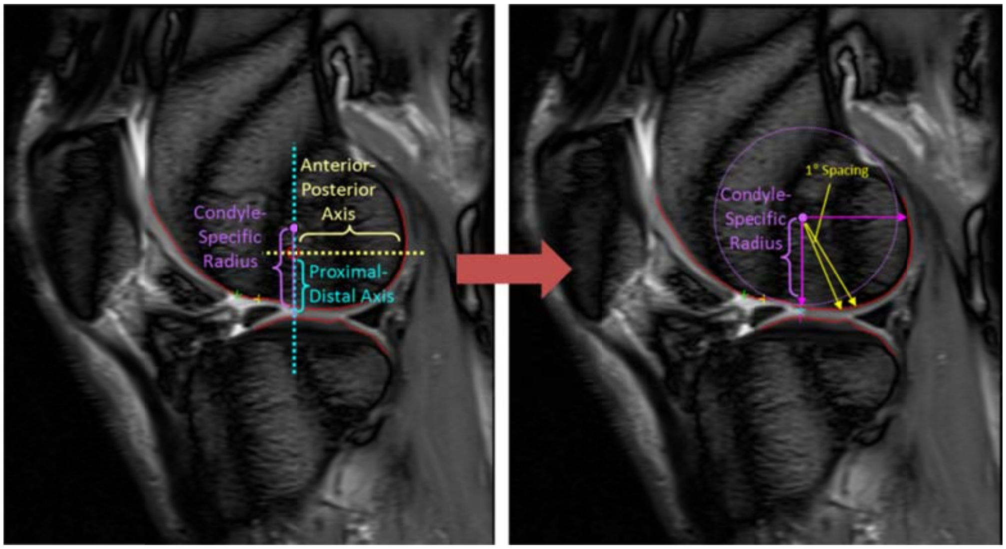

Figure 23. Derivation of the patient-specific coordinate system. The central reference point (purple dot) were determined to be proximal to the posterior ridge by a distance (condyle-specific radius) that was an average between the anterior-posterior axis (yellow) and the proximal-distal axis (teal). Once this central reference point was determined (right), locations along the BCI (red line) were sampled in 1° increments (yellow arrows) between 0-90° (pink arrows) from the posterior ridge. The purple circle (right) shows the approximate size of the condyle-specific radius.

4.2.5 Creation of Line Profiles

Once the patient-specific coordinate system had been defined, line profiles could be created. The T1rho map of the posterior portion of the lateral femoral condyle was sampled in 0.5 mm increments perpendicular from the detected bone-cartilage interface (BCI) to create layers nominally at the deep (0.5mm layer), radial (1.0mm layer), and transitional (1.5mm layer) zones of cartilage. The BCI T1rho relaxation times were not reported, due to partial volume effects caused by the subchondral bone. These three layers, comprising the line profiles, were sampled in single degree increments from the posterior ridge as well. A bilinear interpolation kernel was used to determine the continuum T1rho relaxation times within the image, since voxel intensities are stored in discrete column-row format (Figure 24, [81]).

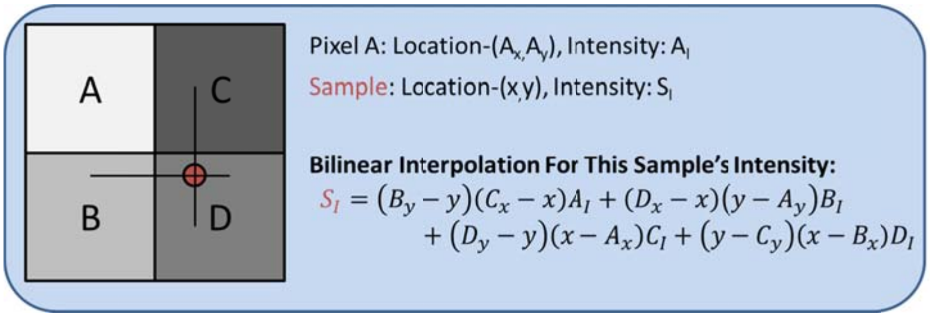

$$S_I = (B_y - y)(C_x - x)A_I + (D_x - x)(y - A_y)B_I + (D_y - y)(x - A_x)C_I + (y - C_y)(x - B_x)D_I$$

Figure 24. A simple bilinear interpolation example for the sample to be taken at location (x, y) (red dot). Using other voxels' coordinates (i.e. A_x,A_y for voxel A) and their signal intensities (i.e. A_I), an interpolated signal intensity at that sample location was found(S_I). This interpolation kernel was used to extract T1rho relaxation times.

Lastly, an example of how these relaxation values are reported can be seen in Figure 25 from Normal 4's second scan, as well as the patient-specific coordinate system used as a reference. With such a tool, zonal-specific and location-specific cartilage T1rho relaxation values may be viewed and interpreted.

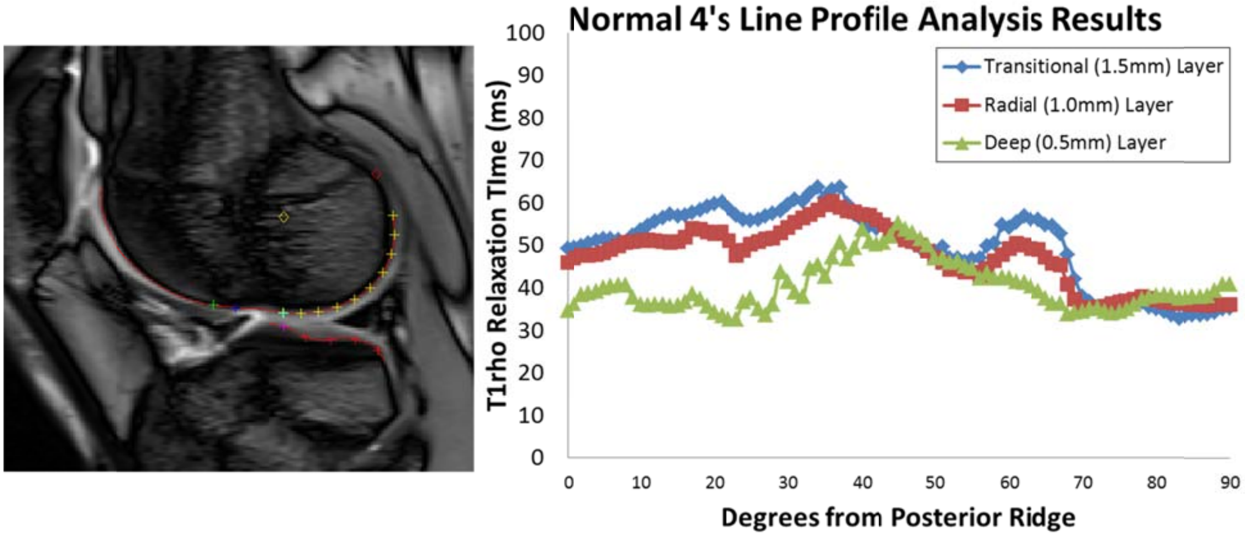

Figure 25. The final patient-specific coordinate system produced for Normal 4’s second scan (left), and the T1rho relaxation times found at each of the three layers (right) sampled from 0° (cyan cross, left image) to 90° (most proximal yellow-cross) from the posterior ridge.

4.3 Discussion and Conclusions About Line Profile Analysis

Line Profile Analysis has been shown to be an objective method in which to sample T1rho relaxation times from femoral articular cartilage. The Canny filter allows for consistent bone-cartilage interface detection, since automation provides edge detection independent of user error. The posterior ridge of the sulcus area in the lateral femoral condyle has been shown to be an identifiable and reliable landmark point across different patient geometries. The patient-specific radius allows for normalization across subjects, and T1rho values that are reported may be used to more specifically identify cartilage abnormalities than region-of-interest averaging techniques. In addition to a fast processing time (approximately two to five minutes), the analysis utilizes a graphical-user interface (GUI) and exports results to Excel.

While this technique has strengths in its objectivity and ease of use, there are a few limitations. Since only the bone-cartilage interface is detected with the Canny filter, only one surface of the cartilage has been found. The cartilage surface boundary cannot be differentiated from other tissue types using this technique, which may result in relaxation times of different tissues and fluid being reported in the more superficial cartilage line profiles. While future implementations of this technique may utilize other edge detections for the surface, it would be advised to not normalize cartilage layers with respect to the cartilage thickness. Such zonal normalization could be appropriate for use in a normal, healthy population, but since cartilage degenerates from the surface down to the bone-cartilage interface in the progression of OA, normalization would be inaccurate for tracking the same locations over time in a patient population. However, if the same depth-wise increment is used over time (i.e. 0.5mm increments) for zonal definitions, the same cartilage areas can be tracked until that tissue has fully degraded. If such a surface detection technique were incorporated, it would be possible to ensure that Line Profile Analysis would occur only within the cartilage tissue, and that it would still be measured in the same locations over time, even with cartilage thinning.

One thing to note is that the Canny filter, like many other basic imaging filters (i.e. LoG), reports the edge locations based on the voxel (x,y) coordinates. These coordinates are defined at the centroid of the voxel. This discretization of the signal (and its demarcation) does not consider that cartilage is a continuum. This may have implications with regards to partial volume effects being sampled near the bone-cartilage interface. This is why the bone-cartilage interfaces' line profile is not reported at all, but this central voxel coordinate location may also slightly affect the deep layers' calculated relaxation times as well, depending upon the final location of the edge (after ellipse fitting).

The worst-case scenario for the effect on the deep layer can be described by the simplified scenario seen in Figure 26. If the physical BCI (gold) is located as such with respect to the voxels' sampling (squares), the Canny may discretize the edge to the closest voxel coordinates, which in this case belongs to the bone (red x's, left panel in Figure 26). This would then be reported as the detected BCI. Then the other line profiles would be sampled in 0.5mm increments from the detected BCI, and the relaxation times would be derived using the bilinear interpolation kernel. In this scenario, the bone (0 ms relaxation time) would affect the deep layer's relaxation times, resulting in an artificial 13.2% loss in relaxation time for the deep zone (if we consider cartilage relaxation to be 40 ms, which is reasonable given some of the measured times in Chapter 5). However, this is the absolute worst effect that this discretization and subsequent interpolation would have. Another issue with this interpolation is that sub-voxel magnitude errors are introduced if different physical depths in the cartilage coincide with 0.5, 1.0, and 1.5 mm levels (i.e., some patient variability in physical cartilage stratification). However, interpolation is a common way in image processing for finding a more continuous signal from the image data, especially in MRI where clinical voxel size can be large compared to other imaging modalities (i.e. CT). One group used a bicubic interpolating kernel to interpolate T1rho relaxation signal from a discrete segmentation using 21 equally spaced points over cartilage thickness (4-5 voxels, same resolution as used in this work of 0.55 x 0.55 x 3mm) [83]. Given this level of interpolation in others' work, it seemed that a small interpolation like the one here would impart fewer errors to the actual measured signal.

The dominant assumption made during this two-dimensional Line Profile Analysis is that the MRI scan will be taken in the same location every scan session for a particular patient. This assumption makes it possible to track a patient's progression in the same slice sample across imaging sessions, yet it is not entirely valid. Like any other two-dimensional medical image, some geometric information is inherently lost when the whole joint is not scanned. Therefore, the exact slice location for T1rho image analysis is entirely dependent upon the MRI technician's judgment while selecting the midline of the lateral femoral condyle. Thus, it is possible that slightly different slice locations may be called the "midline" slice from one imaging session to another. Slight out-of-plane rotations or medial-lateral translations may cause different areas of cartilage to be sampled. However, slice thickness of these two-dimensional images is 3-4 mm, which is fairly large compared to the width of the condyle (approximately 20, i.e., Figure 5). If the trauma is large enough to affect a larger area within the joint, this technique should still be able to track a patient's progress with a similar outcome. To ensure the same cartilage is being tracked, a program such as Univiewer.exe (a DICOM viewing program) can be used to assess which acquired slice aligns the best over time with the first acquisition. Unfortunately, this of course happens after the data has been acquired.

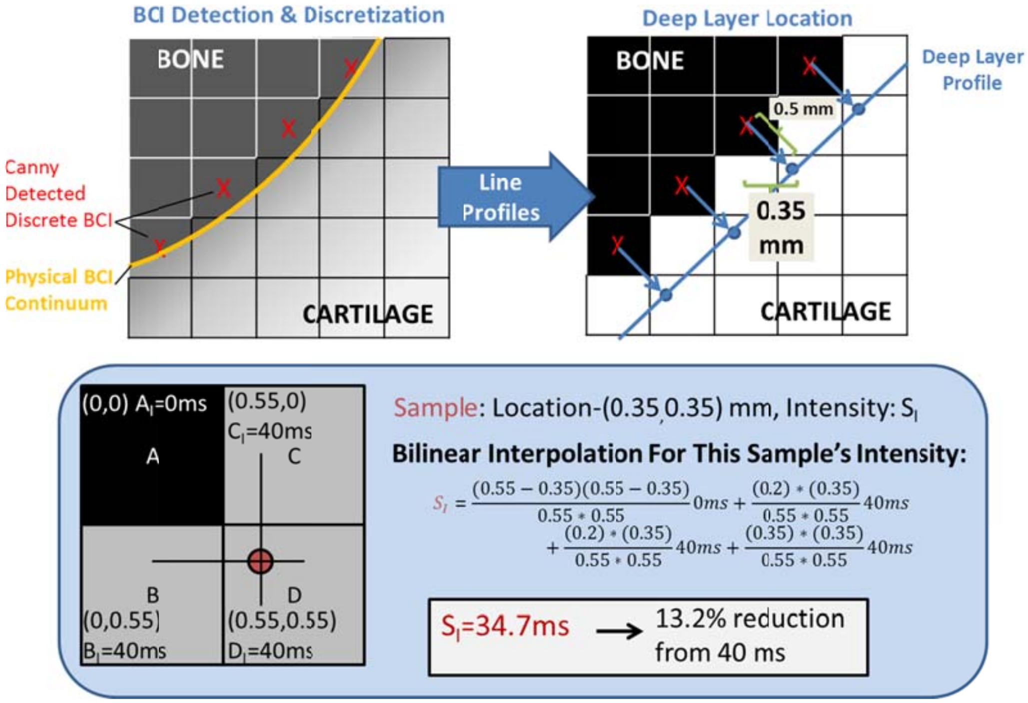

Figure 26. The worst-case scenario for partial-volume effects affecting the deep layer's relaxation time calculation. However, this is one of the inherent issues with discretization of a signal, followed by interpolation back to some sort of continuum.

One way to ensure that the same locations would be sampled would be to image the whole knee joint using three-dimensional T1rho imaging; however clinical time restrictions may prove to limit the number of T1rho images captured, and thus may limit T1rho to two-dimensional imaging. If this turns out to be the case, then perhaps the technician may use a reference image showing the previous imaging session's slice selection to improve consistency. As a follow-up during image-processing, a user could then register the slice locations from the different imaging sessions to a single, three-dimensional morphometric image dataset (i.e. T2 FATSAT), and quantify the misalignment of the different two-dimensional T1rho datasets.

While not solving the problem of technician-placement dependency (since the data would have already been collected), this would at least give the researcher or clinician an idea of the degree of misalignment.

Some of the basic concepts for line profile analysis were first presented by Sirisha Tadimalla [93]. These concepts include sampling from a determined bone-cartilage interface outwards to the superficial surface in known increments, using an ellipse for creating line profiles, and using an anatomic landmark based upon the sulcus region. What is novel in this work is the application of the Canny filter for objective edge-detection of the bone-cartilage interface, geometric interpretation of the sulcus area for a more objective landmark than was previously used, not including the sulcus region within the smoothing ellipse fits, automated limitations in how far the bone-cartilage interface would be detected superiorly, and the anthropometric radius and polar-sampling scheme for patient normalization.

While not without its limitations of technician placement dependency and lack of cartilage surface boundary detection, the Line Profile Analysis technique is a simple, easy-to-use objective method of measuring T1rho relaxation times from the relaxometry maps. It provides a way for specific patient information and population changes within the articular cartilage to be studied in both healthy and at-risk groups. The posterior portion of the midline of the lateral condyle provides an excellent example to study T1rho relaxation within cartilage, and as such will be used in the remainder of this work. Yet, extension of this technique could easily be applied to other portions within the midline of the lateral femoral condyle (i.e. anterior portion of the condyle). Line Profile Analysis allows for more localized cartilage changes (three zonal layers, 0-90° from posterior ridge) to be recorded than previous region-of-interest methodologies could provide, and therefore would give a clinician a more specific idea as to the location and extent of cartilage damage for treatment in an ACL-rupture patient.

CHAPTER 5: INTERPRETATION OF 3.0T T1RHO

5.1 An Introduction

Now that the appropriate tools have been developed to make and analyze T1rho relaxation measurements (Chapters 3 and 4), a demonstration of their utility is presented in this chapter. Within this section, there will be several short hypotheses posed to answer the question of whether T1rho MRI can quantify and track longitudinal changes within a clinically-relevant patient model. First, a definition of normal and injured cartilage T1rho relaxation values will be defined based upon healthy and pre-surgery ACL-rupture patients. If there is a difference between these values, as determined by statistical analyses, then T1rho will be proven to be sensitive to early stages of cartilage injury. Next, to see if T1rho is sensitive to changes within cartilage over time, post-surgery follow-up T1rho images of those same ACL-rupture patients will be analyzed. If some of these patients maintain significantly different T1rho relaxation times as compared to normal cartilage, that may be indicative that the cartilage in these patients is not returning to its normal, healthy state, but is instead progressing towards PTOA. With the results of these studies, and if these hypotheses are proven true, a method and quantitative T1rho threshold value will be proposed as a "Clinical Risk Factor" to be used in future studies of ACL-rupture patients in academic and clinical settings, to help the investigator know whether a patient may be at a higher risk of PTOA development. This chapter will answer how to acquire and interpret T1rho's information at 3.0T, the widely employed research field strength.

A new statistical analysis will also be used in this chapter to determine whether changes over time (with regard to hot spot involvement) are significant over the entire population. Pearson's correlation coefficient provides a way to tell whether two variables have a linear relationship. The sample correlation coefficient (which ranges from -1 to 1) can be described by the equation below (where x_{bar} and y_{bar} are the means of the x and y variables, [78]).

$$r = \frac{\sum(x-\bar{x})(y-\bar{y})}{\sqrt{\sum(x-\bar{x})^2\sum(y-\bar{y})^2}}$$

With its application in this section, a correlation value (r) will be found for cartilage T1rho relaxation values (x) with respect to time (y). To determine whether the correlation is significant (p=0.05), the *r* coefficient will be used to find a t-value (as shown below), which can be used to find the probability within a normal distribution (n=number of samples).

$$t = r\sqrt{\frac{n-2}{1-r^2}}$$

5.2 Can T1rho Clearly Distinguish Between Healthy and Injured Cartilage Using Line Profile Analysis?

Several studies have investigated T1rho's ability to differentiate healthy and injured cartilage, but many simply look at large regions of interest, which may dilute the sensitivity to specific regions' acute injuries [3, 39, 56]. Some studies have looked at cartilage relaxation times using b-splines and zonal definitions. However, these have been based on normalized cartilage depths, which may not be the most accurate to use over time since cartilage thins from the surface downward [83]. Therefore, this study will utilize the patient-specific, Line Profile Analysis tool in order to determine T1rho's sensitivity towards acute injuries.

Normal, healthy subjects were scanned on a 3.0T Siemens scanner to define an age-matched baseline database. Two of the normal subjects were scanned using an oblique-sagittal angle on three alternating days (Normal 3,4), one subject was scanned once using an oblique-sagittal view (Normal 2), one subject was scanned at a sagittal view (Normal 6), and one subject had two separate scans in which one was and the other was oblique-sagittal (i.e., aligned with the midline of the lateral femoral condyle, Normal 7). These five normal subjects were chosen since they were approximately the same age as many of the ACL-rupture patients. All ACL-rupture patients were scanned at 3.0T prior to surgical reconstruction, at approximately zero to four weeks post-injury. Oblique-sagittal T1rho images were captured in order to maintain clinical relevancy; many knee injury scans are performed in this view to better distinguish ruptured ACLs ([94], APPENDIX A: Image Sequence and Patient Information).

The ACL subjects were broken into two separate groups for line profile analysis. ACL Group 1 were patients with six or seven spin-lock (SL) images collected (AOSSM 2-9, CORT 1-4), and ACL Group 2 were patients with four or five SL images collected (AOSSM 1, CORT 5, CORT 7-18). Relaxation maps were made for each of the groups (using all available SL images), and two sets of relaxation maps were made for the normal subjects. The first set of maps (Normal Group 1) were to be more similar to those of ACL Group 1, where SL=5,10,20,40,60,80ms. The second set of normal maps (Normal Group 2) were similar to those seen in ACL Group 2, where SL = 10,20,40,60ms. Since it was previously demonstrated that the number of SL times can greatly affect the reported T1rho relaxation parameters (see Section 3.5 3.5), defining a set of normal relaxation times for both ACL groups was necessary to provide an equivalent baseline T1rho set. Using the Line Profile Analysis tool, T1rho measurements were made from each of the relaxation maps of the posterior femoral condyle for each of the subjects. The same sample locations were used for both sets of normal subject relaxation maps.

For each cartilage layer, a “hot spot” relaxation threshold was defined as being one standard deviation above the normal subjects’ relaxation times across the entire condyle (i.e., not angle-specific). Since it has been observed that damaged cartilage has higher relaxation times than intact cartilage [61], it was thought that if observed relaxation times were greater than this hot spot threshold, then this would be indicative of injured cartilage, and thus demonstrate T1rho’s sensitivity in this clinically relevant injury model. Any relaxation times which were greater than 150ms were rejected in the final analysis, since this has been previously identified as fluid signal in T1rho images [66]. Other values which were rejected were visually verified as full-thickness sampling of fluid or some other tissue interference as apparent by the 20ms SL image (Figure D-1, Table D-1). The fraction of each line profile which was beyond this hot spot relaxation threshold was reported, to help determine the extent of above-normal cartilage. A student t-test was also employed in each ACL patient (and to the overall ACL composite relaxation times) to test whether the depth-dependent T1rho relaxation times for each zone were significantly different than those found from the normal subjects ($p \leq 0.05$).

The results for the normal data groups are shown in Figure 27. The distributions found for each cartilage layer are also shown, and give an idea of how normally-distributed the healthy subjects' data are through the use of the normal "bell" curves (displayed in red). The most variability (widest normal distribution) was the deep layer for Group 1. The relaxation times for the deep and radial layers of Group 2 were typically lower than those of Group 1 in reference to condylar location (middle Figure 27). However, a student t-test revealed that the values found for the deep cartilage layers were significantly different (probability value (pval, p) <0.05) between the two groups, whereas the other two layers were not statistically different (pval>0.05). This is important because it demonstrates that the SL times chosen for a given image study will affect the outcome of the relaxation parameters, and that it was appropriate to create a separate set of normal times for comparison to the Group 2 ACL patients. Had the normal cartilage values for Group 1 been used as a comparison to the ACL patients in Group 2, then the deep zone's hot-spot threshold value would have been an inappropriate normal baseline for these subjects.

Individually, Group 1's normal subject mean cartilage values (± standard deviation) were 43.75 (± 15.17) ms, 45.95 (± 9.98) ms, and 46.89 (± 8.64) ms for the deep (0.5mm from the bone-cartilage interface), radial (1.0mm), and transitional (1.5mm) zones of cartilage. The subsequent hot spot thresholds were 58.92 ms, 55.93 ms, and 55.53 ms. The source of a larger standard deviation (15.17 ms vs. < 10ms, and thus not as "normal" distribution) for the deep layer was some relaxation time data (45-70°) in Normal 6 that was high compared to a lot of the other normal subjects. This could be traced back to the inclusion of the 0.5ms SL image, since relaxation times were not as high when the 0.5ms was excluded (like in the 4 SL Group 2 data). However, since there was no visible fluid or other unusual tissue signal (such as those reported in Table D-1) within this range, it would have been inappropriate to ignore it, since this was part of the normal subject population. Given this possible outlier, the locations of "hot spots" were also examined for the normal subjects. The total percentage of all the normal subject's condyles which was above the hot spot threshold was 7.5% (0-90°, for all layers and subjects). The comparisons made between the normal subjects' relaxation times and those of the Group 1 ACL patients are in Table D-2.

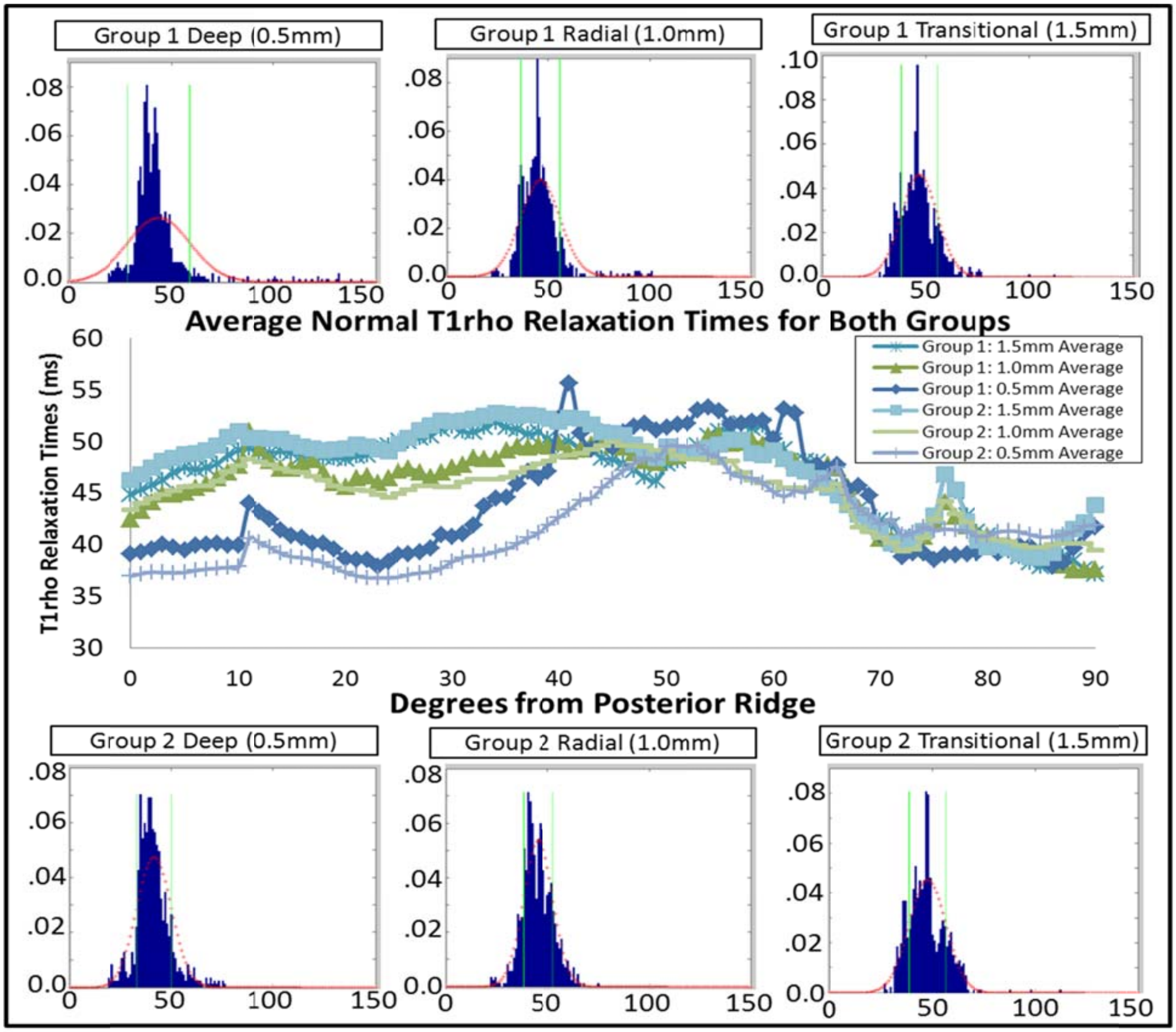

Figure 27. The average zonal relaxation times for the two groups of normal cartilage relaxation maps, as reported by degrees from the posterior ridge (middle). The subset distributions represent the percentage of the total counts of relaxation times in each zone (from 0 to 150 ms left to right, blue), an estimation of what a normal distribution looks like given the counts (red), and the standard deviations (green). The green bar on the right side of each subset demarcates the hot spot threshold for each layer. The deep layer for Group 1 is not as normally distributed, due to some data in Normal 6.

Group 2's normal subject mean cartilage values (± standard deviation) were 41.56 (± 8.41) ms, 45.22 (± 7.41) ms, and 47.63 (± 8.83) ms for the deep, radial, and transitional zones of cartilage, and had hot spot thresholds of 49.97 ms, 52.63 ms, and 56.46 ms, respectively. Similarly, the total percentage of the Group 2 normal subject values which were above the hot spot threshold was 11.1%. These values and the ACL comparisons are reported in Table D-3.

Most but not all of the ACL patients' cartilage layers were significantly different from normal. Significant differences may indicate the level of trauma during ACL rupture (bolded in Table D-2 and Table D-3). Half of patients in Group 1 had significantly different relaxation values for their full thickness cartilage (all three layers), and ten out of the twelve patients in Group 2 fell into this category. Interestingly in Group 2, two patients (CORT5, CORT17) had significantly *lower* relaxation values than the normal subjects. It is unclear at this time if these patients' cartilage was not affected in these areas during injury, or if the small number of SL images captured (4) greatly diminished their overall T1rho relaxation parameters. When patients' relaxation times were combined together and compared to the composite normal groups, each of the three cartilage layers (overall) were significantly different ($p<0.05$). Since most of the patients had significantly higher relaxation values and since much of that elevation was above the hot-spot threshold, there is indication that T1rho is sensitive to the differences seen *in vivo* in pre-surgery ACL-rupture patients.

Considering that the majority of the patients' layers were significantly different (even with some portion of the normal cartilage being above this threshold) compared to the healthy subjects' cartilage, a general trend for ACL injury location was hypothesized. One paradigm for cartilage injury during ACL-rupture is that the sudden impact mainly affects the cartilage near the sulcus region, as evidenced by the location of bone bruises in MRI [95]. To see if this was the case, the hot spot locations of all twenty-five pre-surgery datasets were recorded and counted for each layer (deep, radial, transitional) and for each single degree increment (0-90° from the posterior ridge, Figure 28). Theoretically, if trauma tended to occur close to the sulcus region, then an inverse relationship would exist between the number of hot spots and the degree location (i.e. higher hot spot count near 0°).

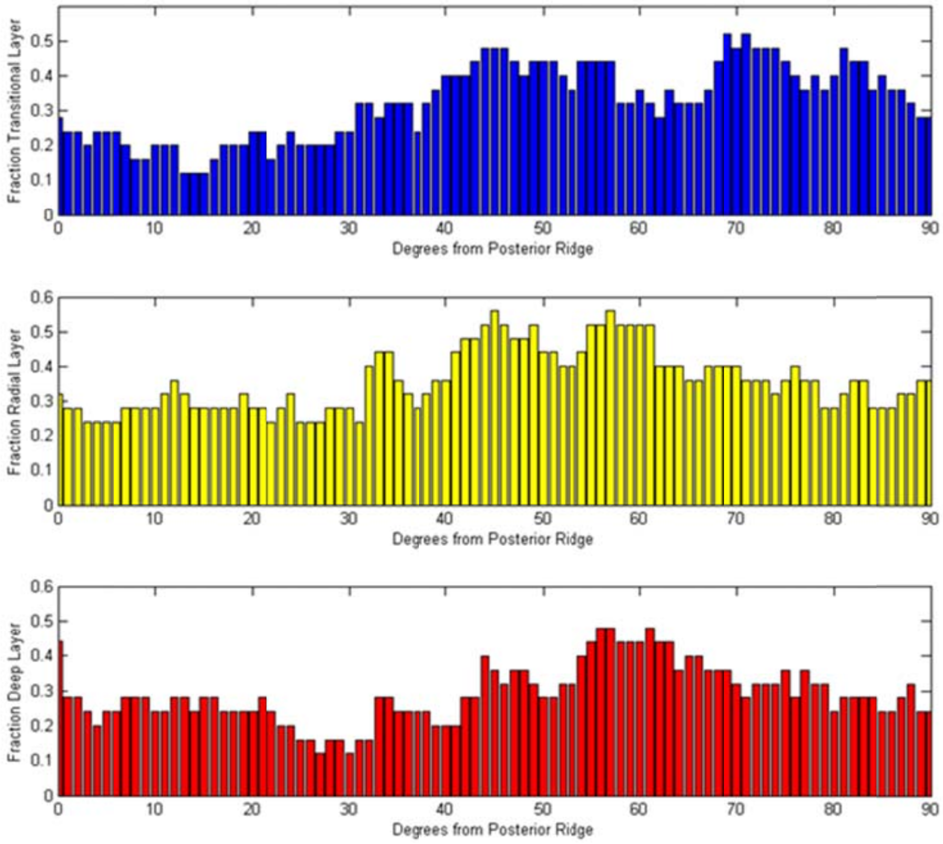

Figure 28. The number of hot spots for each cartilage layer (red: deep, yellow: radial, blue: transitional) was counted for each degree location within the posterior portion of the condyle for all twenty-five pre-surgery ACL-rupture patients. The histogram shows the fraction of patients who had a hot spot at each degree location.

The total number locations encompassed within the hot spot threshold (25 patients x 0-90° (91) samples = 2275 possible occurrences) seen in all pre-surgery images for the deep layer was 658 (28.92% average hot-spot coverage for each ACL patient), the radial layer had 814 (35.78%), and the transitional layer had 738 instances (32.44%). In Figure 28, the fraction of patients who had a hot spot at each particular degree location is shown. There were at least three patients (six in the radial layer) who had a hot spot elevation throughout the entire condylar cartilage. The maximum number of patients with a hot spot location was 12 for the deep layer, 14 for the radial layer, and 13 for the transitional layer. Only 27.2%, 26.3%, and 21.0% of all of the hot spots recorded in the deep, radial, and transitional layers (respectively) were seen for angles less than 30° the weight-bearing area and closest to the sulcus [91]. This suggests that there is not a predominant pattern of injury near the sulcus region.

The values and a potential threshold value for determining injured with respect to normal T1rho relaxation times has confirmed the first hypothesis posed in this chapter. While a portion of the normal cartilage is above the hot spot threshold, the ACL-rupture patients' zonal relaxation times were still significantly above the normals' distributions, thereby confirming the hypothesis.

5.3 Can T1rho Detect and Quantify Injured Cartilage Changes Over Time?

The previous section demonstrated T1rho's sensitivity to early differences between injured and healthy cartilage, and provided a cartilage injury threshold derived from normal cartilage T1rho relaxation time distributions. One study observed ACL patients longitudinally, with a single-year follow-up, but used a region-based approach [66]. In this section, the hot-spot threshold was applied to measure more local change of cartilage relaxation values over time. If the same cartilage areas in a subject continue to have elevated T1rho relaxation times as determined by the hot-spot threshold, these areas may have sustained irreparable damage, which could lead to PTOA. Theoretically, then, this would show that T1rho could be used clinically as an early biomarker for cartilage degradation and PTOA.

For this portion of the work, some of the ACL patients (13) from the previous section returned for follow-up T1rho images. Two additional subjects (CORT 6, CORT11) were also available for a 4 month follow-up image, but the pre-surgical images obtained were unusable due to technical difficulties. The follow-up scans were approximately 4 months (session B, 13 patients), 8 months (session C, 5 patients), and 12 months (session D, 2 patients) post-surgery, and followed the same T1rho imaging protocol the midline of the lateral femoral condyle as previously collected pre-operatively (Session A, APPENDIX A: Image Sequence and Patient Information). Only two returned for a one-year follow-up. As in many clinical follow-ups, the results from this study are limited by the small number of subjects returning at irregular intervals. However, this is on-going study, and stronger conclusions will be possible about this technique's beneficial dividends as follow-up numbers increase.

T1rho relaxation maps were made with the MRI_Relaxation_Map_Tool GUI (Chapter 3) using the SL=5,10,20,40,60,80ms images for each patient in ACL Group 1, and SL=12,20,40,60ms for those in ACL Group 2. Line profile analysis (Chapter 4) sampled T1rho relaxation times from 0 to 90° from the posterior ridge in the midline slice of the lateral femoral condyle. The normal subject data and hot-spot thresholds were used to determine the areas of potential cartilage damage in these ACL patients' post-surgery images. The location of each hot spot was recorded, and the overall fractions of involved cartilage were calculated for each zonal layer. A student t-test was applied to each layer to determine whether a patient's cartilage relaxation values were still significantly different from the normal population ($p < 0.05$, Table D-4-Table D-6). The student t-test was also used to determine overall whether each layer (composite) was still significantly different from the corresponding normal group at each follow-up session. These tests determine whether and where a patient's cartilage was affected by the ACL-rupture, even months after injury.

In addition to these observations, the portions of the cartilage which were above these hot-spot thresholds were tracked over the course of each patient's image sets. The total fraction of the condyle which was above the hot spot thresholds for the deep, radial, and transitional layers are reported in Table D-4, Table D-5, and Table D-6 respectively. These tables also contain the fraction of the condyle which was common in both pre- and post-surgical images as a denoted hot spot (i.e. hotspot found in 0-18° pre-op = 0.2 fraction of total condyle; 4 months post-op hotspot 0-9°, same as pre-op = 0.5, total condyle=0.1). Also, if a hot spot persists through different imaging sessions at a particular location, this may be indicative of sustained cartilage damage progressing toward PTOA. To visualize how these hot-spot locations changed over time, plots tracking each patient's total condylar involvement (as a hot spot) through each of the cartilage layers and through 0-90° were created (Figure 29; to see specific hot-spot locations for each individual, please refer to Figure D-2). Finally, the Pearson's correlation coefficient was used to determine if there was a linear relationship between the hot spot involvement over time considering all available subjects.

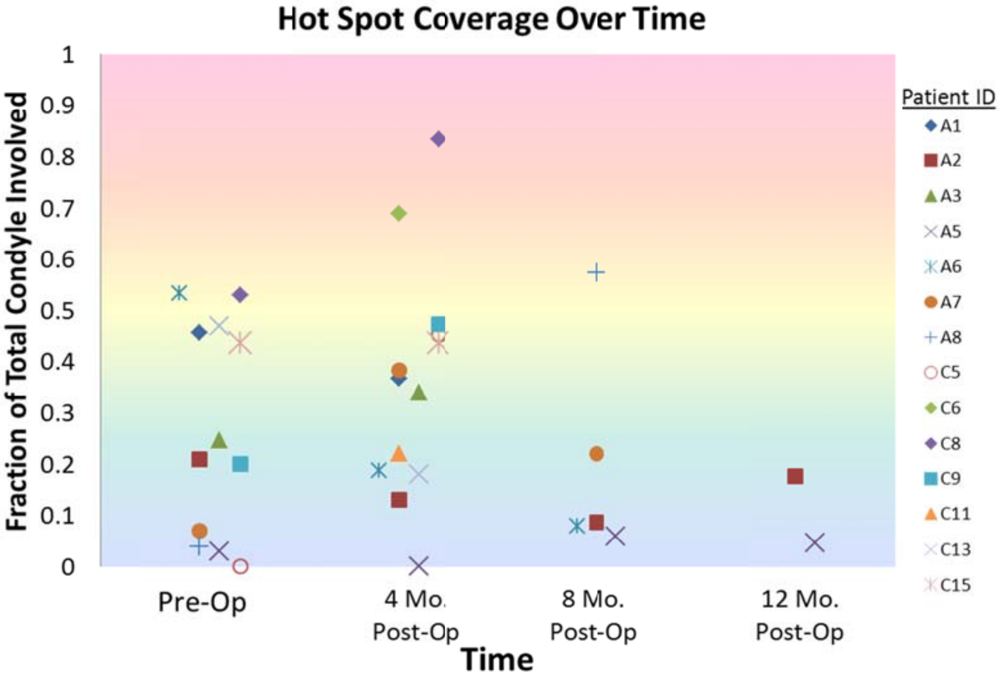

Figure 29. The total fraction of the condyle (deep, radial, and transitional layers combined) for each subject which was above the hot spot threshold varied considerably between subjects and over time.

Overall, most patients' cartilage layers were still significantly ($p<0.05$) above normal cartilage's relaxation times, even at 4, 8, and 12 months after surgery. Some patients (i.e. AOSSM 5, AOSSM 8), did not have consistent hot spot location as time progressed, but the majority of the patients did have continuation of some of the same hot spot locations in each of the different layers as time progressed after surgery. Some patients had full cartilage-thickness hot spots (i.e. AOSSM 7 at 4 Months post-surgery between 0-15°), which may be indicative of high trauma and fluid effusion. When comparing all of the patients' data with the student t-test, the deep layer at 8 months (p=0.07), and the radial layer (p=0.25) as well as the transitional layer (p=0.36) were statistically the same as the normal populations' data. All other layers were significantly different from the normal subjects' means. This would suggest that at four months after surgery, the cartilage is still experiencing increased water to PG ratio, while at 8 and 12 months it is starting to return back to a more normal state. This trend was also reflected by the hot spot coverage. In general, the average fraction of the condyle covered by hot spots rose from the pre-surgery images to the 4 month post-op images, and then tended to decrease as time progressed (top, Figure 30). The fraction of persistent hot-spots was also plotted as the mean across all individuals (bottom, Figure 30).

Overall, the fraction of persistent hot-spots decreased over time as well; this made sense since total hot-spot involvement also decreased. However, above-normal relaxation times are seen post-surgery even in parts of the cartilage which were not part of the pre-op hot-spot locations. This suggests that biochemical changes within the cartilage propagate or shift as time progresses to 4 months, thereby causing these higher relaxation values. Perhaps a better point in time to image ACL-rupture patients would be around this 4 month mark, given that there seems to be an overall increase in relaxation times until this juncture. Then, if a patient continued to have high relaxation times thereafter (since some cartilage layers return back to a normal state at 8-12 months, as determined by the overall results from the student t-test), the patient may then be considered to be at a higher-risk for developing PTOA.

To determine whether there was some correlation between time and hot spot involvement, the Pearson's correlation coefficient was found (Table 1). First, the total hot-spot involvement over time (pre-surgery to 12 months post-surgery) was examined. This had the smallest linear correlation overall, which makes sense since it seems (based on the means shown in the top of Figure 30) that there was more of a “peak” involvement (i.e., non-linear) at 4 months. The Pearson’s correlation coefficient was then applied to see if there was a greater linear correlation with hot spot involvement between pre-op and 4 months post-surgery, and between 4 months and 12 months post-surgery (to describe the “peak”). In fact, there was a stronger correlation within these time frames (as indicated by r values closer to -1 and 1), but these were still not a significant correlation. Finally, the same hot spot involvement as pre-surgery (values seen in bottom of Figure 30) was also tested using the Pearson correlation coefficient, to find whether there was a significant correlation with a decreasing amount of hot-spot involvement as time progressed.

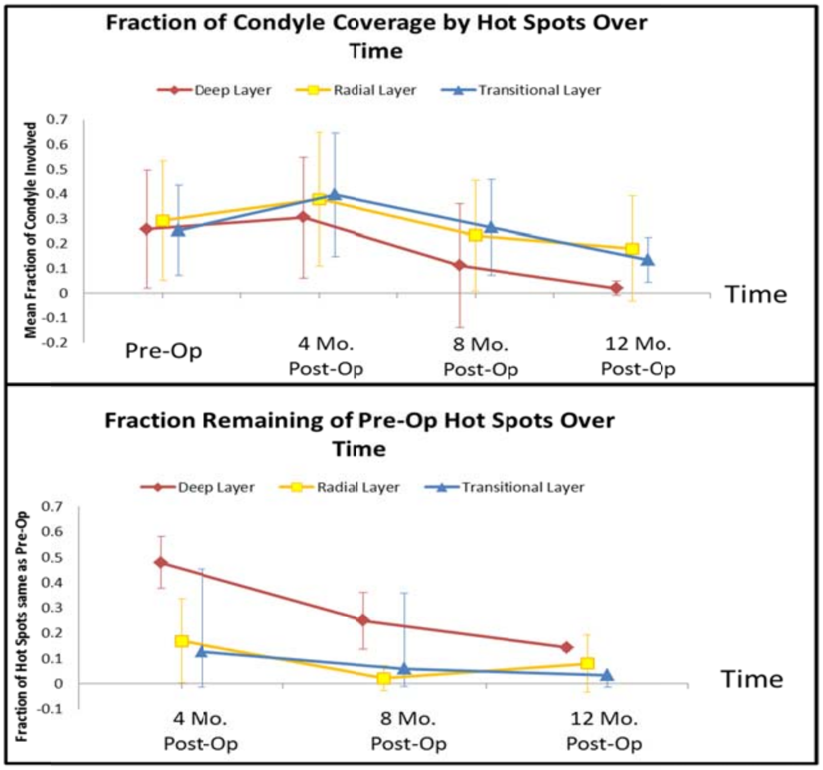

Figure 30. Average (± standard deviation bars) hot-spot condyle coverage show the general trend of T1rho’s sensitivity to cartilage changes over time. For all layers (top), it appears that the portion of cartilage which is above normal increases at 4 months post-operation, but then steadily decreases. The mean fraction of a hot spot’s persistence is shown below for each of the three layers. Pre-Op: n=13, 4 Mo. Post-Op: n=13, 8 Mo. Post-Op: n=5, 12 Mo. Post-Op: n=2.

Table 1. Correlation statistics analysis for various hot spot involvement over time within the all of the ACL rupture patients' condyles.

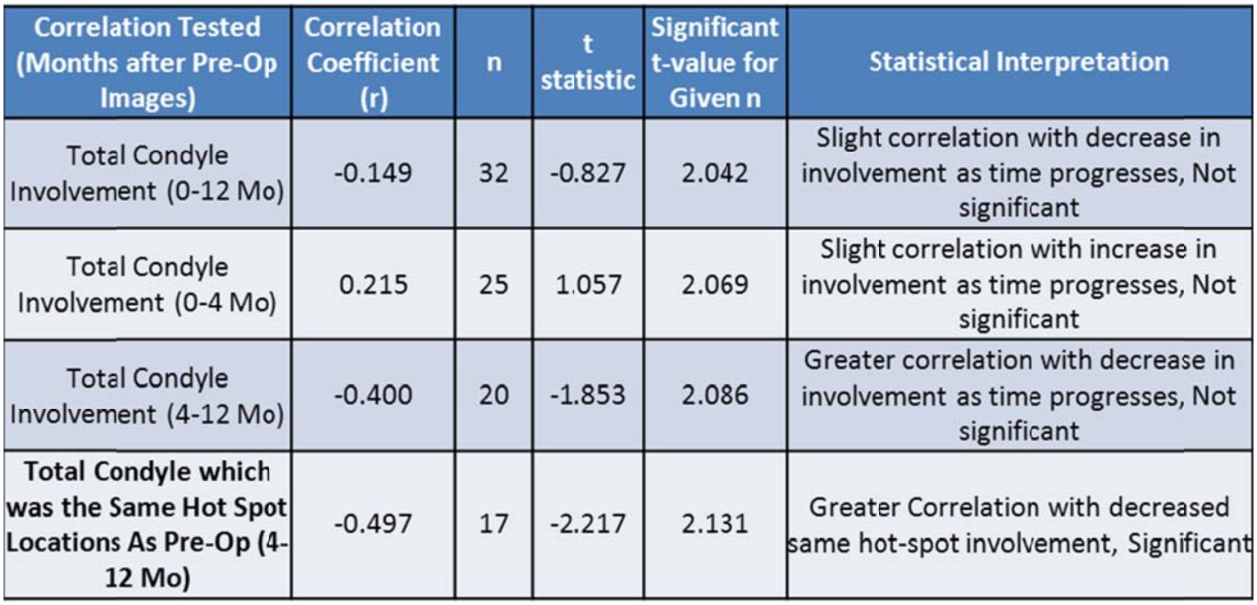

Correlation Tested (Months after Pre-Op Images)	Correlation Coefficient (r)	n	t statistic	Significant t-value for Given n	Statistical Interpretation
Total Condyle Involvement (0-12 Mo)	-0.149	32	-0.827	2.042	Slight correlation with decrease in involvement as time progresses, Not significant
Total Condyle Involvement (0-4 Mo)	0.215	25	1.057	2.069	Slight correlation with increase in involvement as time progresses, Not significant
Total Condyle Involvement (4-12 Mo)	-0.400	20	-1.853	2.086	Greater correlation with decrease in involvement as time progresses, Not significant
Total Condyle which was the Same Hot Spot Locations As Pre-Op (4-12 Mo)	-0.497	17	-2.217	2.131	Greater Correlation with decreased same hot-spot involvement, Significant

Quantifiable changes have been tracked over time in a patient population with this hot spot threshold, and thus the second hypothesis posed in this section has been proven. While it is uncertain as to which patients will develop PTOA in this on-going study, the information found from these hot spot investigations highlight interesting trends.

5.4 Discussion and Conclusions About T1rho Interpretation in a Clinical Model at a Research Field Strength

This chapter showed how to acquire and interpret T1rho's quantitative information at 3.0T. After relaxation maps were made for both healthy subjects and ACL-rupture patients, Line Profile Analysis was employed to measure T1rho relaxation times. These tools were used to consistently acquire the T1rho data at 3.0T, and pose interpretation of the data to answer the first two questions posed at the start of this work.

A quantifiable difference was determined between healthy and injured cartilage within patients. With the line profiles sampling through each nominal cartilage zone, the similarity between a patient's cartilage and the normal subjects' T1rho relaxation behavior was significantly elevated ($p<0.05$) from a healthy patient. Therefore, this showed that T1rho can differentiate cartilage of normal versus ACL-injured joints.

A hot spot threshold was proposed to measure a patient's cartilage relaxation behavior over time. This hot spot threshold was defined as being one standard deviation above the normal subjects' mean T1rho relaxation time for each zone of the cartilage. This initial value was chosen to demonstrate potential stratification of increased T1rho relaxation times correlated to damaged cartilage [61]. Locations where a patient's relaxation time exceeded this hot spot threshold (a.k.a hot spots) were recorded along each line profile (0-90°, three layers) in the patient-specific coordinate system, thereby improving likelihood of successfully answering the second hypothesis of this work (is there a meaningful pre-screening measure which can be tracked over time?). While the Line Profile Analysis' dependence on proper MR technician alignment between scanning sessions is omnipresent, the changes reported from some of the ACL patients' return visits may be indicative of overall cartilage health at various stages of PTOA development. The hot spots varied spatially from one patient to another in the pre-surgery images, which is a possible indication that the blunt trauma during acute ACL-rupture may occur anywhere within the posterior lateral femoral condyle. This differs slightly from some previous studies, which theorized that most cartilage trauma occurs near the sulcus during such an injury [37]. Patient follow-up was possible in approximately half of the patients, but the number of post-surgery visits by these patients varied greatly from one session to another. This small number of patients, especially at 12 months post-surgery, limits the number of strong conclusions that can be made about T1rho's predictive capabilities at this time, since it is not known whether some or all of these patients will develop PTOA.

However, one conclusion that can be drawn at this time is that T1rho does show quantifiable differences at different imaging sessions for a given patient. The hot spots track the biochemical abnormalities (i.e. increased water to PG ratio) seen within these patients. While hot spot emergence did not seem to follow any sort of pattern in some patients (i.e. AOSSM 5), the majority of patients had at least some of the same portion of the cartilage that remained above the hot spot threshold in follow-up images. The general trend (Figure 30) shows that there is an overall decrease in the average portion of the condyle identified as a “hot spot” at 8 months. While this correlation was stronger (total hot spot involvement decreasing from 4 to 12 months post-operatively), it was not significant when examining the entire population at this time. The one significant correlation suggests that the initial hot spot locations are indeed diminishing over time, thereby suggesting that the cartilage begins to return to a more normal state. However, the overall predictive capabilities will be better understood with more patient enrollment.

While only time and future studies will clearly tell if this hot spot threshold is the quintessential “Clinical Risk Factor” associated with PTOA progression, this chapter demonstrated a means to provide a pre-screening procedure at 3.0T using a quantifiable measure to differentiate T1rho relaxation times found within healthy and injured cartilage. These initial findings suggest that the hot spot threshold can register cartilage changes over time, and that there is a significant difference (full thickness at pre-surgery and 4 months post-surgery by the student t-test) between healthy and injured cartilage, thereby affirmatively answering the first two hypotheses at the beginning of the present work.

CHAPTER 6: TOWARD DATA CONSISTENCY ACROSS CENTERS

6.1 A Brief Introduction

To become a valuable clinical tool, T1rho research performed on 3.0T scanners must be translated to 1.5T scanners, which are used by 60-75% of practices in the United States [6]. To quantify the quality and utility of 1.5T T1rho imaging in the clinical setting, this chapter compares cartilage T1rho relaxation times and the general T1rho image properties (i.e. SNR) of a cartilage-surrogate phantom and one healthy subject on same-day data collected from 1.5T and 3.0T MRI scanners. Data quality will be assessed by the image signal and noise statistics, as well as the data's ability to discern differences through cartilage layers. Both topics are important to affirm 1.5T T1rho as a clinically useful sequence. Cartilage should be distinguishable by a high, positive relative contrast to other joint tissues. Secondly, for potential therapy to gage the severity of cartilage injury, it is important to know whether the T1rho relaxation values at 1.5T are discriminatory using current analysis capabilities. Same-day imaging with the same parameters at 1.5T and 3.0T are used to understand magnet influences on T1rho relaxation times, such that measures of cartilage changes and differences across platforms can be translated.

6.2 Methods

Three normal subjects without knee pain (females, 23, 24, 30 yr) were selected for this study. Same day scans were performed to eliminate day-to-day variability. T1rho images were acquired using a 3T Siemens TIM Trio scanner and an Avanto 1.5T scanner, both with a quadrature knee coil. Twelve spin-lock (SL) times were chosen to characterize T1rho relaxation constants on both scans (SL=0.5, 5, 10, 15, 20, 25, 30, 40, 50, 60, 70, 80 ms) in a 2D oblique-sagittal slice (aligned with the lateral femoral condyle) through the approximate midline of the left lateral femoral condyle (other parameters in Table A-2). The previously described carrageenan-agarose phantom (Figure 10) was also imaged using the same parameters on both the 1.5T and 3.0T MR scanners. The sagittal midline of the phantom was used for subsequent analysis.

T1ρ relaxation maps were created using all twelve spin-lock images for both the phantom and normal subjects, and line profile analysis was used to extract *in vivo* T1rho relaxation times. A student's two-tailed t-test with equal variance was used to determine the probability of the resulting T1rho relaxation times to be the same across systems with different B_0 (significant p=0.05).

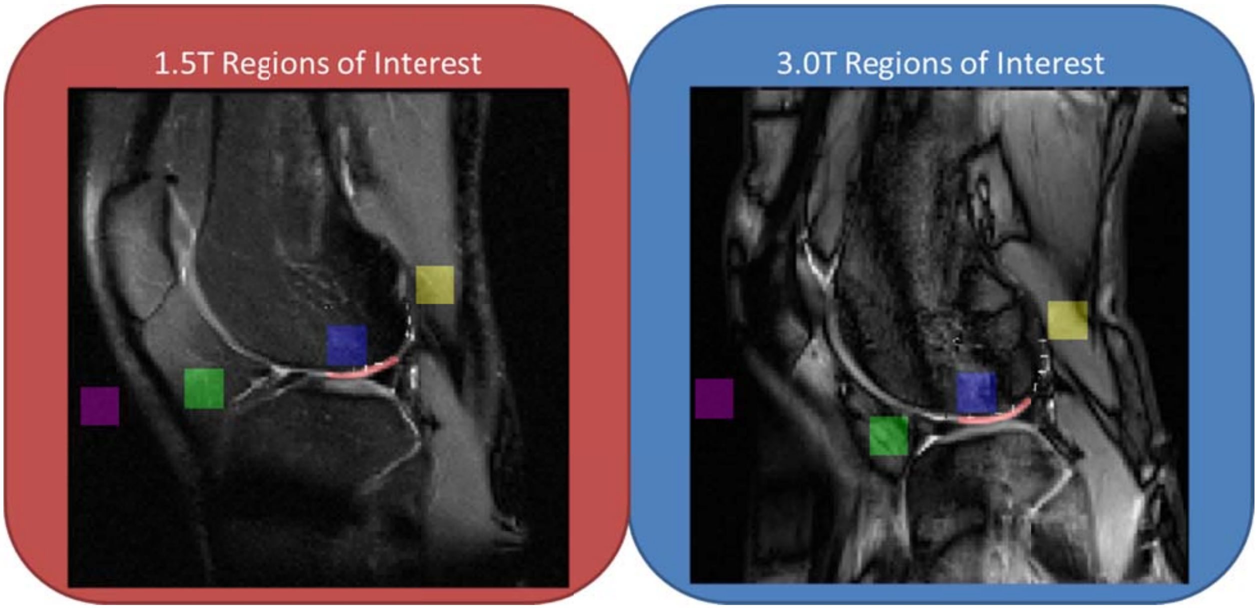

Figure 31. User-defined regions of interest (ROI) for both 1.5T and 3.0T datasets, as shown on the 20ms SL T1rho image of Normal 7. The colored areas represent the ROIs sampled for each tissue type: infrapatellar fat pad (green), femur bone (blue), gastrocnemius muscle (yellow), and air (magenta, noise measurement). The full-thickness cartilage ROI (red) was manually selected from 0-50° posterior to the posterior ridge.

The previously identified line profile coordinate system was referenced to approximate the same tissue locations in the normal subjects' scans. In order to determine how discernable cartilage signal is compared to other tissues, such that Line Profile Analysis (or others) may properly identify the raw cartilage information (not relaxation times) from other tissues during segmentation, it was important to examine other tissues' signals for comparisons (even though this is not the main focus of this cartilage-specific sequence). Square tissue regions (bone, fat, muscle) for contrast comparisons with respect to cartilage, and air (for noise measurements) were selected, whereas manual segmentation was used for the full cartilage thickness (Figure 31). The bone ROI was directly superior to the posterior ridge within the femur, the muscle ROI was placed within the gastrocnemius muscle, fat information was gathered in the infrapatellar fat pad region, and lastly the air ROI was defined outside of the knee. By using the Line Profile Analysis' coordinate system, the majority of the pixels in each ROI in the 3.0T images would be the same as those found in the 1.5T images, ensuring direct comparisons (assuming proper technician placement). For the phantom, rectangular regions (n=378 voxels) in each of the five gels were selected, and a portion of the air was also selected. Since these were assumed to be homogeneous gels that ought to have the same relaxation behavior throughout, the ROIs were placed in approximately the same place on both the 1.5T and 3.0T images, but exact location determination was less scrutinized.

Typical imaging parameters were calculated (Figure 32). Noise for each image was derived from the standard deviation found from within the air ROI, a typical way to measure noise. Signal-to-Noise Ratio (SNR) was defined as the mean signal intensity of a tissue divided by the noise of the image [52]. This parameter gives a sense of the tissue intensity compared to the background noise inherent in the system. Parameters which quantify the contrast between tissues indicate the radiologist's ability to visually distinguish tissues, such as Signal-Difference-to-Noise Ratio (SDNR), Contrast-to-Noise Ratio (CNR), and Relative-Contrast (RC). While not pertinent for tissues other than cartilage, knowing cartilage's contrast to these tissues is essential in order to properly segment it. The definitions for calculation of these parameters are given in Figure 32 [50, 62]. CNR indicates which tissue has a higher signal intensity based on its sign, whereas SDNR indicates the overall difference. RC provides a normalized contrast that does not account for the noise in an image. Overall, the SNR, SDNR, CNR, and RC were calculated for each region of fat, bone, muscle, and cartilage within each *in vivo* image. Since there were no other tissues in the phantom, only SNR was calculated for each gel.

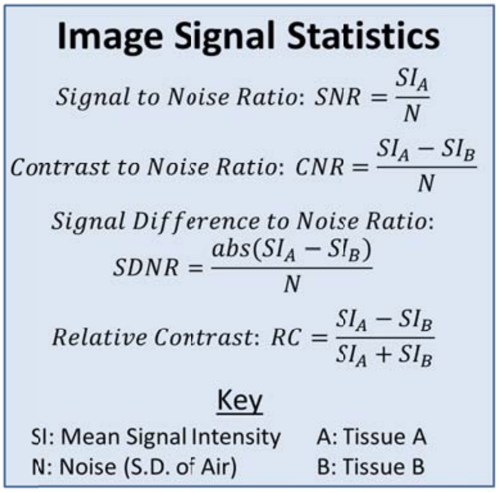

Image Signal Statistics

$$\textit{Signal to Noise Ratio}: SNR = \frac{SI_A}{N}$$

$$\textit{Contrast to Noise Ratio}: CNR = \frac{SI_A - SI_B}{N}$$

$$\textit{Signal Difference to Noise Ratio}: SDNR = \frac{abs(SI_A - SI_B)}{N}$$

$$\textit{Relative Contrast}: RC = \frac{SI_A - SI_B}{SI_A + SI_B}$$

Key

SI: Mean Signal Intensity
N: Noise (S.D. of Air)
A: Tissue A
B: Tissue B

Figure 32. The summary for calculating all signal and noise statistics presented to compare 1.5T and 3.0T T1rho datasets.

To understand the relative differences in these parameters across B_0 fields, ratios between the values collected at 3.0T and 1.5T were made. For example, if the SNR of cartilage in the 20ms 3.0T image (85.4) was divided by the 1.5T 20 ms cartilage's SNR (45.3), to determine the overall increase in SNR (1.88) between these systems. Similar ratios were made for the other imaging parameters.

6.3 1.5T vs. 3.0T T1rho Comparison Results

For the phantom gels, the average (±standard deviation) relaxation times from the regions of interest (ROI) were 132.3 (±8.5) ms, 48.9 (±1.3) ms, 56.2 (±3.6) ms, 29.9 (±0.8) ms, 23.8 (±0.6) ms for the 1.5T 12 SL relaxation map images, and 125.2 (±9.2) ms, 45.3 (±2.3) ms, 54.0 (±3.8) ms, 28.0 (±0.9) ms, 22.8 (±1.6) ms for the 3.0T 12 SL relaxation map images' 1%, 2%, 3%, 4%, and 5% agarose gels, respectively. Small standard deviations indicate that these were indeed homogeneous gels. All ROIs' mean relaxation times in the phantom were significantly different ($p << 0.01$, student t-test) at 1.5T compared to 3.0T, with the mean 3.0T relaxation times being lower than those at 1.5T.

Overall, the cartilage T1rho relaxation times tended to increase from the deep to transitional layers for both the 1.5T and 3.0T cases (Figure 33). The T1rho relaxation times from the 3.0T scan were generally lower than those found at 1.5T (average across all three layers Figure 33, right). The mean (± standard deviation) relaxation times for Normal 7 across all three layers were 50.0 (±4.1) ms at 1.5T and 44.0 (±2.3)ms at 3.0T. Similarly, the mean relaxation times for Normal 8 were 46.6 (±2.2) ms at 1.5T and 41.3 (±2.7) ms at 3.0T, whereas in Normal 9 the mean relaxation times were 49.7 (±3.4) ms at 1.5T and 45.4 (±2.9) ms at 3.0T. Inter-magnet comparisons of the three normal subjects combined (all sampled 0-50° from the posterior ridge except where fluid interfered) revealed that the relaxation times for the deep (0.5mm) and radial (1.0mm) zones proved to be significantly different ($p<<0.01$, student t-test), but the transitional (1.5mm) layer's relaxation times were found to be statistically the same on both B_0 field strengths ($p=0.25$). 3.0T Intra-magnet cartilage zonal comparisons showed all three layers had statistically distinct relaxation behavior (deep vs. radial $p=1.4e-13$, deep vs. transitional $p=4.0e-34$, radial vs. transitional $p= 1.3e-14$), while within the 1.5T data, the radial compared to the transitional layer was the only intra-magnet comparison which was statistically different ($p=0.02$, deep vs. radial=0.11, deep vs. transitional=0.34).

In the phantom, the signal-to-noise ratio (SNR) in most of the SL images was greater in the 3.0T data compared to the 1.5T (Figure 34). The average (±standard deviation) 3.0T to 1.5T SNR ratio across all five of the gels and SL images was 1.51 (±0.24). The 5% agarose region had the smallest signal compared to the other gels, and therefore its SNR was the smallest. This is why it had the smallest 3.0T to 1.5T ratio as well. The ratios for 3.0T to 1.5T were calculated for the various *in vivo* tissues' noise and contrast statistics (Figure 35, Table D-7). The average 3.0T to 1.5T ratio for cartilage across all three subjects and all spin-lock images was 2.08 (± 0.96). For each of the tissue contrast comparisons (Table D-7), the tissue listed first was considered "tissue A" with respect to calculation (Figure 32). Most of the *in vivo* tissue comparisons were higher at 3.0T compared to those seen in 1.5T.

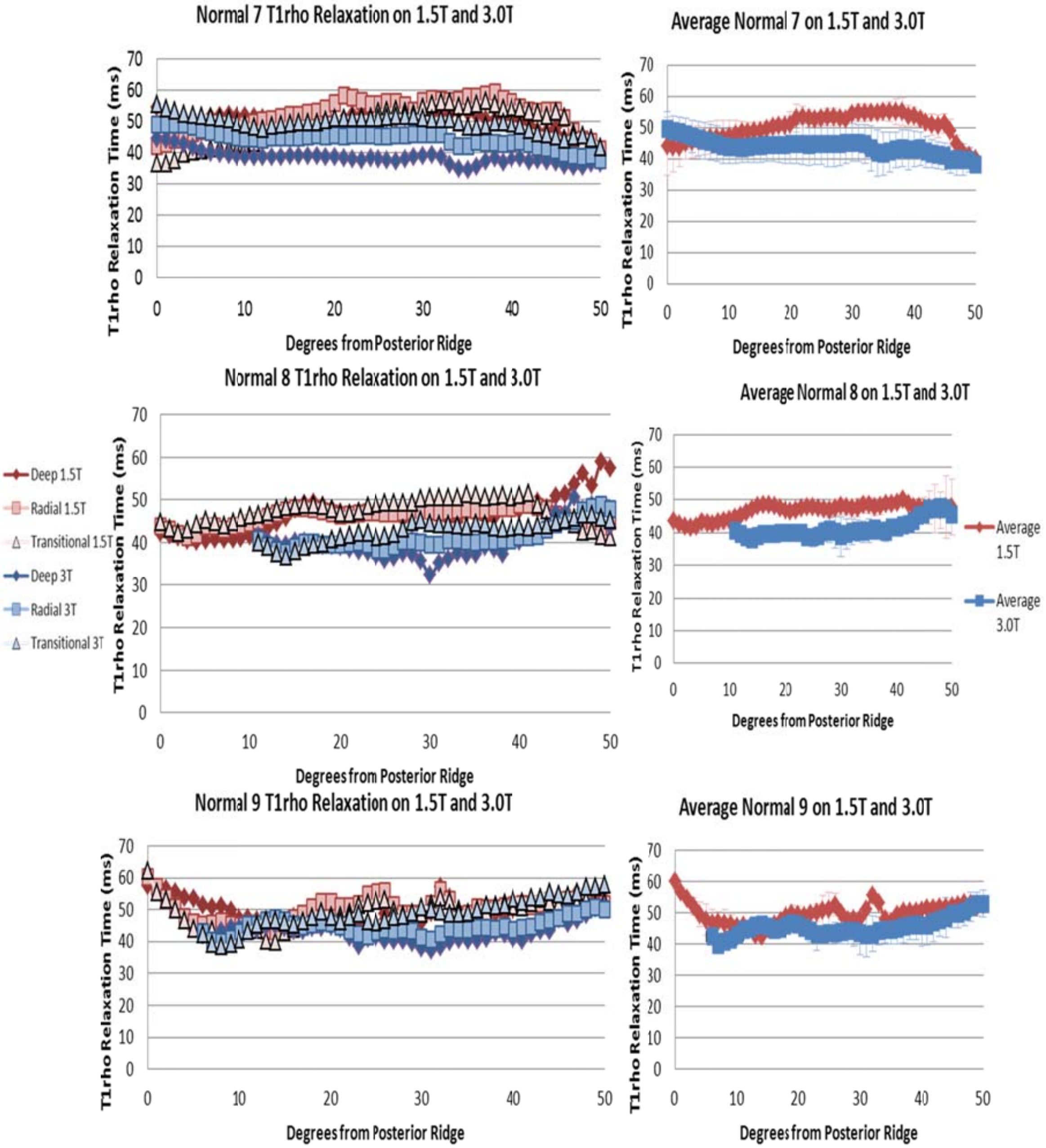

Figure 33. Relaxation times for line profiles found for the deep (0.5mm), radial (1.0mm), and superficial (1.5mm) layers through the cartilage of Normal 7, 8, 9 (left). Average relaxation times (standard deviation bars) across the three layers (right) help demonstrate mean 3.0T values being less than 1.5T values.

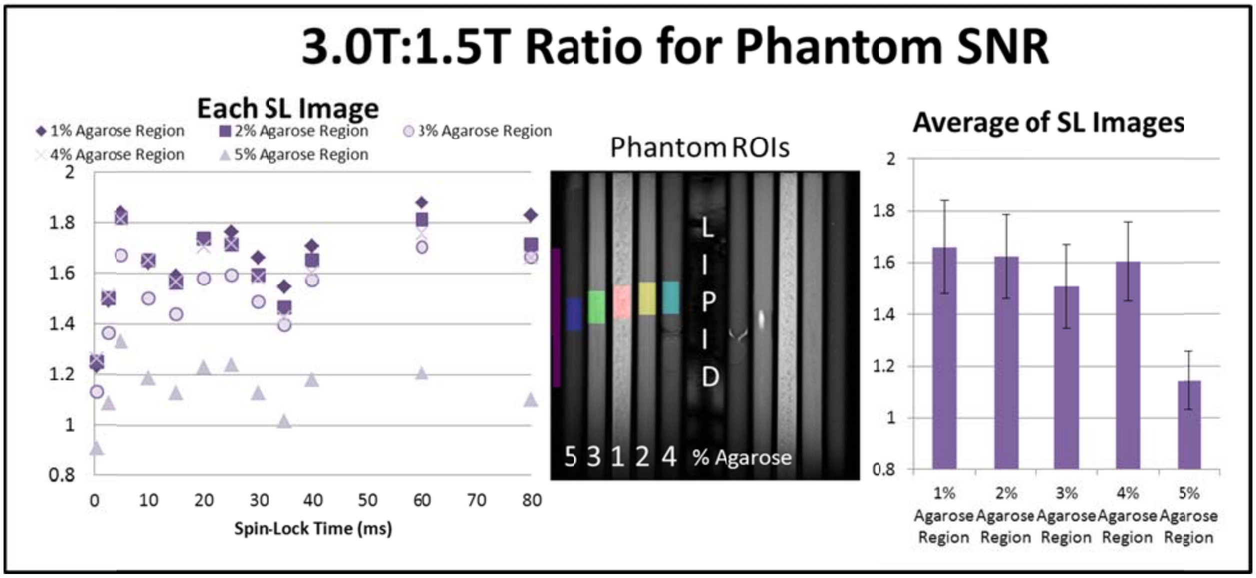

Figure 34. 3.0T compared to 1.5T Signal-to-noise (SNR) ratio for each of the phantom ROIs (highlighted, middle). For each agarose region, the 3.0T:1.5T ratio was calculated for the average (right) across SL images and individual SL images (left). Only the 1.5T 0.5ms SL image's SNR in the 5% agarose region was greater than the 3.0T SNR data.

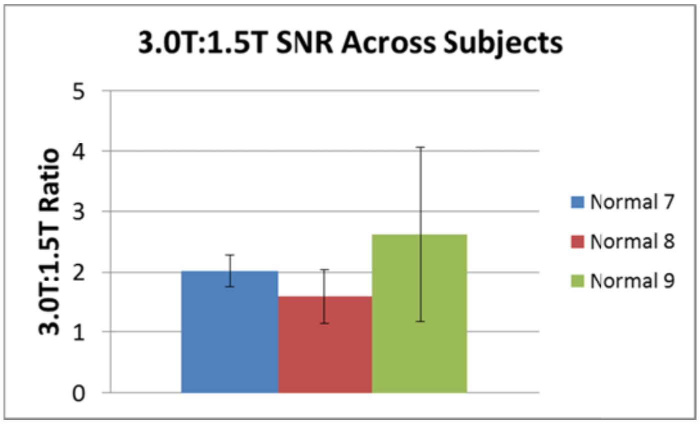

Figure 35. Average Signal-to-Noise (SNR) increase when comparing 3.0T to 1.5T *in vivo* for T1rho SL images. While all were greater at 3T, Normal 7 was the least variable.

6.4 Discussion and Conclusions

Some of these results correlate well with general MR physics theory, while others are slightly less expected. A higher B_0 magnetic field will directly affect (increase) the possible amount of signal that a tissue will produce, but as the length of the decay (spin-lock time) increases, the B_0 effect will diminish as well. This means that shorter 3.0T SL image times would have higher signal intensity than those seen at 1.5T, but longer SL times would be more similar due to decay in both B_0 systems. This translates to different exponential decay curve shapes, since individual voxel signal intensities for each of the SL images dictate the shape of the exponential decay. Therefore, it is not surprising that the resulting T1rho relaxation constants were significantly different from the 3.0T system to the 1.5T system. The more "shallow" exponential decay seen at 1.5T translates to a longer T1rho relaxation constant, as was seen in the phantom and most of the *in vivo* line profiles' results. The relaxation times for particular cartilage layers were visually and statistically distinct when compared using a student t-test at 3.0T, but only one such comparison was distinct at 1.5T ($p<0.05$, radial vs. transitional layer). The line profiles used in this study show that cartilage layers' relaxation times can be different at 1.5T, but maybe fewer layers (i.e. combine into two layers sampled instead of three), or only a region-of-interest approach may be applicable because of this lack of differentiation at 1.5T. In other words, Line Profile Analysis (as it stands) may be "overkill" for 1.5T analysis. One thing to consider is that this study was performed in healthy cartilage, so it may be inappropriate to infer whether T1rho is able to distinguish clinically significant differences in ACL-rupture patients.

Approximate doubling of the SNR of the cartilage occurred for 3.0T T1rho compared to 1.5T T1rho, following theory that the signal intensity (compared to noise) is linearly proportional to the strength of the B_0 field. Since the B_0 field doubled, the mean SNR approximately doubled for the cartilage (Figure 35) across the three subjects (even though there was some variability in Normal 8 and 9). However, the phantom images' SNR did not improve by a factor of two within any of the gels (Figure 34). This is interesting because the gels' gadolinium trichloride and agarose contents, which are responsible for the different signals in each of the concentric rings, were guaranteed not to change between imaging sessions.

While SNR is high in both datasets, it is important for further image analysis to discern the cartilage from other tissue types; hence other imaging parameters pertaining to contrast were examined (Table D-7). In all *in vivo* images on both systems, the cartilage was brighter than the muscle, fat and bone. However, the relative contrast of the cartilage to the bone was somewhat diminished in some of the early SL images due to the higher bone signal. This may exacerbate finding the bone-cartilage interface, unless some sort of multidirectional, noise-resistant (i.e., hysterisis) edge-detection algorithm, like the Canny operator, is used.

Even though morphology may be easier to visualize in 3.0T T1rho images, the overall quality of the T1rho images captured at 1.5T were still relatively good. Relaxation times between cartilage layers were still some-what distinguishable (low p values). Signal intensity of the cartilage was still greater than that of other tissues, aiding in post-processing segmentation efforts, since brighter tissues would be easier to visually identify in comparison to a darker background. Even though the ROI data and line profile data had many samples, limitations of this 1.5T versus 3.0T study include small *in vivo* subject size (n=3), and that this was collected only in healthy subjects. Therefore, in order for T1rho to be used in a 1.5T clinical scanner, further studies would need to be performed to determine what T1rho relaxation times are indicative of normal and traumatized cartilage at this clinical field strength. However, based on these preliminary results, meaningful 1.5T T1rho cartilage imaging may be possible, due to cartilage's high SNR and CNR (compared to other tissues), and to T1rho relaxation times retaining the ability to differentiate some cartilage zones for potential prognosis capabilities.

CHAPTER 7: FINAL DISCUSSION AND CONCLUSIONS

The overarching question posed and the motivation for this work was whether T1rho MRI could be applied to an at-risk population and translated into a clinical setting. ACL rupture is a large risk factor in development of post-traumatic osteoarthritis (PTOA), and so this work has developed tools to investigate cartilage's compositional changes over time in this population. Since only 5% of the scanners in the nation are 3.0T field strength, the clinical utility of 1.5T T1rho imaging was also examined. However, several things must be considered prior to determination of T1rho's clinical utility.

The first question posed was whether there was a quantifiable difference between healthy and injured cartilage in patients. As was found in others' work, there was a significant difference ($p<0.05$) between healthy subjects' and the majority of patients' cartilage. Unlike others' work (ROI-based), localized cartilage trauma could be determined through the use of Line Profile Analysis, which gathered data from 0-90° from the posterior ridge, in three different cartilage zones. Assuming that MRI technician placement of the 2D-imaging plane was fairly consistent over the imaging sessions, changes in the cartilage T1rho relaxation times could be tracked longitudinally. This led to the ability to answer the second question posed.

A "hot spot" was proposed as the indicative measure which could be tracked over time. The threshold value for hot spot delineation was one standard deviation above the normal subjects' mean T1rho relaxation time for each zonal layer. This higher relaxation time presumably would be indicative of higher water content and early PG loss, which are some of the earliest changes in cartilage biochemistry leading to PTOA. Hot spot location varied for each patient, and there was no clear trend of hot spot spatial dependence, such as near the sulcus. However, in the majority of the patients who came back for follow-up studies, at least some portion of the hot spots identified at pre-surgery remained hot-spots post-operatively, with a general "peak' hot spot involvement found at 4 months post-operatively. These continued elevated T1rho regions may potentially be sites of cartilage softening and degeneration as time progresses. Unfortunately, at this time, there was not a significant linear correlation with regard to the total hot spot involvement over time across all the subjects, but perhaps more patient follow-ups will increase this correlation (for now a more patient-by-patient analysis may yield the most benefit).

Since this is an ongoing study, end stage information is not available, and therefore it is not clear at this time which individuals will develop PTOA. In the future, the areas which were denoted as hot spots in these early images can be compared to morphometric images taken at later stage. Since morphologic changes are slower (one group recently reported no significant changes at 7 years post-operatively, [38]), comparisons with morphometric changes were not performed, even for the two patients who had one-year follow-up images. However, with the aid of semi-automated cartilage segmentation programs, such as the LOGISMOS program developed by Yin et al., tracking changes in cartilage thickness could be implemented [96]. With such a program, and by using image registration techniques (T1rho to morphometric data), the predictive power of these hot spots could be validated. Therefore, if proven to be a measure of future cartilage thinning, these hot spots could be used as a meaningful pre-screening procedure, one which would be easy to implement and track using Line Profile Analysis. While a clinically relevant measure was proposed for the second question of this work, like the rest of T1rho research (long term biochemical and morphometric comparisons have not been made in the literature as of this time), only time will tell whether this is an appropriate predictor of OA progression.

The last question posed was whether the same or similar quality of T1rho data could be obtained at 1.5T as that which was shown at 3.0T. Identification from other soft tissues (ability to segment) was one quality, and the other was whether 1.5T relaxation times were still sensitive to normal proteoglycan zonal variation (as shown by statistical significance). This last point, PG sensitivity, is the driving purpose behind T1rho as a quantitative sequence. In preliminary experiments, it was found that the signal-to-noise ratio (SNR) at 3.0T was approximately twice that found at 1.5T *in vivo*, which followed theory since the imaging parameters (i.e. resolution) remained the same in both scanning environments. The improvement in SNR in the phantom was closer to 1.51; perhaps with additional constituents that are more akin to natural cartilage (i.e., PG) the phantom could serve as an excellent control for cross-center studies. In the *in vivo* study, the cartilage had high SNR at both B_0 values, and it had the highest signal intensity compared to the other tissues examined (i.e. positive contrast-to-noise ratio). This means that for post-processing (i.e. segmentation), the cartilage should still be distinguishable from the other tissues at 1.5T, such as bone. Even though the overall SNR is less at 1.5T than at 3.0T, the relative contrast between the bone and cartilage is still large enough that a multi-directional Canny filter can easily detect the bone-cartilage interface. Distinct zonal layers' relaxation times were partially maintained at 1.5T (n=3). However, more *in vivo* subjects should be used to validate this observation, since only the radial and transitional layers were statistically different ($p<0.05$) at 1.5T, whereas all layers were different at 3.0T. Further verification of 1.5T's zonal specificity should be pursued (with perhaps a different zonal model being used), since different cartilage layers should have different relaxation times due to the varying PG content, and this will ultimately determine how specific longitudinal patient tracking can be at this most clinically available field strength.

The time needed to scan an ACL-rupture patient to get full diagnostic images will influence what variants of T1rho scanning would be achievable (2D or 3D). Resolution of ~0.55mm (in-plane) is needed in order to achieve approximately 4-5 voxels' worth of sampling throughout an average cartilage thickness, which will allow for 2-3 voxels free of partial volume effects. This sets the acquisition time to approximately one minute per slice per spin-lock (SL) image, as was found using the fast-spin-echo sequence presented herein. Without application of other fast-imaging techniques (i.e. partial k-space sampling, parallel imaging), this means that the number of SL images acquired will be approximately the same as the T1rho sequence scan time (i.e., 6 spin-lock images through one slice is approximately 6 minutes). While there may be variability between clinics in the amount of time each physician is willing to allocate for additional scans, at the Sports Medicine Clinic at the University of Iowa, it is thought that an additional 10-15 minutes might be possible to add onto the standard MRI scanning procedure. With this time frame and the fast-spin echo sequence used, two 2D slices with 6 or 7 SL times, or a 3D T1rho sequence (20 slices) with only 4 SL times may be acquired. As was shown (Chapter 3), the SL images captured will affect the resulting T1rho relaxation time. Preliminary results show that 4 SL may not be sufficient for achieving accurate T1rho relaxation times (since 8 SL images had the lowest sum of square error compared to 12 SL maps), but more *in vivo* tests are needed. This may limit T1rho to 2D imaging, unless fast-imaging acquisition techniques are applied (which may impart some artifact), or unless absolutely appropriate SL times are determined to enable 3D imaging to truly capture T1rho behavior.

Overall, T1rho is sensitive to water/PG content, but the relaxation times are also sensitive to the B_0, B_1, and the spin-lock times used to acquire images. Therefore, in order to make T1rho imaging a clinical reality, several steps must be taken prior to patient scanning. A cartilage-specific phantom, similar to the one used in this work, should be used in each institution for regular tuning purposes (i.e. to correct for scanner drift). This phantom would also provide a baseline for any imaging studies that were desired, such as determining “normal” and “abnormal” cartilage signals if different B_0 and B_1 fields were used than those studied in this work. Nevertheless, the sequence shown in this work with at least one 2D T1rho slice with multiple SL (6-8) would be appendable to a clinical examination given time restrictions. Incorporating the T1rho sequence into an ACL-rupture clinical exam could be done by adding the T1rho preparatory pulse (spin-lock pulse) to a standard spin-echo sequence, and other than the preliminary pulse programming, would not require exogenous contrast (i.e., dGEMRIC) or special hardware (i.e., sodium imaging). For analysis of the data, tools like the MRI_Relaxation_Map_Tool and Line Profile Analysis GUIs would create a relatively fast, easy-to-use interface for any technician, clinician, or researcher to track a patient’s data and perhaps use to develop patient-specific treatment plans.

In conclusion, this work has demonstrated that T1rho can be used in an at-risk patient population to provide information about biochemical, early PTOA-like cartilage changes, and with just a few additional steps could be translated into a clinical setting.

APPENDIX A: IMAGE SEQUENCE AND PATIENT INFORMATION

Table A-1 . Subject demographics and data sequences collected for each individual.

Normal Subject			AOSSM ACL Patients (3.0T)			CORT ACL Patients (3.0T)					
#	Age	Other	#	Age	Scan	#	Age	Scan	#	Age	Scan
1	59 M	3.0T, 3Dy	1	19F	A,B	1	23F	A	10	25F	A
2	23 F	3.0T, 3Dy	2	20F	A,B,C,D	2	20F	A	11	24F	A,B
3	22 M	3.0T, 3Dy	3	28M	A,B	3	25M	A	13	21M	A,B
4	22 F	3.0T, 3Dy	4	25M	A	4	22M	A	14	18M	A
5	59 M	3.0T, 3Dy	5	22F	A,B,C,D	5	22M	A,B	15	23F	A,B
6	23 M	3.0T, 3TS	6	18F	A,B,C	6	33F	B	16	22M	A
7	23 F	3TS, 3Tvs1.5T	7	29M	A,B,C	7	33M	A	17	26F	A
8	24 F	3Tvs1.5T	8	24M	A,C	8	40F	A,B	18	19M	A
9	30 F	3Tvs1.5T	9	21M	A	9	22M	A,B	-	-	-

Abbreviations: 3Dy=Scanned 3 days in one week, 3TS=3T sagittal scan, 3Tvs1.5T=same day scan at different B_0 fields. ACL-rupture patients' scans sessions were collected A=pre-surgery, B=4 months post-surgery, C= 8 months post-surgery, D= 12 months post-surgery.

Table A-2. T1rho sequence imaging parameters used for collected datasets.

Subject(s)		T1rho Sequence Parameters			
		Spin-Locks Captured (ms)	Slice Thickness/Slice Spacing (mm)	Echo Train Length/ Echo Time (ms)	Repetition Time (ms)
Normal Subjects	Normal 7-9 (3T vs 1.5T same-day scans)	0.5,5,10,15,20,25,30,40,50,60,70,80	4/8	13/10	3000
	Normal 1-5	5,10,20,40,60,80	4/8	12/7	3000
	Normal 6-7	0.5,5,10,20,40,60,80	4/8	13/10	3000
ACL Group 1	AOSSM1B-9A	5,10,20,40,60,80	3/6	7/9.5	3000
	CORT 1A-4A	0.2,5,10,20,40,60,80	4/0	1/3.05	6000
ACL Group 2	AOSSM1A	10,20,40,60,80	3/6	7/9.5	3000
	CORT 5A	0.2,10,20,40,60	4/0	1/2.94	6000
	CORT 6B-18A	12,20,40(36 CORT 7A),60	4/8	11/14	3000
OTHER	AKA14	0.2,5,10,20,40,60,80	3/6	7/12	3000
	Phantom (3T vs 1.5T same-day scans)	0.5,2.5,5,10,15,20,25,30,35,40,45,50,55,60,65,70,75,80	4/16	13/13	3000

Note: All scans also had 140 x 140 mm field of view, 180° flip angle, B_1= 400 Hz, and 0.55x0.55 in plane resolution

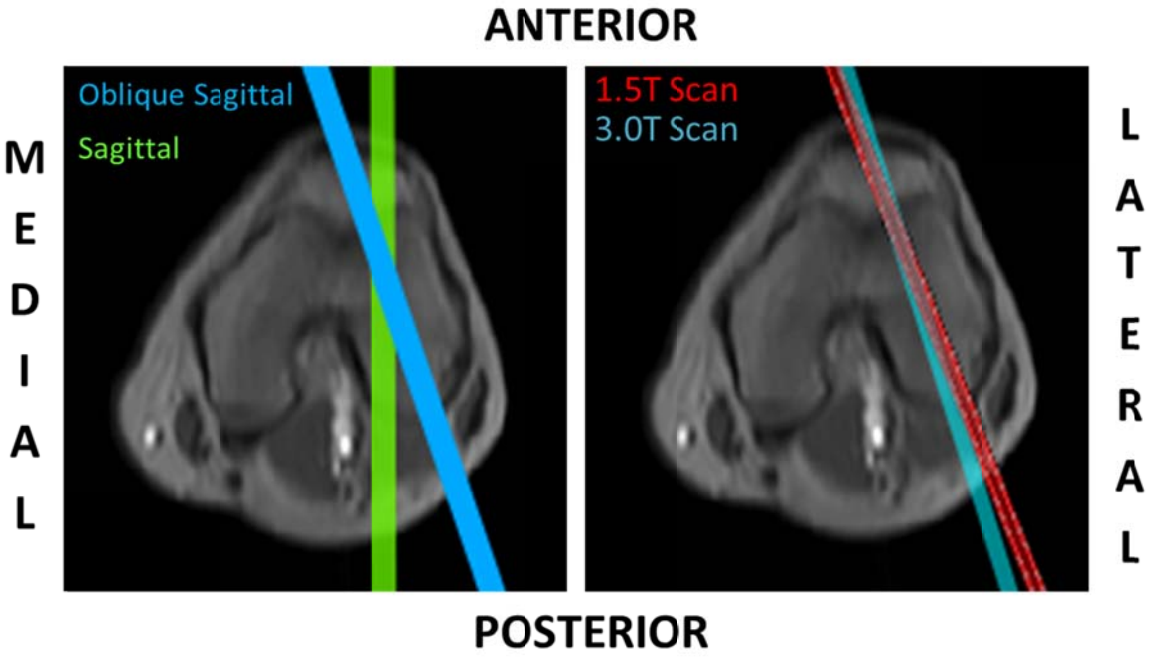

Figure A-1. Axial view of the femoral condyle for Normal 7. The lines in the left image show where the sagittal and oblique sagittal slice locations are selected with regards to the knee. Within the right image, the oblique sagittal slice locations from the 1.5T and 3.0T scans show the position and possible translational and rotational variation with regard to MR technician placement of the data set. Slice locations were correlated using UniViewer.exe, a DICOM viewing program.

APPENDIX B: AUXILIARY DATA COLLECTED IN CHAPTER 3

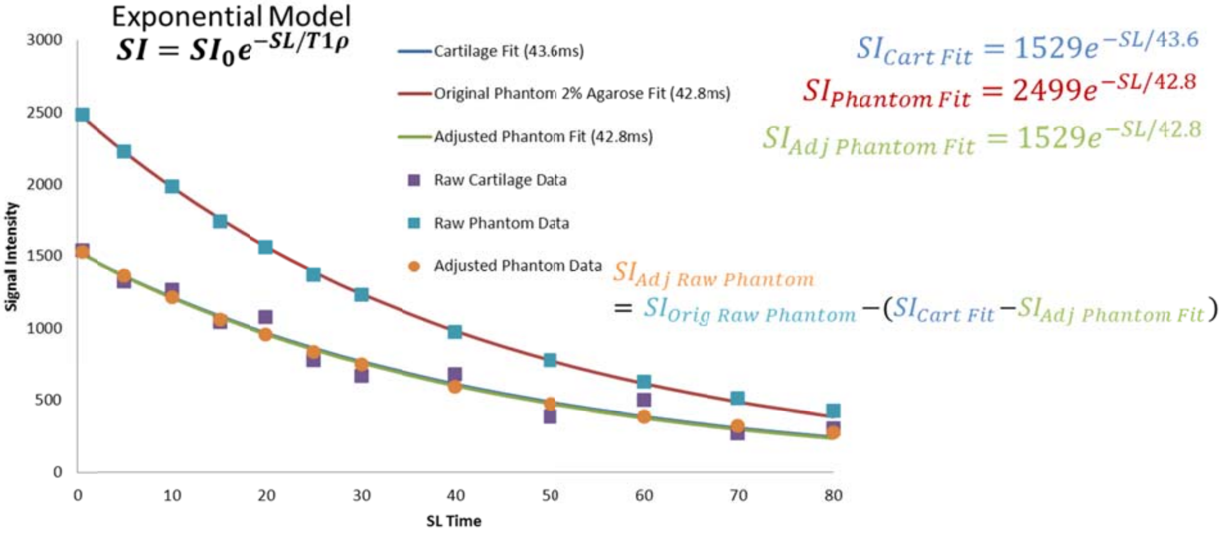

Figure B-1. Carrageenan-agarose phantom's relaxation behavior similarity to cartilage. The raw cartilage signal data (Normal 7) and the raw phantom data (2% agarose gel region) were sampled using 12 spin-lock times as shown. The curve-fitting procedure used to fit the data to the mono-exponential decay model was used to find the original signal intensity (SI_0) and T1rho relaxation time constants (43.6ms for cartilage, 42.8ms for phantom). Since raw absolute signal intensity values are just reflective of the digital gain settings determined by the scanner, and have no physical significance, the SI_0 from the cartilage fit was used in the adjusted phantom fit. The adjusted raw phantom data were calculated such that the offset (a proportionality constant, as shown by the $SI_{\text{Adjusted Raw Phantom}}$ calculation in the figure) from the fit was the same. Since the adjusted phantom fit practically overlays the cartilage fit, it is concluded that using the phantom as a cartilage-relaxation surrogate is appropriate. One thing to note is that the phantom data is not as varied as the cartilage (higher R^2 value in phantom), so this may indicate how the *in vivo* data differs from the phantom data.

Table B-1. Average and standard deviation of affine parameter values found for each 20 ms SL image of the different similarity metrics tested during validation of the automated SL registration technique in 3.2 Spin-Lock Images' Registration and Validation.

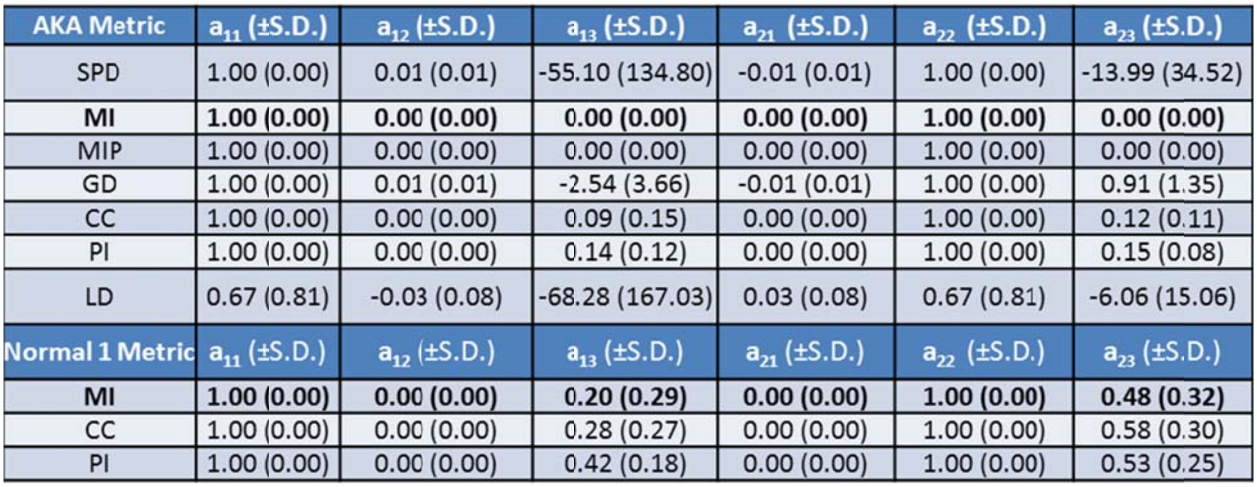

AKA Metric	a_{11} (±S.D.)	a_{12} (±S.D.)	a_{13} (±S.D.)	a_{21} (±S.D.)	a_{22} (±S.D.)	a_{23} (±S.D.)
SPD	1.00 (0.00)	0.01 (0.01)	-55.10 (134.80)	-0.01 (0.01)	1.00 (0.00)	-13.99 (34.52)
MI	**1.00 (0.00)**	**0.00 (0.00)**	**0.00 (0.00)**	**0.00 (0.00)**	**1.00 (0.00)**	**0.00 (0.00)**
MIP	1.00 (0.00)	0.00 (0.00)	0.00 (0.00)	0.00 (0.00)	1.00 (0.00)	0.00 (0.00)
GD	1.00 (0.00)	0.01 (0.01)	-2.54 (3.66)	-0.01 (0.01)	1.00 (0.00)	0.91 (1.35)
CC	1.00 (0.00)	0.00 (0.00)	0.09 (0.15)	0.00 (0.00)	1.00 (0.00)	0.12 (0.11)
PI	1.00 (0.00)	0.00 (0.00)	0.14 (0.12)	0.00 (0.00)	1.00 (0.00)	0.15 (0.08)
LD	0.67 (0.81)	-0.03 (0.08)	-68.28 (167.03)	0.03 (0.08)	0.67 (0.81)	-6.06 (15.06)
Normal 1 Metric	**a_{11} (±S.D.)**	**a_{12} (±S.D.)**	**a_{13} (±S.D.)**	**a_{21} (±S.D.)**	**a_{22} (±S.D.)**	**a_{23} (±S.D.)**
MI	**1.00 (0.00)**	**0.00 (0.00)**	**0.20 (0.29)**	**0.00 (0.00)**	**1.00 (0.00)**	**0.48 (0.32)**
CC	1.00 (0.00)	0.00 (0.00)	0.28 (0.27)	0.00 (0.00)	1.00 (0.00)	0.58 (0.30)
PI	1.00 (0.00)	0.00 (0.00)	0.42 (0.18)	0.00 (0.00)	1.00 (0.00)	0.53 (0.25)

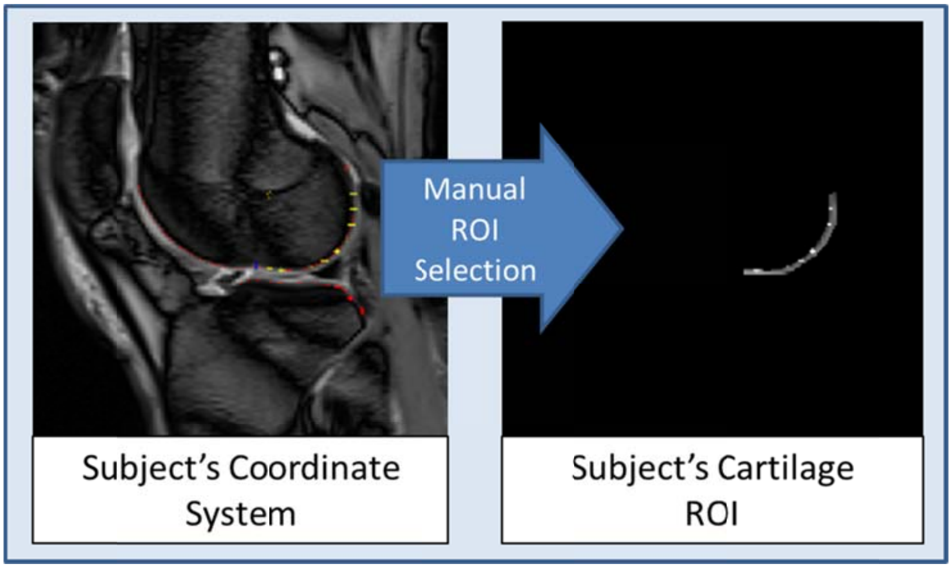

Figure B-2. The region-of-interest (ROI) selection which was used for comparing the different non-linear curve fitting techniques.

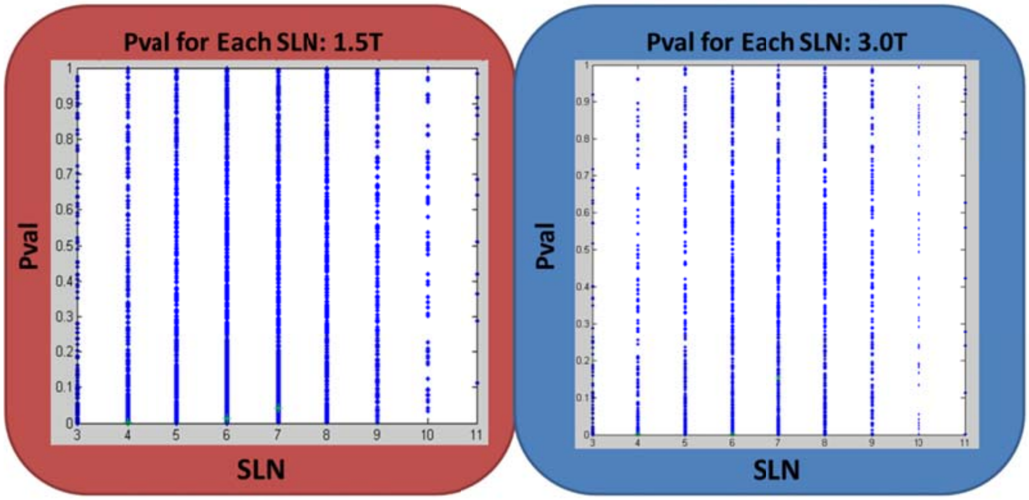

Figure B-3. The pvals determined for each of the *in vivo* spin-lock combinations (SLC), as sorted by the number of spin locks (SLN) for 1.5T and 3.0T images. As can be seen, there is no clear pattern with regard to SLN used and the pval found for a particular SLC image; each SLN has a score of pvals which range from near 0.0 to near 1.0.

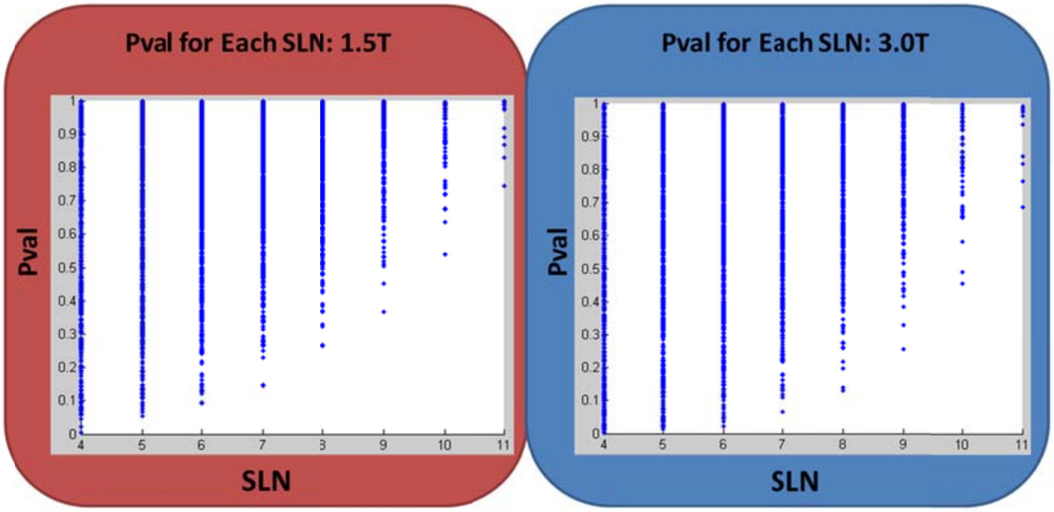

Figure B-4. The pvals determined for each of the phantom spin-lock combinations (SLC), as sorted by the number of spin locks (SLN) for 1.5T and 3.0T images.

Table B-2. The summary for the best *in vivo* spin-lock combinations for 3.0T and 1.5T, as described by the source.

SLN	Source	SLC (ms)	Mean Relax Value (±S.D.)	Pval	SSE (x 10^3)
3	1.5T, Pval	0.5,30,40	46.8(11.0)	0.9744	11.41*
	3.0T, Pval	10,25,80	45.2 (16.8)	0.9201	32.30
	OTM	5,30,80	47.0(15.7)/45.4 (11.0)	0.9681/0.6884	22.10/17.55*
4	1.5T, Pval	0.5,5,30,60	46.9(12.4)	0.9985	27.56
	3.0T, Pval	5,25,30,80	45.0 (11.3)	0.9631	17.53*
	OTM	5,25,30,80	47.0(16.5)/45.0(11.3)	0.9985/0.9631	26.69*/17.53*
5	1.5T, Pval	5,25,40,70,80	46.9(9.3)	0.9943	2.69*
	3.0T, Pval	0.5,5,30,40,50	45.1(5.0)	0.9897	30.23
	OTM	0.5,10,30,50,80	46.8(12.0)/45.2(15.2)	0.9495/0.9167	84.41/9.63*
6	1.5T, Pval	0.5,20,25,30,40,60	46.9(11.3)	0.9991	12.81
	3.0T, Pval	0.5,10,30,40,50,60	45.1(10.3)	0.9833	7.38*
	OTM	0.5,5,25,40,70,80	46.9(9.6)/45.2 (8.4)	0.9873/0.9177	4.90*/14.56
7	1.5T, Pval	0.5,10,15,20,50,60,80	46.9(11.8)	0.9966	21.73
	3.0T, Pval	0.5,15,25,50,60,70,80	45.1(14.0)	0.9984	28.00
	OTM	0.5,5,15,25,40,70,80	46.9(8.1)/45.0 (10.5)	0.9922/0.9704	3.02*/21.25*
8	1.5T, Pval	5,10,20,25,50,60,70,80	46.9(7.7)	0.9980	2.21*
	3.0T, Pval	0.5,5,10,20,25,30,40,50	45.1(17.2)	0.9930	52.07
	OTM	0.5,5,10,20,30,60,70,80	47.0(9.3)/45.0(6.9)	0.9622/0.9435	2.74/6.73*
9	1.5T, Pval	5,10,15,20,25,40,50,70,80	46.9(10.0)	0.9935	6.80
	3.0T, Pval	0.5,5,10,15,30,40,50,70,80	45.1(11.3)	0.9888	3.56
	OTM	0.5,5,15,20,30,40,50,70,80	46.6(8.2)/45.0(9.3)	0.9857/0.9842	5.39*/1.29*
10	1.5T, Pval	0.5,5,10,15,20,25,30,50,60,80	46.9(9.1)	1.0000	2.74*
	3.0T, Pval	0.5,5,10,15,20,25,40,50,70,80	45.1(9.0)	0.9940	1.50*
	OTM	0.5,5,20,25,30,40,50,60,70,80	46.8(9.1)/45.2 (8.2)	0.9673/0.9142	4.21/3.87
11	1.5T, Pval	0.5,5,10,20,25,30,40,50,60,70,80	46.9(7.8)	0.9838	0.62*
	3.0T, Pval	0.5,5,10,15,20,25,30,50,60,70,80	45.1(10.7)	0.9661	2.94
	OTM	0.5,5,10,20,25,30,40,50,60,70,80	46.9(7.8)/45.1(8.3)	0.8879/0.9211	0.62*/0.18*
12	1.5T	0.5,5,10,15,20,25,30,40,50,60,70,80	46.9 (7.6)	1.0000	0.00
	3.0T	0.5,5,10,15,20,25,30,40,50,60,70,80	45.1 (8.4)	1.0000	0.00

Abbreviations: Pval= highest scoring pval for each system for each number of spin-locks, OTM=the optimal trans-magnetic spin-lock combinations, with the various values found on 1.5T/3.0T.

Table B-3. The summary for the best phantom spin-lock combinations based on pval for 3.0T and 1.5T.

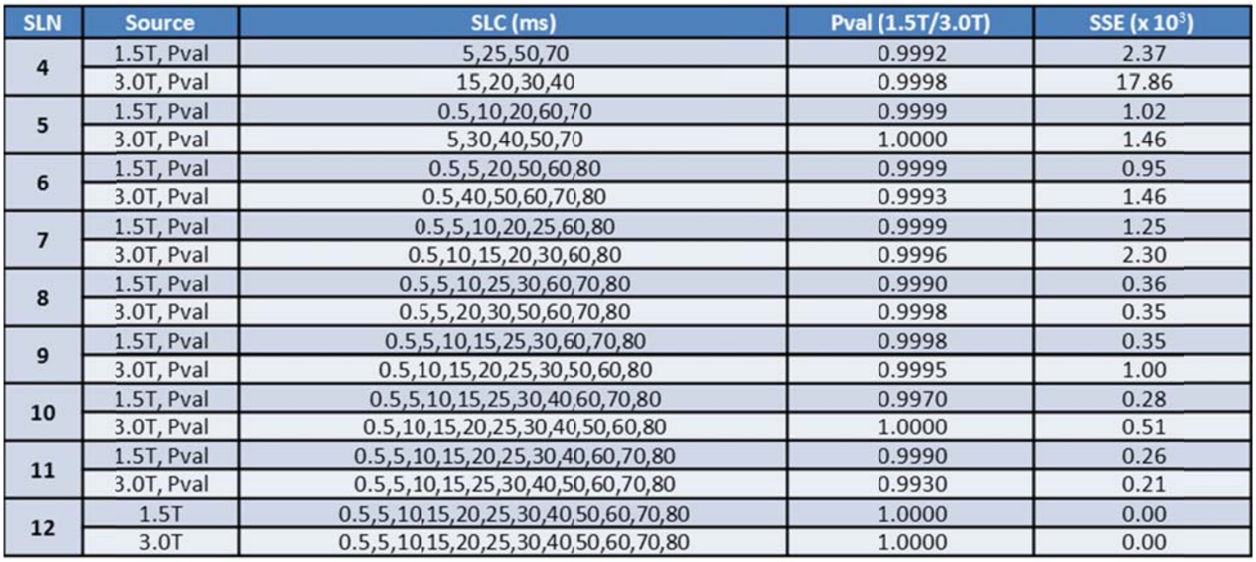

SLN	Source	SLC (ms)	Pval (1.5T/3.0T)	SSE (x 10^3)
4	1.5T, Pval	5,25,50,70	0.9992	2.37
	3.0T, Pval	15,20,30,40	0.9998	17.86
5	1.5T, Pval	0.5,10,20,60,70	0.9999	1.02
	3.0T, Pval	5,30,40,50,70	1.0000	1.46
6	1.5T, Pval	0.5,5,20,50,60,80	0.9999	0.95
	3.0T, Pval	0.5,40,50,60,70,80	0.9993	1.46
7	1.5T, Pval	0.5,5,10,20,25,60,80	0.9999	1.25
	3.0T, Pval	0.5,10,15,20,30,60,80	0.9996	2.30
8	1.5T, Pval	0.5,5,10,25,30,60,70,80	0.9990	0.36
	3.0T, Pval	0.5,5,20,30,50,60,70,80	0.9998	0.35
9	1.5T, Pval	0.5,5,10,15,25,30,60,70,80	0.9998	0.35
	3.0T, Pval	0.5,10,15,20,25,30,50,60,80	0.9995	1.00
10	1.5T, Pval	0.5,5,10,15,25,30,40,60,70,80	0.9970	0.28
	3.0T, Pval	0.5,10,15,20,25,30,40,50,60,80	1.0000	0.51
11	1.5T, Pval	0.5,5,10,15,20,25,30,40,60,70,80	0.9990	0.26
	3.0T, Pval	0.5,5,10,15,25,30,40,50,60,70,80	0.9930	0.21
12	1.5T	0.5,5,10,15,20,25,30,40,50,60,70,80	1.0000	0.00
	3.0T	0.5,5,10,15,20,25,30,40,50,60,70,80	1.0000	0.00

Table B-4. Mean and standard deviation of the relaxation times found for the optimal spin-lock spacing experiment, which compared linear and exponential spacing in a phantom.

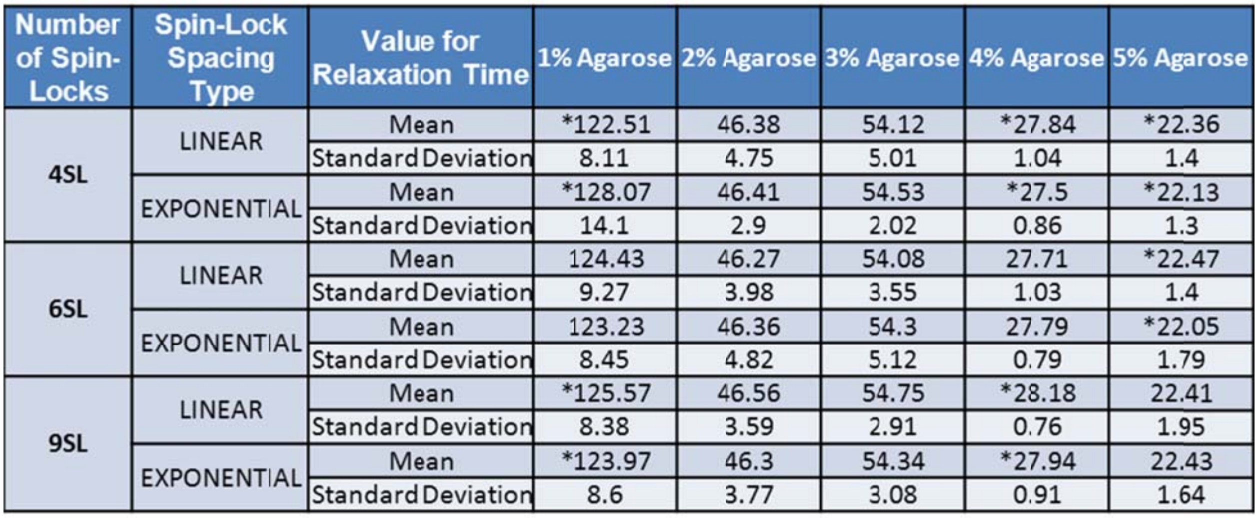

Number of Spin-Locks	Spin-Lock Spacing Type	Value for Relaxation Time	1% Agarose	2% Agarose	3% Agarose	4% Agarose	5% Agarose
4SL	LINEAR	Mean	*122.51	46.38	54.12	*27.84	*22.36
		Standard Deviation	8.11	4.75	5.01	1.04	1.4
	EXPONENTIAL	Mean	*128.07	46.41	54.53	*27.5	*22.13
		Standard Deviation	14.1	2.9	2.02	0.86	1.3
6SL	LINEAR	Mean	124.43	46.27	54.08	27.71	*22.47
		Standard Deviation	9.27	3.98	3.55	1.03	1.4
	EXPONENTIAL	Mean	123.23	46.36	54.3	27.79	*22.05
		Standard Deviation	8.45	4.82	5.12	0.79	1.79
9SL	LINEAR	Mean	*125.57	46.56	54.75	*28.18	22.41
		Standard Deviation	8.38	3.59	2.91	0.76	1.95
	EXPONENTIAL	Mean	*123.97	46.3	54.34	*27.94	22.43
		Standard Deviation	8.6	3.77	3.08	0.91	1.64

Note: *=significant difference in relaxation times based on student t-test between linear and exponential spacing.

APPENDIX C: AUXILIARY DATA COLLECTED IN CHAPTER 4

Table C-1. Inter-user variability of selecting anterior and posterior sulcus boundary cutoffs and the resulting posterior ridge.

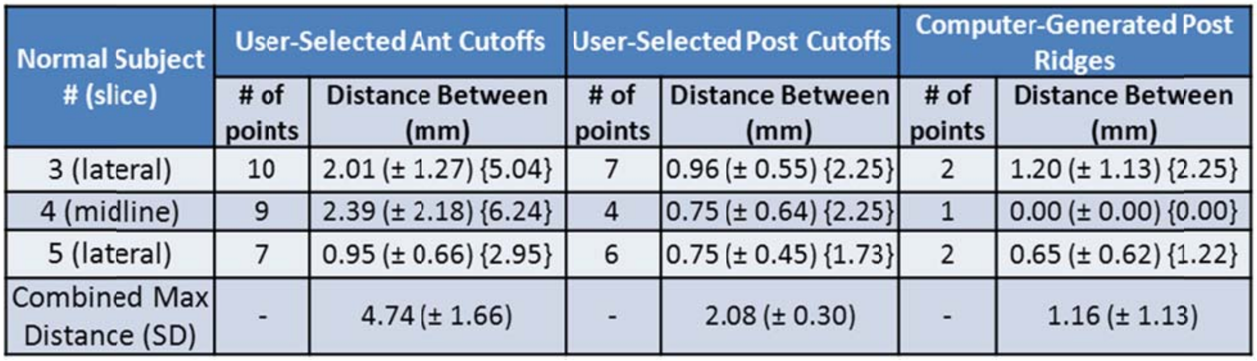

Normal Subject # (slice)	User-Selected Ant Cutoffs		User-Selected Post Cutoffs		Computer-Generated Post Ridges	
	# of points	Distance Between (mm)	# of points	Distance Between (mm)	# of points	Distance Between (mm)
3 (lateral)	10	2.01 (± 1.27) {5.04}	7	0.96 (± 0.55) {2.25}	2	1.20 (± 1.13) {2.25}
4 (midline)	9	2.39 (± 2.18) {6.24}	4	0.75 (± 0.64) {2.25}	1	0.00 (± 0.00) {0.00}
5 (lateral)	7	0.95 (± 0.66) {2.95}	6	0.75 (± 0.45) {1.73}	2	0.65 (± 0.62) {1.22}
Combined Max Distance (SD)	-	4.74 (± 1.66)	-	2.08 (± 0.30)	-	1.16 (± 1.13)

For the distances reported, the average distance (± one standard deviation) and {maximum} distance are reported from each of the twelve trials in mm.

Table C-2. Differences between distances of bone-cartilage interface points between the three different profiles found from the different imaging sessions for both the midline and lateral slices through the normal subjects' lateral femoral condyle.

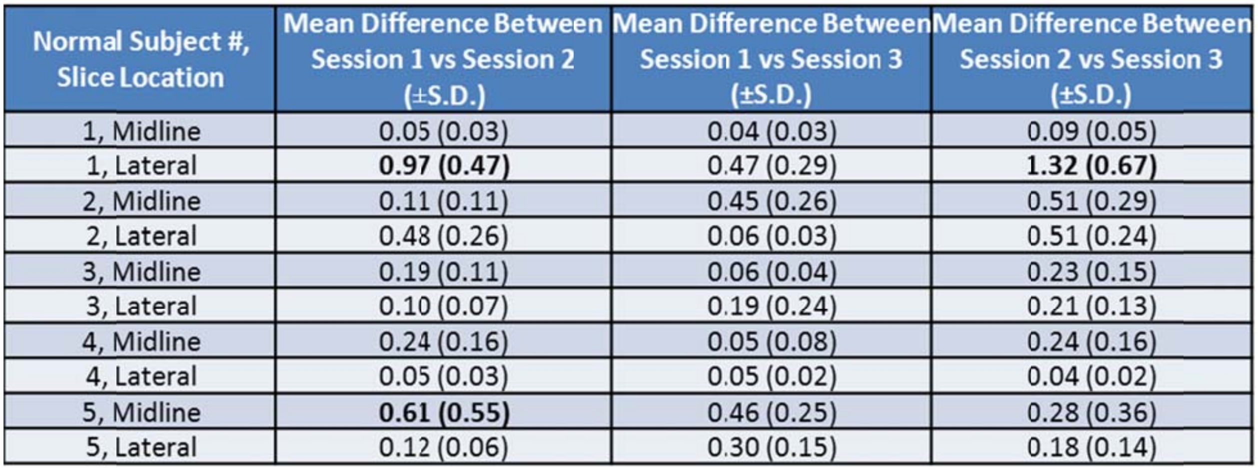

Normal Subject #, Slice Location	Mean Difference Between Session 1 vs Session 2 (±S.D.)	Mean Difference Between Session 1 vs Session 3 (±S.D.)	Mean Difference Between Session 2 vs Session 3 (±S.D.)
1, Midline	0.05 (0.03)	0.04 (0.03)	0.09 (0.05)
1, Lateral	**0.97 (0.47)**	0.47 (0.29)	**1.32 (0.67)**
2, Midline	0.11 (0.11)	0.45 (0.26)	0.51 (0.29)
2, Lateral	0.48 (0.26)	0.06 (0.03)	0.51 (0.24)
3, Midline	0.19 (0.11)	0.06 (0.04)	0.23 (0.15)
3, Lateral	0.10 (0.07)	0.19 (0.24)	0.21 (0.13)
4, Midline	0.24 (0.16)	0.05 (0.08)	0.24 (0.16)
4, Lateral	0.05 (0.03)	0.05 (0.02)	0.04 (0.02)
5, Midline	**0.61 (0.55)**	0.46 (0.25)	0.28 (0.36)
5, Lateral	0.12 (0.06)	0.30 (0.15)	0.18 (0.14)

Note: Bolded highlights average distance differences to be greater than one voxel width.

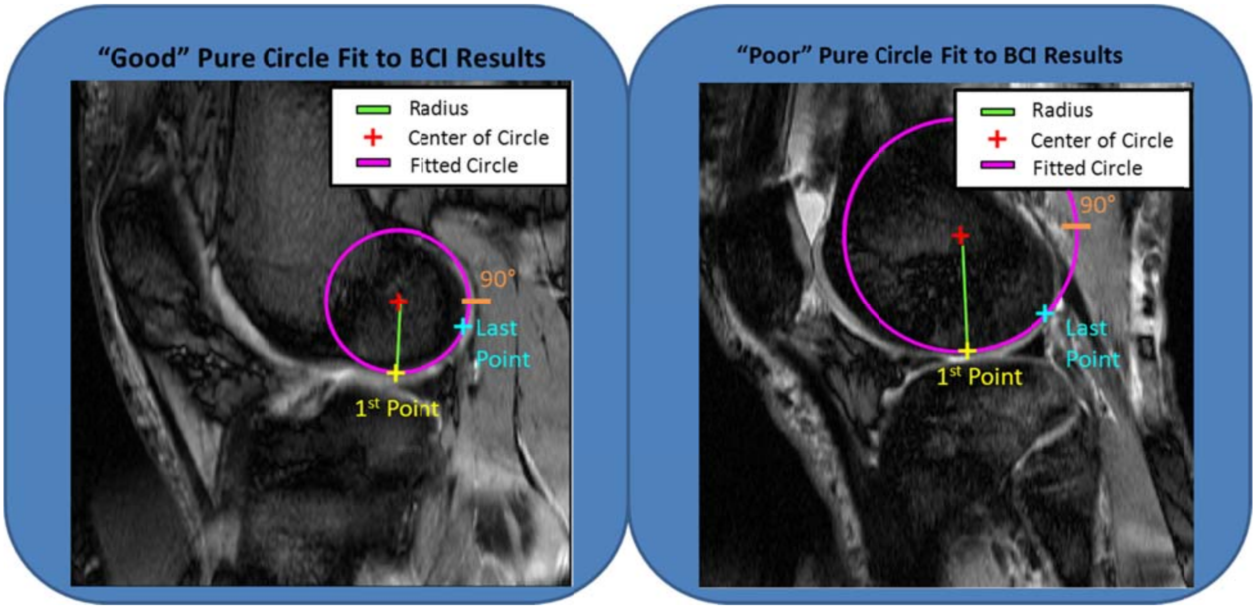

Figure C-1. This shows an example of "good" circular fit (left panel) with a knee that is a much rounder curvature between the two points (yellow, blue; note size of approximate purple circle and yellow center location) in comparison to a "poor" purely circular fit in a larger knee (right panel). The curvilinear distance between the two points (yellow, blue) is the same (30mm), but in a knee which is a little larger (right), not enough of the entire condyle's geometry is accounted for by this distance when fit with a circle. This subsequently places the location of the center (red, right image) much too high to fully capture data from 0-90° within the cartilage (as shown by the orange mark where other tissue like the bursa would be sampled), and may be a poorer approximate center of rotation than the knee on the left. Hence the derivation of the condyle-specific radius (as determined as the average of the anterior-posterior and proximal-distal axes in Figure 23) to restrain the polar coordinate system to the knee size, instead of just a purely circular fit based on a constant curvilinear distance about the periphery of the condyle.

APPENDIX D: AUXILIARY DATA COLLECTED IN CHAPTER 5 AND 6

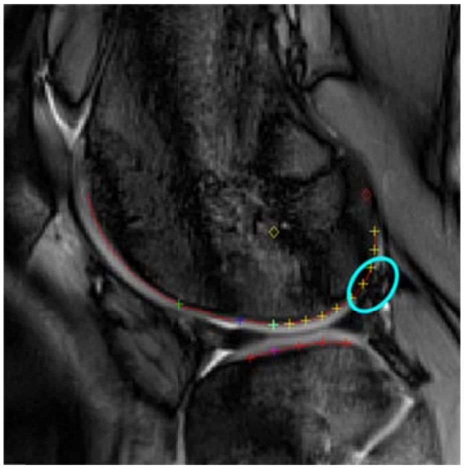

Figure D-1. Normal 7's coordinate system (resulting from line profile analysis) serves as an example for data selection. Once line profile measurements were made from 0° (first yellow cross-hair) to 90° (last yellow cross-hair) posteriorly of the posterior ridge (cyan cross-hair) in 10° increments, the 20ms SL images were double-checked for any obvious erroneous tissue signal. In this case, another tissue (dark portion, circled in cyan) is interfering with the cartilage signal from 50-70°, and was excluded.

Table D-1. Portions of subjects' line profiles which were rejected from further analysis and why.

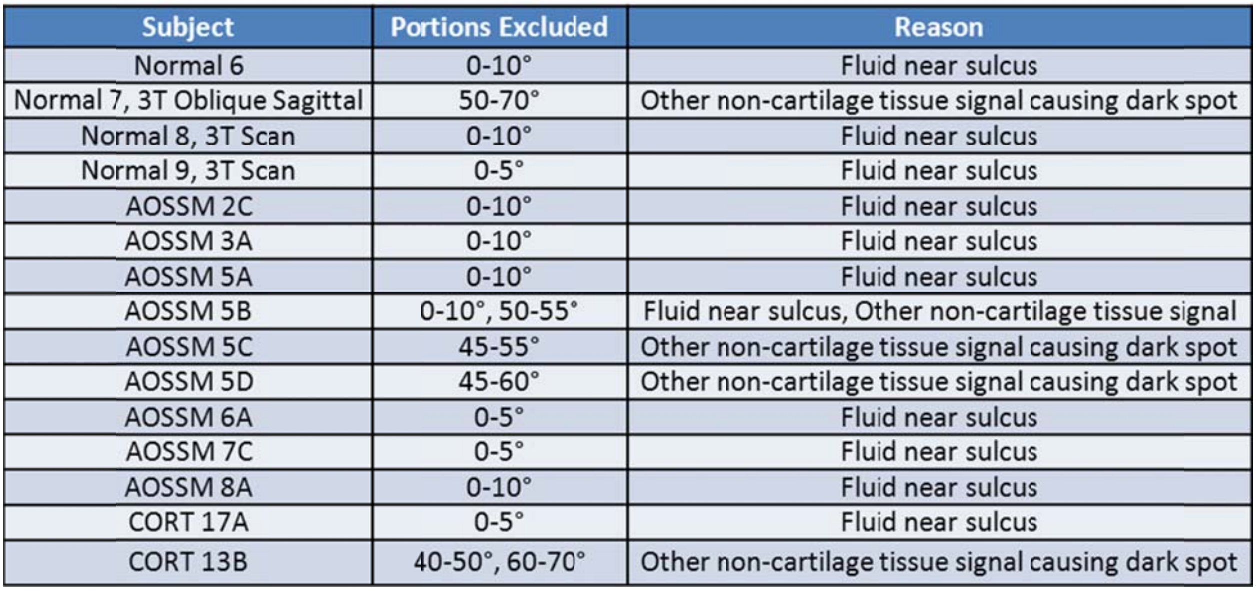

Subject	Portions Excluded	Reason
Normal 6	0-10°	Fluid near sulcus
Normal 7, 3T Oblique Sagittal	50-70°	Other non-cartilage tissue signal causing dark spot
Normal 8, 3T Scan	0-10°	Fluid near sulcus
Normal 9, 3T Scan	0-5°	Fluid near sulcus
AOSSM 2C	0-10°	Fluid near sulcus
AOSSM 3A	0-10°	Fluid near sulcus
AOSSM 5A	0-10°	Fluid near sulcus
AOSSM 5B	0-10°, 50-55°	Fluid near sulcus, Other non-cartilage tissue signal
AOSSM 5C	45-55°	Other non-cartilage tissue signal causing dark spot
AOSSM 5D	45-60°	Other non-cartilage tissue signal causing dark spot
AOSSM 6A	0-5°	Fluid near sulcus
AOSSM 7C	0-5°	Fluid near sulcus
AOSSM 8A	0-10°	Fluid near sulcus
CORT 17A	0-5°	Fluid near sulcus
CORT 13B	40-50°, 60-70°	Other non-cartilage tissue signal causing dark spot

Table D-2. Group 1's healthy and injured cartilage relaxation behaviors as reported by layer.

Subject	Layer	Average Relaxation Time (± Std. Dev.) (ms)	Fraction Above Hot Spot Threshold	pval for Normal Similarity
Composite Normal Data	Deep	43.75 (15.17)	-	-
	Radial	45.95 (9.98)	-	-
	Transitional	46.89 (8.64)	-	-
AOSSM 2	**Deep**	37.37 (9.53)	0.00	0.000
	Radial	49.03 (12.89)	0.31	0.007
	Transitional	56.56 (15.58)	0.35	0.000
AOSSM 3	**Deep**	60.88 (18.68)	0.43	0.000
	Radial	54.47 (15.97)	0.30	0.000
	Transitional	51.09 (16.38)	0.21	0.000
AOSSM 4	**Deep**	82.41 (34.31)	0.33	0.000
	Radial	90.19 (33.38)	0.33	0.000
	Transitional	75.7 (22.34)	0.30	0.000
AOSSM 5	Deep	46.14 (7.74)	0.09	0.165
	Radial	44.17(5.34)	0.03	0.115
	Transitional	42.9 (5.94)	0.01	0.000
AOSSM 6	**Deep**	68.19 (17.65)	0.64	0.000
	Radial	62.82 (13.99)	0.67	0.000
	Transitonal	53.4 (9.94)	0.41	0.000
AOSSM 7	**Deep**	35.30 (3.5)	0.00	0.000
	Radial	44.46 (4.66)	0.00	0.176
	Transitional	53.02 (10.92)	0.23	0.000
AOSSM 8	Deep	42.59 (7.04)	0.00	0.497
	Radial	45.68 (6.44)	0.11	0.813
	Transitional	46.32 (4.46)	0.03	0.557
AOSSM 9	**Deep**	55.82 (18.42)	0.40	0.000
	Radial	54.63 (10.61)	0.34	0.000
	Transitional	48.14 (9.03)	0.10	0.195
CORT 1	**Deep**	57.33 (9.83)	0.41	0.000
	Radial	58.68 (12.01)	0.51	0.000
	Transitional	50.64 (9.78)	0.34	0.000
CORT 2	Deep	46.03 (9.25)	0.10	0.161
	Radial	50.85 (7.96)	0.32	0.000
	Transitional	55.21 (11.13)	0.43	0.000
CORT 3	Deep	42.08 (10.04)	0.07	0.315
	Radial	47.58 (8.88)	0.17	0.144
	Transitional	50.97 (8.36)	0.29	0.000
CORT 4	**Deep**	56.86 (28.39)	0.31	0.000
	Radial	54.16 (17.22)	0.32	0.000
	Transitional	51.18 (11.64)	0.31	0.000

Table D-3. Group 2's healthy and injured cartilage relaxation behaviors as reported layer.

Subject	Layer	Average Relaxation Time (± Std. Dev.) (ms)	Fraction Above Hot Spot Threshold	pval for Normal Similarity
Composite Normal Data	Deep	41.56 (8.41)	-	-
	Radial	45.22 (7.41)	-	-
	Transitional	47.63 (8.83)	-	-
AOSSM 1	**Deep**	54.40 (13.65)	0.57	0.000
	Radial	55.86 (14.85)	0.51	0.000
	Transitional	56.40 (22.58)	0.33	0.000
CORT 5*	Deep	33.24 (4.35)	0.00	0.000
	Radial	34.65 (5.1)	0.00	0.000
	Transitional	35.80 (4.89)	0.00	0.000
CORT 7	**Deep**	93.72 (23.83)	0.90	0.000
	Radial	112.87 (29.57)	0.90	0.000
	Transitional	107.04 (29.19)	0.85	0.000
CORT 8	**Deep**	87.63 (22.93)	0.55	0.000
	Radial	95.62 (15.99)	0.55	0.000
	Transitional	89.54 (21.07)	0.52	0.000
CORT 9	Deep	43.30 (9.06)	0.20	0.063
	Radial	47.38 (7.66)	0.16	0.009
	Transitional	51.29 (6.00)	0.24	0.000
CORT 10	**Deep**	47.89 (10.9)	0.31	0.000
	Radial	54.87 (8.68)	0.51	0.000
	Transitional	56.82 (9.56)	0.41	0.000
CORT 13	**Deep**	50.66 (14.36)	0.42	0.000
	Radial	56.48 (11.96)	0.60	0.000
	Transitional	54.62 (12.97)	0.41	0.000
CORT 14	**Deep**	43.60 (6.02)	0.13	0.025
	Radial	47.61 (3.98)	0.12	0.002
	Transitional	58.71 (16.34)	0.25	0.000
CORT 15	**Deep**	49.18 (8.60)	0.41	0.000
	Radial	52.43 (9.07)	0.46	0.000
	Transitional	75.43 (32.95)	0.52	0.000
CORT 16	**Deep**	55.83 (15.97)	0.58	0.000
	Radial	60.17 (17.80)	0.68	0.000
	Transitional	58.93 (15.25)	0.55	0.000
CORT 17	Deep*	37.54 (4.13)	0.00	0.000
	Radial	50.55 (8.27)	0.32	0.000
	Transitional	61.11 (13.94)	0.56	0.000
CORT 18	**Deep**	51.8 (9.96)	0.52	0.000
	Radial	47.10 (8.38)	0.33	0.023
	Transitional	45.66 (7.18)	0.11	0.040

Note: *=significantly lower than normal cartilage

Table D-4. Deep cartilage layer's average relaxation times for each patient with a follow-up history, as well as the pval for normal similarity and fractions of the condyle's which were affected by hot spots.

ACL Patient	Imaging Session	Average Relaxation Time (± Std.Dev.) (ms)	Total Fraction Above Hot Spot Threshold	Fraction Above Hot Spot Threshold that was same as Pre-Op	Pval for Normal Similarity
AOSSM 1	Pre-Op	54.40 (13.65)	0.56	-	0.000
	4 Mo. Post	58.66 (24.68)	0.26	0.32	0.000
AOSSM 2	Pre-Op	37.37 (9.53)	0.01	-	0.000
	4 Mo. Post	48.24 (12.33)	0.00	1.00	0.007
	8 Mo. Post	50.64 (13.50)	0.00	1.00	0.000
	12 Mo. Post	39.61 (6.46)	0.00	0.00	0.010
AOSSM 3	Pre-Op	60.88(18.68)	0.34	-	0.000
	4 Mo. Post	61.36 (34.58)	0.30	0.56	0.000
AOSSM 5	**Pre-Op**	46.14 (7.74)	0.07	-	0.165
	4 Mo. Post	38.02 (6.06)	0.00	0.00	0.001
	8 Mo. Post	35.52 (10.48)	0.00	0.00	0.000
	12 Mo. Post	39.77 (16.20)	0.04	0.29	0.030
AOSSM 6	Pre-Op	68.19 (17.65)	0.59	-	0.000
	4 Mo. Post	49.67 (12.00)	0.24	0.41	0.000
	8 Mo. Post	35.72 (7.45)	0.00	0.00	0.000
AOSSM 7	Pre-Op	35.30 (3.5)	0.00	-	0.000
	4 Mo. Post	54.45 (10.29)	0.33	NA	0.000
	8 Mo. Post	39.69 (8.75)	0.00	0.00	0.016
AOSSM 8	**Pre-Op**	42.59 (7.04)	0.00	-	0.497
	8 Mo. Post	66.23 (28.89)	0.56	NA	0.000
CORT 5	Pre-Op	33.24 (4.35)	0.00	-	0.000
	4 Mo. Post	51.96 (21.26)	0.21	NA	0.000
CORT 6	4 Mo. Post	65.66 (18.22)	0.81	NA	0.000
CORT 8	Pre-Op	87.63 (22.93)	0.54	-	0.000
	4 Mo. Post	58.12 (16.93)	0.64	0.37	0.000
CORT 9	**Pre-Op**	43.30 (9.06)	0.20	-	0.063
	4 Mo. Post	58.86 (25.92)	0.45	1.00	0.000
CORT 11	4 Mo. Post	44.82 (7.62)	0.21	NA	0.000
CORT 13	Pre-Op	50.66 (14.36)	0.41	-	0.000
	4 Mo. Post	37.58 (8.29)	0.03	0.07	0.000
CORT 15	Pre-Op	49.18 (8.60)	0.38	-	0.000
	4 Mo. Post	51.35 (10.43)	0.49	0.58	0.000

Table D-5. Radial cartilage layer’s average relaxation times for each patient with a follow-up history, as well as the pval for normal similarity and fractions of the condyle’s which were affected by hot spots.

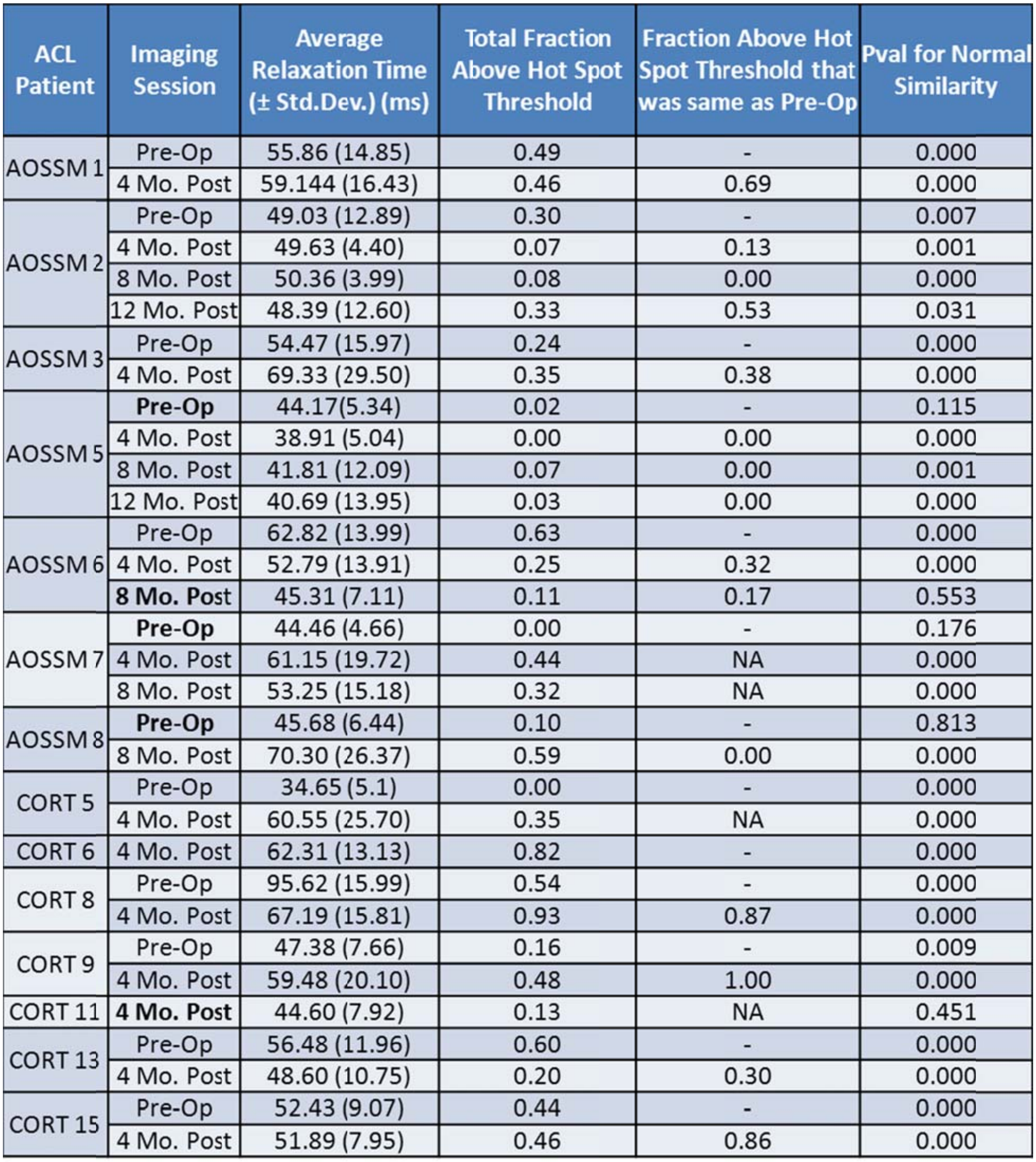

ACL Patient	Imaging Session	Average Relaxation Time (± Std.Dev.) (ms)	Total Fraction Above Hot Spot Threshold	Fraction Above Hot Spot Threshold that was same as Pre-Op	Pval for Normal Similarity
AOSSM 1	Pre-Op	55.86 (14.85)	0.49	-	0.000
	4 Mo. Post	59.144 (16.43)	0.46	0.69	0.000
AOSSM 2	Pre-Op	49.03 (12.89)	0.30	-	0.007
	4 Mo. Post	49.63 (4.40)	0.07	0.13	0.001
	8 Mo. Post	50.36 (3.99)	0.08	0.00	0.000
	12 Mo. Post	48.39 (12.60)	0.33	0.53	0.031
AOSSM 3	Pre-Op	54.47 (15.97)	0.24	-	0.000
	4 Mo. Post	69.33 (29.50)	0.35	0.38	0.000
AOSSM 5	**Pre-Op**	44.17(5.34)	0.02	-	0.115
	4 Mo. Post	38.91 (5.04)	0.00	0.00	0.000
	8 Mo. Post	41.81 (12.09)	0.07	0.00	0.001
	12 Mo. Post	40.69 (13.95)	0.03	0.00	0.000
AOSSM 6	Pre-Op	62.82 (13.99)	0.63	-	0.000
	4 Mo. Post	52.79 (13.91)	0.25	0.32	0.000
	8 Mo. Post	45.31 (7.11)	0.11	0.17	0.553
AOSSM 7	**Pre-Op**	44.46 (4.66)	0.00	-	0.176
	4 Mo. Post	61.15 (19.72)	0.44	NA	0.000
	8 Mo. Post	53.25 (15.18)	0.32	NA	0.000
AOSSM 8	**Pre-Op**	45.68 (6.44)	0.10	-	0.813
	8 Mo. Post	70.30 (26.37)	0.59	0.00	0.000
CORT 5	Pre-Op	34.65 (5.1)	0.00	-	0.000
	4 Mo. Post	60.55 (25.70)	0.35	NA	0.000
CORT 6	4 Mo. Post	62.31 (13.13)	0.82	-	0.000
CORT 8	Pre-Op	95.62 (15.99)	0.54	-	0.000
	4 Mo. Post	67.19 (15.81)	0.93	0.87	0.000
CORT 9	Pre-Op	47.38 (7.66)	0.16	-	0.009
	4 Mo. Post	59.48 (20.10)	0.48	1.00	0.000
CORT 11	**4 Mo. Post**	44.60 (7.92)	0.13	NA	0.451
CORT 13	Pre-Op	56.48 (11.96)	0.60	-	0.000
	4 Mo. Post	48.60 (10.75)	0.20	0.30	0.000
CORT 15	Pre-Op	52.43 (9.07)	0.44	-	0.000
	4 Mo. Post	51.89 (7.95)	0.46	0.86	0.000

Table D-6. Transitional cartilage layer's average relaxation times for each patient with a follow-up history, as well as the pval for normal similarity and fractions of the condyle's which were affected by hot spots.

ACL Patient	Imaging Session	Average Relaxation Time (± Std.Dev.) (ms)	Total Fraction Above Hot Spot Threshold	Fraction Above Hot Spot Threshold that was same as Pre-Op	Pval for Normal Similarity
AOSSM 1	Pre-Op	56.40 (22.58)	0.32	-	0.000
	4 Mo. Post	52.39 (11.14)	0.38	0.59	0.000
AOSSM 2	Pre-Op	56.56 (15.58)	0.32	-	0.000
	4 Mo. Post	51.63 (14.03)	0.32	0.28	0.000
	8 Mo. Post	48.73 (7.59)	0.18	0.09	0.080
	12 Mo. Post	50.36 (11.74)	0.20	0.22	0.000
AOSSM 3	Pre-Op	51.09 (16.38)	0.16	-	0.000
	4 Mo. Post	58.74 (27.13)	0.37	0.25	0.000
AOSSM 5	Pre-Op	42.9 (5.94)	0.00	-	0.000
	4 Mo. Post	41.34 (4.52)	0.00	NA	0.000
	8 Mo. Post	49.00 (19.15)	0.11	NA	0.069
	12 Mo. Post	44.27 (10.96)	0.07	NA	0.014
AOSSM 6	Pre-Op	53.4 (9.94)	0.38	-	0.000
	4 Mo. Post	48.08 (12.29)	0.07	0.00	0.000
	8 Mo. Post	46.45 (8.67)	0.13	0.34	0.644
AOSSM 7	Pre-Op	53.02 (10.92)	0.21	-	0.000
	4 Mo. Post	63.35 (23.72)	0.38	0.95	0.000
	8 Mo. Post	60.80 (18.22)	0.34	0.67	0.000
AOSSM 8	**Pre-Op**	46.32 (4.46)	0.02	-	0.557
	8 Mo. Post	63.01 (18.01)	0.57	0.00	0.000
CORT 5	Pre-Op	35.80 (4.89)	0.00	-	0.000
	4 Mo. Post	69.11 (18.85)	0.80	NA	0.000
CORT 6	4 Mo. Post	63.73 (26.1)	0.44	NA	0.000
CORT 8	Pre-Op	89.54 (21.07)	0.51	-	0.000
	4 Mo. Post	74.46 (20.75)	0.93	0.96	0.000
CORT 9	Pre-Op	51.29 (6.00)	0.24	-	0.000
	4 Mo. Post	58.52 (12.38)	0.49	0.54	0.000
CORT 11	4 Mo. Post	52.22 (12.63)	0.32	NA	0.000
CORT 13	Pre-Op	54.62 (12.97)	0.40	-	0.000
	4 Mo. Post	57.52 (14.60)	0.31	0.30	0.000
CORT 15	Pre-Op	75.43 (32.95)	0.49	-	0.000
	4 Mo. Post	53.52 (14.30)	0.36	0.29	0.000

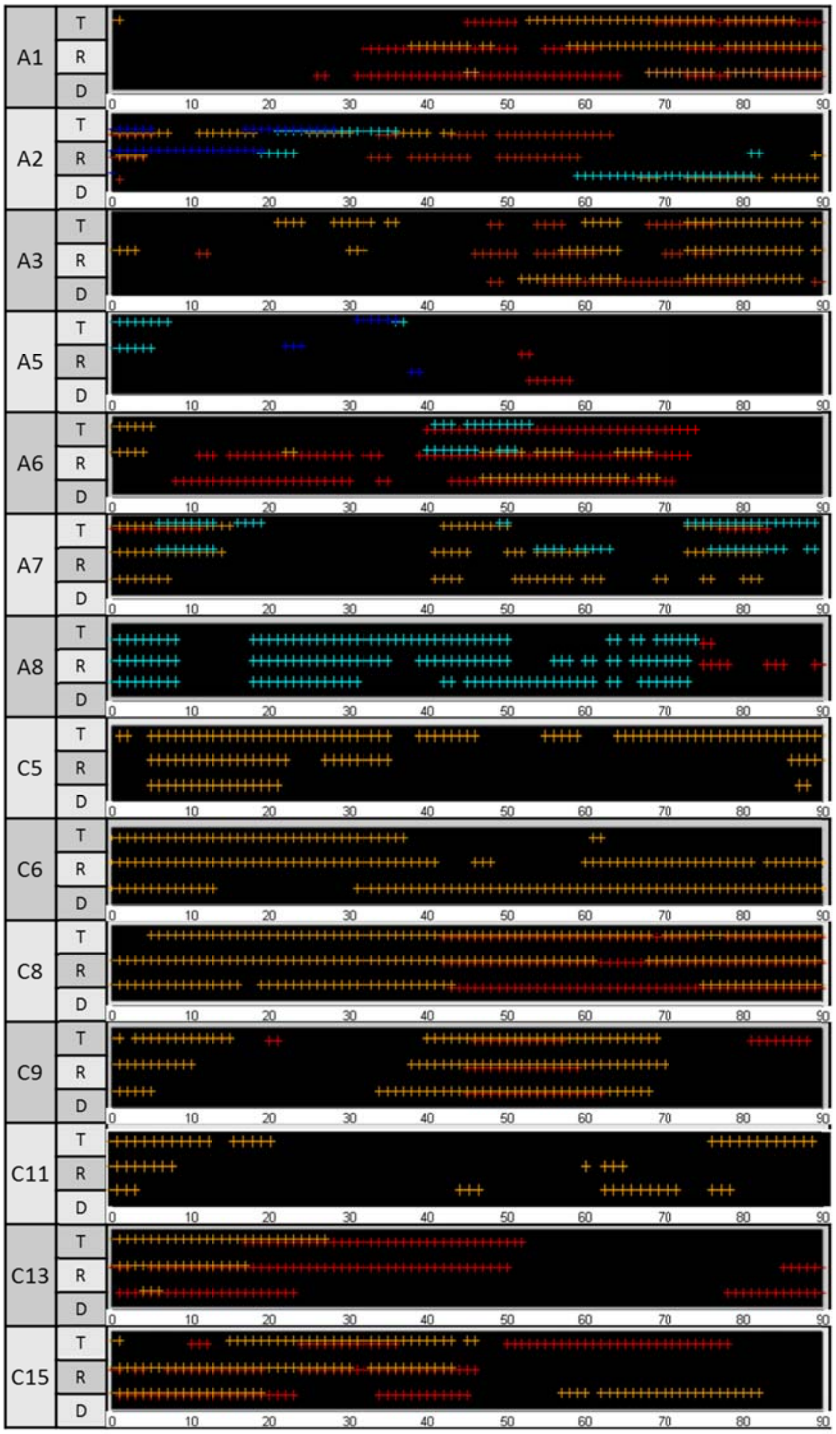

Figure D-2. Locations of hot spots (+) over time for each of the patients who had follow-up T1rho images collected as reported for the deep (D), radial (R), and transitional (T) zones along 0-90° from the posterior ridge. These AOSSM (A) and CORT (C) patients had pre-surgery (red), 4 month (orange), 8 month (cyan), and 12 month (blue) post-surgery images collected. This visualization allows for tracking the severity of potential cartilage trauma over time (by color) and the depth (by layers).

Table D-7. The average 3.0T to 1.5T ratios for Relative-Contrast, Contrast-to-Noise Ratio, and Signal-Difference-to-Noise-Ratio.

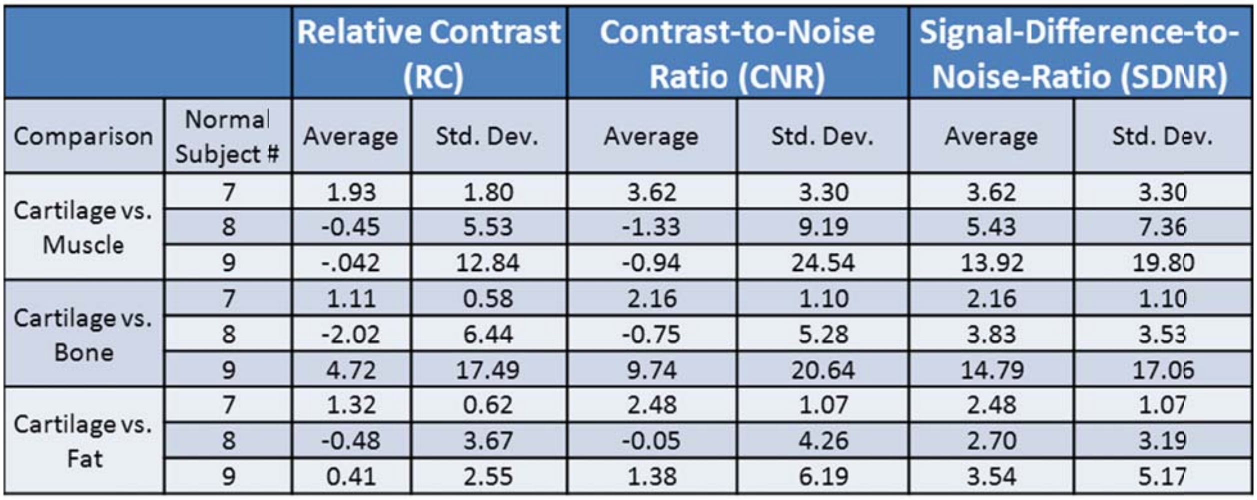

		Relative Contrast (RC)		Contrast-to-Noise Ratio (CNR)		Signal-Difference-to-Noise-Ratio (SDNR)	
Comparison	Normal Subject #	Average	Std. Dev.	Average	Std. Dev.	Average	Std. Dev.
Cartilage vs. Muscle	7	1.93	1.80	3.62	3.30	3.62	3.30
	8	-0.45	5.53	-1.33	9.19	5.43	7.36
	9	-.042	12.84	-0.94	24.54	13.92	19.80
Cartilage vs. Bone	7	1.11	0.58	2.16	1.10	2.16	1.10
	8	-2.02	6.44	-0.75	5.28	3.83	3.53
	9	4.72	17.49	9.74	20.64	14.79	17.06
Cartilage vs. Fat	7	1.32	0.62	2.48	1.07	2.48	1.07
	8	-0.48	3.67	-0.05	4.26	2.70	3.19
	9	0.41	2.55	1.38	6.19	3.54	5.17

REFERENCES

1. Brown, T.D., Johnston, R.C., Saltzman, C.L., Marsh, J.L., Buckwalter, J.A, *Posttraumatic osteoarthritis: a first estimate of incidence, prevalence, and burden of disease.* J Orthop Trauma, 2006. **20**(10): p. 739-44.

2. May 2011[cited 2011 May 14]. https://www.cia.gov/library/publications/the-world-factbook/geos/us.html.

3. Regatte, R.R., Akella, S.V., Lonner, J.H., Kneeland, J.B., Reddy, R., *T1rho relaxation mapping in human osteoarthritis (OA) cartilage: comparison of T1rho with T2.* J Magn Reson Imaging, 2006. **23**(4): p. 547-53.

4. Roos, H., Adalberth, T., Dahlberg, L., Lohmander, L.S., *Osteoarthritis of the knee after injury to the anterior cruciate ligament or meniscus: the influence of time and age.* Osteoarthritis Cartilage/ OARS, Osteoarthritis Research Society, 1995. **3**(4): p. 261-7.

5. Boden, B.P., Sheehan, F. T., Torg, J.S., Hewett, T.E., *Noncontact anterior cruciate ligament injuries: mechanisms and risk factors.* J Am Acad Orthop Surg, 2010. **18**(9): p. 520-7.

6. 2011 [cited 2011 April 13]; http://www.emrf.org/

7. Prince, J.L. and J.M. Links, *Medical imaging signals and systems* 2006, Upper Saddle River, NJ: Pearson Prentice Hall.

8. Duvvuri, U., Kudchodkar, S., Reddy, R., Leigh, J.S., *T(1rho) relaxation can assess longitudinal proteoglycan loss from articular cartilage in vitro.* Osteoarthritis Cartilage, 2002. **10**(11): p. 838-44.

9. Bernstein, J., editor, *Musculoskeletal medicine*. 1st ed 2003, Rosemont, Ill.: American Academy of Orthopaedic Surgeons. xxiv, 490 p., 44 p. of plates.

10. Blackburn, T.A. and E. Craig, *Knee anatomy: a brief review.* Phys Ther, 1980. **60**(12): p. 1556-60.

11. Tortora, G.J., *Principles of human anatomy*. 9th ed 2002, New York: John Wiley & Sons. xxviii, 918 p.

12. Fu, F.H., Harner, C.D., Johnson, D.L., Miller, M.D., Woo, S.L.Y., *Biomechanics of Knee Ligaments - Basic Concepts and Clinical-Application.* J Bone Joint Surg Am, 1993. **75A**(11): p. 1716-1727.

13. Temple, M.M., Bae, W.C., Chen, M.Q., Lotz, M., Amiel, D., Coutts, R.D., Sah, R.L., *Age- and site-associated biomechanical weakening of human articular cartilage of the femoral condyle.* Osteoarthritis and cartilage, 2007. **15**(9): p. 1042-52.

14. DeMorat, G., Weinhold, P., Blackburn, T., Chudik, S., Garrett, W., *Aggressive quadriceps loading can induce noncontact anterior cruciate ligament injury.* Am J Sports Med, 2004. **32**(2): p. 477-83.

15. Griffin, L.Y., Agel, J., Albohm, M.J., Arendt, E.A., Dick, R.W., Garrett, W.E., Garrick, J.G., Hewett, T.E., Huston, L., Ireland, M.L., Johnson, R.J., Kibler, W.B., Lephart, S., Lewis, J.L., Lindenfield, T.N., Mandelbaum, B.R., Marchak, P., Teitz, C.C., Wojtys, E.M., *Noncontact anterior cruciate ligament injuries: risk factors and prevention strategies.* J Am Acad Orthop Surg, 2000. **8**(3): p. 141-50.

16. Quatman, C.E., C.C. Quatman-Yates, and T.E. Hewett, *A 'plane' explanation of anterior cruciate ligament injury mechanisms: a systematic review.* Sports Med, 2010. **40**(9): p. 729-46.

17. Hashemi, J., Breighner, R., Chandrashekar, N., Hardy, D.M., Chaudhari, A.M., Shultz, S.J., Slauterbeck, J.R., Beynnon, B.D., *Hip extension, knee flexion paradox: a new mechanism for non-contact ACL injury.* J Biomech, 2011. **44**(4): p. 577-85.

18. Huetink, K., Nelissen, R.G., Watt, I., van Erkel, A.R., Bloem, J.L., *Localized development of knee osteoarthritis can be predicted from MR imaging findings a decade earlier.* Radiology, 2010. **256**(2): p. 536-46.

19. Borthakur, A., Mellon, E., Niyogi, S., Witschey, W., Kneeland, J.B., Reddy, R., *Sodium and T1rho MRI for molecular and diagnostic imaging of articular cartilage.* NMR Biomed, 2006. **19**(7): p. 781-821.

20. Burstein, D., Gray, M., Mosher, T., Dardzinski, B., *Measures of molecular composition and structure in osteoarthritis.* Radiol Clin North Am, 2009. **47**(4): p. 675-86.

21. Gray, M.L., Burstein, D., Kim, Y.J., Maroudas, A., *2007 Elizabeth Winston Lanier Award Winner. Magnetic resonance imaging of cartilage glycosaminoglycan: basic principles, imaging technique, and clinical applications.* J Orthop Res, 2008. **26**(3): p. 281-91.

22. Link, T.M., *MR imaging in osteoarthritis: hardware, coils, and sequences.* Radiol Clin North Am, 2009. **47**(4): p. 617-32.

23. Gold, G.E., Chen, C.A., Koo, S., Hargreaves, B.A., Bangerter, N.K., *Recent advances in MRI of articular cartilage.* AJR Am J Roentgenol, 2009. **193**(3): p. 628-38.

24. Regatte, R.R., Akella, S.V., Borthakur, A., Reddy, R., *Proton spin-lock ratio imaging for quantitation of glycosaminoglycans in articular cartilage.* J Magn Reson Imaging, 2003. **17**(1): p. 114-21.

25. Wheaton, A.J., Dodge, G.R., Elliot, D.M., Nicoll, S.B., Reddy, R., *Quantification of cartilage biomechanical and biochemical properties via T1rho magnetic resonance imaging.* Magn Reson Med, 2005. **54**(5): p. 1087-93.

26. Shepherd, D.E. and B.B. Seedhom, *Thickness of human articular cartilage in joints of the lower limb.* Ann Rheum Dis, 1999. **58**(1): p. 27-34.

27. Eckstein, F., Heudorfer, L., Faber, S.C., Burgkart R., Englmeier, K.H., Reiser, M., *Long-term and resegmentation precision of quantitative cartilage MR imaging (qMRI).* Osteoarthritis Cartilage, 2002. **10**(12): p. 922-8.

28. Keenan, K.E., Besier, T.F., Pauly, J.M., Han, E., Rosenberg, J., Smith, R.L., Delp, S.L., Beaupre, G.S., Gold, G.E., *Prediction of glycosaminoglycan content in human cartilage by age, T1rho and T2 MRI.* Osteoarthritis Cartilage, 2011. **19**(2): p. 171-9.

29. Cibere, J., Sayre, E.C., Guermazi, A., Nicolaou, S., Kopec, J.A., Esdaile, J.M., Thorne, A., Singer, J., Wong, H., *Natural history of cartilage damage and osteoarthritis progression on magnetic resonance imaging in a population-based cohort with knee pain.* Osteoarthritis Cartilage, 2011. **19**(6): p. 683-8.

30. Hayashi, D., A. Guermazi, and D.J. Hunter, *Osteoarthritis year 2010 in review: imaging.* Osteoarthritis Cartilage, 2011. **19**(4): p. 354-60.

31. Frobell, R.B., Le Graverand, M.P., Buck, R., Roos, E.M., Roos, H.P., Tamez-Pena, J., Totterman, S., Lohmander, L.S., *The acutely ACL injured knee assessed by MRI: changes in joint fluid, bone marrow lesions, and cartilage during the first year.* Osteoarthritis Cartilage, 2009. **17**(2): p. 161-7.

32. Blumenkrantz, G. and S. Majumdar, *Quantitative magnetic resonance imaging of articular cartilage in osteoarthritis.* Eur Cell Mater, 2007. **13**: p. 76-86.

33. Sowers, M., Karvonen-Gutierrez, C.A., Jacobson, J.A., Jiang, Y., Yosef, M., *Associations of anatomical measures from MRI with radiographically defined knee osteoarthritis score, pain, and physical functioning.* J Bone Joint Surg Am, 2011. **93**(3): p. 241-51.

34. Kellgren, J.H. and J.S. Lawrence, *Radiological assessment of osteo-arthrosis.* Ann Rheum Dis, 1957. **16**(4): p. 494-502.

35. Pakin, S.K., M.E. Schweitzer, and R.R. Regatte, *3D-T1rho quantitation of patellar cartilage at 3.0T.* J Magn Reson Imaging, 2006. **24**(6): p. 1357-63.

36. Ogino, S., Huang, T., Watanabe, A., Iranpour-Boroujeni, T., Yoshioka, H., *Magnetic resonance imaging of articular cartilage abnormalities of the far posterior femoral condyle of the knee.* Acta Radiol, 2010. **51**(1): p. 52-7.

37. Johnson, D.L., Urban, W.P. Jr., Caborn, D.N., Vanarthos, W.J., Carlson, C.S., *Articular cartilage changes seen with magnetic resonance imaging-detected bone bruises associated with acute anterior cruciate ligament rupture.* Am J Sports Med, 1998. **26**(3): p. 409-14.

38. Theologis, A.A., Kuo, D., Cheng, J., Bolbos, R.I., Carballido-Gamio, J., Ma, C.B., Li, X., *Evaluation of bone bruises and associated cartilage in anterior cruciate ligament-injured and -reconstructed knees using quantitative t(1rho) magnetic resonance imaging: 1-year cohort study.* Arthroscopy, **27**(1): p. 65-76.

39. Stahl, R., Luke, A., Li, X., Carballido-Gamio, J., Ma, C.B., Majumdar, S., Link, T.M., *T1rho, T2 and focal knee cartilage abnormalities in physically active and sedentary healthy subjects versus early OA patients--a 3.0-Tesla MRI study.* Eur Radiol, 2009. **19**(1): p. 132-43.

40. Derrett, S., Stokes, E.A., James, M., Bartlett, W., Bentley, G., *Cost and health status analysis after autologous chondrocyte implantation and mosaicplasty: a retrospective comparison.* Int J Technol Assess Health Care, 2005. **21**(3): p. 359-67.

41. Taylor, C., Carballido-Gamio, J., Majumdar, S., Li, X., *Comparison of quantitative imaging of cartilage for osteoarthritis: T2, T1rho, dGEMRIC and contrast-enhanced computed tomography.* Magn Reson Imaging, 2009. **27**(6): p. 779-84.

42. Regatte, R.R., Akella, S.V., Wheaton, A.J., Lech, G., Borthakur, A., Kneeland, J.B., Reddy, R., *3D-T1rho-relaxation mapping of articular cartilage: in vivo assessment of early degenerative changes in symptomatic osteoarthritic subjects.* Acad Radiol, 2004. **11**(7): p. 741-9.

43. Burstein, D., *MRI for development of disease-modifying osteoarthritis drugs.* NMR Biomed, 2006. **19**(6): p. 669-80.

44. Peterfy, C.G., E. Schneider, and M. Nevitt, *The osteoarthritis initiative: report on the design rationale for the magnetic resonance imaging protocol for the knee.* Osteoarthritis Cartilage, 2008. **16**(12): p. 1433-41.

45. Eckstein, F., Ateshian, G., Burgkart, R., Burstein, D., Cicuttini, F., Dardzinski, B., Gray, M., Link, T.M., Majumdar, S., Mosher, T., Peterfy, C., Totterman, S., Waterton, J., Winalski, C.S., Felson, D., *Proposal for a nomenclature for magnetic resonance imaging based measures of articular cartilage in osteoarthritis.* Osteoarthritis Cartilage, 2006. **14**(10): p. 974-83.

46. Link, T.M., Sell, C.A., Masi, J.N., Phan, C., Newitte, D., Lu, Y., Steinbach, L., Majumdar, S., *3.0 vs 1.5 T MRI in the detection of focal cartilage pathology--ROC analysis in an experimental model.* Osteoarthritis Cartilage, 2006. **14**(1): p. 63-70.

47. Bitar, R., Leung, G., Pernq, R., Tadros, S., Moody, A.R., Sarrazin, J., McGregor, C., Christakis, M., Symons, S., Nelson, A., Roberts, T.P., *MR pulse sequences: what every radiologist wants to know but is afraid to ask.* Radiographics, 2006. **26**(2): p. 513-37.

48. Farrelly, C., Davarpanah, A., Brennan, S., Sampson, M., Eustace, S.J., *Imaging of soft tissues adjacent to orthopedic hardware: comparison of 3-T and 1.5-T MRI.* AJR Am J Roentgenol, 2010. **194**(1): p. W60-4.

49. Bauer, J.R.C., Li X, Carballido-Gamio J, Banerjee S, Krug R., *Optimization and reproducibility evaluation of volumetric cartilage measurements of the knee at 1.5T and 3T.* Proceedings of the Thirteenth Meeting of the International Society for Magnetic Resonance in Medicine, 2005.

50. Lutterbey, G., Behrends, K., Falkenhausen, M.V., Wattjes, M.P., Morakkabati, N., Gieseke, J., Schild, H., *Is the body-coil at 3 Tesla feasible for the MRI evaluation of the painful knee? A comparative study.* Eur Radiol, 2007. **17**(2): p. 503-8.

51. Erickson, S.J., Cox, I.H., Hyde, J.S., Carrera, G.F., Strandt, J.A., Estkowski, L.D., *Effect of tendon orientation on MR imaging signal intensity: a manifestation of the "magic angle" phenomenon.* Radiology, 1991. **181**(2): p. 389-92.

52. Kornaat, P.R., Reeder, S.B., Koo, S., Brittain, J.H., Yu, H., Andriacchi, T.P., Gold, G.E., *MR imaging of articular cartilage at 1.5T and 3.0T: comparison of SPGR and SSFP sequences.* Osteoarthritis Cartilage, 2005. **13**(4): p. 338-44.

53. Carneiro, A.A.O., Vilela, G.R., de Araujo, D.B., Baffa, O., *MRI relaxometry: Methods and applications.* Brazilian Journal of Physics, 2006. **36**(1A): p. 9-15.

54. Regatte, R.R., Akella, S.V., Wheaton, A.J., Borthakur, A., Kneeland, J.B., Reddy, R., *T 1 rho-relaxation mapping of human femoral-tibial cartilage in vivo.* J Magn Reson Imaging, 2003. **18**(3): p. 336-41.

55. Kanal, E., Broome, D.R., Martin, D.R., Thomsen, H.S., *Response to the FDA's May 23, 2007, nephrogenic systemic fibrosis update.* Radiology, 2008. **246**(1): p. 11-4.

56. Li, X., Ma, C.B., Link, T.M., Castillo, D.D., Blumenkrantz, G., Lozano, J., Carballido-Gamio, J., Ries, M., Majumdar, S., *In vivo T(1rho) and T(2) mapping of articular cartilage in osteoarthritis of the knee using 3 T MRI.* Osteoarthritis Cartilage, 2007. **15**(7): p. 789-97.

57. Redfield, A.G., *Nuclear Magnetic Resonance Saturation and Rotary Saturation in Solids.* Physical Review, 1955. **98**(6): p. 1787-1809.

58. Knispel, R.R., R.T. Thompson, and M.M. Pintar, *Dispersion of Proton Spin-Lattice Relaxation in Tissues.* J Magn Reson, 1974. **14**(1): p. 44-51.

59. Borthakur, A., Gur, T., Wheaton, A.J., Corbo, M., Trojanowski, J.Q., Lee, V.M., Reddy, R., *In vivo measurement of plaque burden in a mouse model of Alzheimer's disease.* J Magn Reson Imaging, 2006. **24**(5): p. 1011-7.

60. Pedersen, D.R., Thedens, D.R., Klocke, N.F., Baer, T.E., Martin, J.A., *Effect of B0 Magnetic Field Changes on Quantitative T1 Rho Relaxation Measurements.* Osteoarthritis and Cartilage, 2010. **18**: p. S198-S198.

61. Duvvuri, U., Reddy, R., Patel, S.D., Kaufman, J.H., Kneeland, J.B., Leigh, J.S., *T1rho-relaxation in articular cartilage: effects of enzymatic degradation.* Magn Reson Med, 1997. **38**(6): p. 863-7.

62. Duvvuri, U., Charagundla, S.R., Kudchodkar, S.B., Kaufman, J.H., Kneeland, J.B., Rizi, R., Leigh, J.S., Reddy, R., *Human knee: in vivo T1(rho)-weighted MR imaging at 1.5 T--preliminary experience.* Radiology, 2001. **220**(3): p. 822-6.

63. Wheaton, A.J., Casey, F.L., Gougoutas, A.J., Dodge, G.R., Borthakur, A., Lonner, J.H., Schumacher, H.R., Reddy, R., *Correlation of T1rho with fixed charge density in cartilage.* J Magn Reson Imaging, 2004. **20**(3): p. 519-25.

64. Charagundla, S.R., Borthakur, A., Leigh, J.S., Reddy, R., *Artifacts in T(1rho)-weighted imaging: correction with a self-compensating spin-locking pulse.* J Magn Reson, 2003. **162**(1): p. 113-21.

65. U.S. Department of Health and Human Services, F. D.A., Center for Devices and Radiological Health. *Guidance for Industry: Guidance for the Submission of Premarket Notifications for Magnetic Resonance Diagnostic Devices*. 08/25/2010 [cited 2011 05/25/11]; http://www.fda.gov/

66. Li, X., Kuo, D., Theologis, A., Carballido-Gamio, J., Stehling, C., Link, T.M., Ma, C.B., Majumdar, S., *Cartilage in Anterior Cruciate Ligament-Reconstructed Knees: MR Imaging T1{rho} and T2--Initial Experience with 1-year Follow-up.* Radiology, 2011. **258**(2): p. 505-14.

67. Lozano, J., Li, X., Link, T.M., Safran, M., Majumdar, S., Ma, C.B., *Detection of posttraumatic cartilage injury using quantitative T1rho magnetic resonance imaging. A report of two cases with arthroscopic findings.* J Bone Joint Surg Am, 2006. **88**(6): p. 1349-52.

68. Thedens, D., *Fast MRI Techniques*, in *Magnetic Resonance Imaging Systems* 2010: Iowa City.

69. Zuo, J., Li, X., Banerjee, S., Han, E., Majumdar, S., *Parallel imaging of knee cartilage at 3 Tesla.* J Magn Reson Imaging, 2007. **26**(4): p. 1001-9.

70. Kijowski, R., Blankenbaker, D.G., Davis, K.W., Shinki, K., Kaplan, L.D., De Smet, A.A., *Comparison of 1.5- and 3.0-T MR imaging for evaluating the articular cartilage of the knee joint.* Radiology, 2009. **250**(3): p. 839-48.

71. Saupe, N., Pfirrmann, C.W., Schmid, M.R., Schertler, T., Manestar, M., Weishaupt, D., *MR imaging of cartilage in cadaveric wrists: comparison between imaging at 1.5 and 3.0 T and gross pathologic inspection.* Radiology, 2007. **243**(1): p. 180-7.

72. Bjarnason, T.A. and J.R. Mitchell, *AnalyzeNNLS: magnetic resonance multiexponential decay image analysis.* J Magn Reson, 2010. **206**(2): p. 200-4.

73. Does, M.D. and J.C. Gore, *Complications of nonlinear echo time spacing for measurement of T (2).* NMR Biomed, 2000. **13**(1): p. 1-7.

74. Dula, A.N., D.F. Gochberg, and M.D. Does, *Optimal echo spacing for multi-echo imaging measurements of Bi-exponential T2 relaxation.* J Magn Reson, 2009. **196**(2): p. 149-56.

75. Koff, M.F., Amrami, K.K., Felmlee, J.P., Kaufman, K.R., *Bias of cartilage T2 values related to method of calculation.* Magn Reson Imaging, 2008. **26**(9): p. 1236-43.

76. Papanikolaou, N., Maniatis, V., Pappas, J., Roussakis, A., Efthimiadou, R., Andreou, J., *Biexponential T2 relaxation time analysis of the brain: correlation with magnetization transfer ratio.* Invest Radiol, 2002. **37**(7): p. 363-7.

77. Shrager, R.I., G.H. Weiss, and R.G. Spencer, *Optimal time spacings for T2 measurements: monoexponential and biexponential systems.* NMR Biomed, 1998. **11**(6): p. 297-305.

78. Pagano, M. and K. Gauvreau, *Principles of biostatistics*. 2nd ed, 2000, Pacific Grove, CA: Duxbury.

79. 1984-2011 [cited 2009-2011]. http://www.mathworks.com/

80. Yoshimura, K., Kato, H., Kuroda, M., Yoshida, A., Hanamoto, K., Tanaka, A., Tsunoda, M., Kanazawa, S., Shibuya, K., Kawasaki, S., Hiraki, Y., *Development of a tissue-equivalent MRI phantom using carrageenan gel.* Magn Reson Med, 2003. **50**(5): p. 1011-7.

81. Sonka, M., V. Hlavac, and R. Boyle, *Image processing, analysis, and machine vision*. 3rd ed, 2008, Toronto: Thompson Learning. xxv, 829 p.

82. Penney, G.P., Weese, J., Little, J.A., Desmedt, P., Hill, D.L., Hawkes, D.J., *A comparison of similarity measures for use in 2-D-3-D medical image registration.* IEEE Trans Med Imaging, 1998. **17**(4): p. 586-95.

83. Carballido-Gamio, J., T.M. Link, and S. Majumdar, *New techniques for cartilage magnetic resonance imaging relaxation time analysis: texture analysis of flattened cartilage and localized intra- and inter-subject comparisons.* Magn Reson Med, 2008. **59**(6): p. 1472-7.

84. Reiter, D.A., Roque, R.A., Lin, P.C., Doty, S.B., Pleshko, N., Spencer, R.G., *Improved specificity of cartilage matrix evaluation using multiexponential transverse relaxation analysis applied to pathomimetically degraded cartilage.* NMR Biomed, 2011.

85. Oh, J., Han, E.T., Pelletier, D., Nelson, S.J., *Measurement of in vivo multi-component T2 relaxation times for brain tissue using multi-slice T2 prep at 1.5 and 3 T.* Magn Reson Imaging, 2006. **24**(1): p. 33-43.

86. Carballido-Gamio, J., Stahl, R., Blumenkrantz, G., Romero, A., Majumdar S., Link T.M., *Spatial analysis of magnetic resonance T1rho and T2 relaxation times improves classification between subjects with and without osteoarthritis.* Medical Phys, 2009. **36**(9): p. 4059-67.

87. Hohe, J., Faber, S., Muehlbauer, R., Reiser, M., Englmeier, K.H., Eckstein, F., *Three-dimensional analysis and visualization of regional MR signal intensity distribution of articular cartilage.* Medical Engineering & Physics, 2002. **24**(3): p. 219-27.

88. Raya, J.G., Hornq, A., Dietrich, O., Weber, J., Dinges, J., Mutzel, E., Reiser, M.F., Glaser, C., *Voxel-based reproducibility of T2 relaxation time in patellar cartilage at 1.5 T with a new validated 3D rigid registration algorithm.* MAGMA, 2009. **22**(4): p. 229-39.

89. Canny, J., *A Computational Approach to Edge-Detection.* IEEE Trans Pattern Anal Mach Intell, 1986. **8**(6): p. 679-698.

90. Lacoste, C., J.J. Granizo, and E. Gomez-Barrena, *Reliability of a simple fluoroscopic method to study sagittal plane femorotibial contact changes in total knee arthroplasties during flexion.* Knee, 2007. **14**(4): p. 289-94.

91. Stahl, R., Blumenkrantz, G., Carballido-Gamio, J., Zhao, S., Munoz, T., Hellio Le Graverand-Gastineau, M.P., Li, X., Majumdar, S., Link, T.M., *MRI-derived T2 relaxation times and cartilage morphometry of the tibio-femoral joint in subjects with and without osteoarthritis during a 1-year follow-up.* Osteoarthritis Cartilage, 2007. **15**(11): p. 1225-34.

92. Ikeda, E.R., Schenkman, M.L., Riley, P.O., Hodge, W.A., *Influence of age on dynamics of rising from a chair.* Phys Ther, 1991. **71**(6): p. 473-81.

93. Tadimalla, S., *Evaluation of Post Traumatic Changes in Cartilage Using T1rho, T2 Imaging and dGEMRIC: A Line Profile Based Approach*, in *Biomedical Engineering,* 2009, University of Iowa: Iowa City.

94. Vellet, A.D., Marks, P., Fowler, P., Munro, T., *Accuracy of nonorthogonal magnetic resonance imaging in acute disruption of the anterior cruciate ligament.* Arthoscopy, 1989. **5**(4): p. 287-93.

95. Geeslin, A.G. and R.F. LaPrade, *Location of bone bruises and other osseous injuries associated with acute grade III isolated and combined posterolateral knee injuries.* Am J Sports Med, 2010. **38**(12): p. 2502-8.

96. Yin, Y., Zhang, X., Williams, R., Wu, X., Anderson, D.D., Sonka, M., *LOGISMOS--layered optimal graph image segmentation of multiple objects and surfaces: cartilage segmentation in the knee joint.* IEEE Trans Med Imaging, 2010. **29**(12): p. 2023-37.